Resonant inelastic x-ray scattering spectra for electrons in solids

Akio Kotani and Shik Shin

Institute for Solid State Physics, University of Tokyo, Kashiwanoha, Kashiwa, Chiba 277-8581, Japan

(Published 27 February 2001)

Resonant inelastic x-ray scattering (RIXS) has recently been a subject of remarkable progress due to the advent of high-brilliance synchrotron radiation sources. The authors present a review of both experimental and theoretical investigations of electrons in solids using this second-order optical process, in which there is coherent absorption and emission of x rays at resonance with electronic excitations. The review starts with some of the fundamental aspects of RIXS, after which are presented typical experimental data and their theoretical interpretation for various materials. The first class of materials considered is semiconductors and insulators (Si, C, and BN), which are typical systems with weak electron correlation, and the data are interpreted based on electronic states described by an energy-band model. Effects of symmetry of electronic states and electron momentum conservation are discussed. At the opposite extreme are rare-earth systems (metals and oxides), in which the $4f$ electrons are almost localized with strong electron correlation. The observations are interpreted based on the effects of intra-atomic multiplet coupling and weak interatomic electron transfer, which are well described with an Anderson impurity model or a cluster model. In this context a narrowing of spectral width in the excitation spectrum, polarization dependence, and the magnetic circular dichroism in ferromagnetic materials are discussed. The authors then consider transition-metal compounds, materials with electron correlation strengths intermediate between semiconductors and rare-earth systems. In these interesting cases there is an interplay of intra-atomic and interatomic electronic interactions that leads to limitations of both the band model and the Anderson impurity model. Finally, other topics in resonant x-ray emission studies of solids are described briefly.

CONTENTS

I. INTRODUCTION

Spectroscopic measurements are powerful tools in modern physics, and the interaction between light and matter is one of the primary experimental areas for probing the properties of solids. Especially important for studying electronic properties is light in the range of soft x rays and the vacuum ultraviolet, which interacts with electrons in solids, with strength that varies with the photon energy. Such techniques as photoemission spectroscopy and x-ray absorption spectroscopy are now standard tools for studying the electronic structure of materials (see, for instance, Kanamori and Kotani, 1988; Fujimori and Tokura, 1995; Hüfner, 1995; Rehr and Albers, 2000). The application of these techniques and the interpretation of the results are especially important in the studies of exciting new materials, including strongly correlated electron systems, new superconductors, organic materials, and complex systems.

Recently, technological advances have made possible a third generation of synchrotron radiation sources, give extremely high-brilliance light in the vacuum ultraviolet, soft-x-ray, and hard-x-ray regions. The brilliance of this

synchrotron radiation light is almost comparable with that produced by lasers. It has been found quite useful in studying the electronic structure of solids via x-ray emission spectroscopy (XES) and especially resonant inelastic x-ray scattering (RIXS). XES has a long history in solid-state physics, but it has made remarkable progress only very recently [see, for instance, Materlik *et al.* (1994), Ederer amd McGuire (1996), Nordgren and Kurmaev (2000)]; the recent interest in RIXS is sometimes called a ''renaissance'' in x-ray physics. It is the purpose of this article to review the present status of this renaissance.

XES is a spectroscopy of second-order optical processes, in which a core electron is excited by an incident x-ray photon and then this excited state decays by emitting an x-ray photon to fill the core hole. If the core electron is resonantly excited to the absorption threshold by the incident photon (as in the process of x-ray absorption spectroscopy), the resulting emission spectrum depends strongly on the incident-photon energy Ω, and we denote this type of XES as resonant x-ray emission spectroscopy (RXES). On the other hand, if the core electron is excited to the high-energy continuum well above the absorption threshold (as in the process of x-ray photoemission spectroscopy), we denote this type of XES as normal x-ray emission spectroscopy (NXES), where the spectral shape does not depend on Ω. Both RXES and NXES are second-order optical processes. The intermediate state of RXES is the same as the final state of x-ray absorption, whereas that of NXES is the same as the final state of x-ray photoemission. Resonant x-ray emission spectra are classified into two categories: when the emitted-photon energy ω is the same as that of the incident-photon energy Ω, the spectrum is called ''Rayleigh scattering'' or ''resonant elastic x-ray scattering,'' while for $\omega \neq \Omega$ it is called ''resonant inelastic x-ray scattering (RIXS).''

Since RXES and NXES include absorption and photoemission as excitation processes and further include information on radiative decay, the information given by them is much greater than that given by the first-order optical processes of x-ray absorption or photoemission. RIXS especially is one of the most powerful tools available for the study of electronic states in solids. We should stress that RIXS provides us with bulk-sensitive and site-selective information. Furthermore, it is a photon-in and photon-out process, so that this technique is equally applicable to metals and insulators and can be performed in applied electric or magnetic fields, as well as in applied high pressure. However, the intensity of the signal in a second-order optical process is much weaker than that of a first-order optical process because the efficiency of x-ray emission is quite low. In order to obtain precise experimental data, we need state-of-the-art experimental instrumentation. The recent implementation of undulator radiation at high-brilliance synchrotron light sources, as well as highly efficient detectors, were major contributors to the development of RIXS experiments. Since synchrotron radiation is tunable, it is quite useful for the measurements of RIXS, by which we can obtain selected information connected directly with a specific intermediate state to which the incident-photon energy is tuned. Further progress in RIXS can be expected with the use of higher-brilliance synchrotron sources.

The characteristic features of RIXS depend on materials. In semiconductors and insulators (Si, C, and BN), which are typical systems with weak electron correlation, the experimental RIXS data are interpreted based on electronic states described by an energy-band model. The effect of electron momentum conservation in the RIXS process determines the spectral features, which reflect the energy band dispersion of conduction and valence electrons (Ma *et al.*, 1992; Ma, 1994; Carlisle, Shirley, *et al.*, 1995; Shin *et al.*, 1996). At the opposite extreme, RIXS in rare-earth systems (metals and oxides), where the $4f$ electrons are almost localized with strong electron correlation, is interpreted based on an Anderson impurity model (or an atomic model), in which the effects of intra-atomic multiplet coupling and weak (or vanishing) interatomic electron transfer are taken into account (Hämäläinen *et al.*, 1991; Krisch *et al.*, 1995; Butorin, Mancini, *et al.*, 1996). As materials with electron correlation strength intermediate between semiconductors and rare-earth systems, transition-metal compounds provide an interesting regime to study the interplay between the local and itinerant character of $3d$ electrons (Hill *et al.*, 1998; Jiménez-Mier *et al.*, 1999). In any case, RIXS for f and d electron systems gives us important information on the electronic states, such as the intra-atomic multiplet coupling, electron correlation, and interatomic hybridization [see, for instance, the short review papers by Kotani (1997,1998,1999)].

A word about terminology is in order here. RIXS is sometimes called ''resonant x-ray fluorescence spectroscopy'' or ''resonant x-ray Raman spectroscopy.'' NXES is also sometimes called ''x-ray fluorescence spectroscopy'' or ''x-ray luminescence spectroscopy.'' The terms ''fluorescence'' and ''luminescence'' originally meant the emission from fully relaxed excited states. However, normal x-ray emission is not necessarily from fully relaxed states but from excitations well above the threshold. Since the electronic relaxation time is, in general, longer than the core-hole lifetime in the x-ray region, the excited states are not fully relaxed in NXES.

In this article, we present a review of both experimental and theoretical investigations of RIXS in solids, mainly in semiconductors, rare-earth systems, and transition-metal compounds. Our main interest is RIXS in the soft-x-ray region, but some interesting results in the hard-x-ray region are also included, which are associated with the $2p$ core level of rare-earth elements and the $1s$ core level of transition-metal elements. In Sec. II, we describe fundamental aspects of RIXS, including a basic description of RIXS, experimental measurements, and theoretical models. We discuss the RIXS of semiconductors and ionic crystals in Sec. III, rare-earth systems in Sec. IV, and transition-metal compounds in Sec. V. Sections VI and VII are devoted to other topics and concluding remarks.

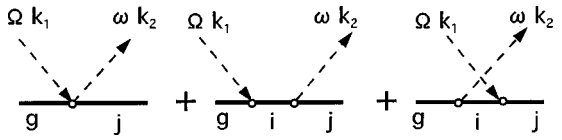

FIG. 1. Schematic representation of three scattering terms.

II. FUNDAMENTAL ASPECTS OF RESONANT INELASTIC X-RAY SCATTERING

A. Basic description of RIXS

Let us consider the x-ray scattering process in which an x-ray photon with energy Ω (wave vector $\mathbf{k}_1$) is incident on a material and then an x-ray photon with energy ω (wave vector $\mathbf{k}_2$) is emitted as a result of the electron-photon interaction in the material. We take into account the electron-photon interaction of the form $[e^2/(2mc^2)]\Sigma_n A(\mathbf{r}_n)^2$ by the lowest-order perturbation, and that of $[e/(mc)]\Sigma_n \mathbf{p}_n \cdot \mathbf{A}(\mathbf{r}_n)$ by the second-order perturbation, where $\mathbf{A}(\mathbf{r})$ is the vector potential of a photon. Then the differential scattering cross section (with respect to the solid angle $\Omega_{\mathbf{k}_2}$ and energy ω of the scattered photon) is expressed as (Kramers and Heisenberg, 1925; Heitler, 1944)

$$\frac{d^2\sigma}{d\Omega_{\mathbf{k}_2} d\omega} = \frac{\omega^2}{c^4}\left(\frac{1}{2\pi}\right)^3 W_{12}, \tag{1}$$

where the transition rate W_{12} is given by

$$\begin{aligned} W_{12} = \sum_j \frac{(2\pi)^3}{\Omega\omega}\left(\frac{e^2}{m}\right)^2 \delta(E_j - E_g + \omega - \Omega) \\ \times \left| \left[\langle j|\rho_{\mathbf{k}_1-\mathbf{k}_2}|g\rangle (\eta_1 \cdot \eta_2) \right.\right. \\ + \frac{1}{m}\sum_i \left(\frac{\langle j|\mathbf{p}(\mathbf{k}_2)\cdot\eta_2|i\rangle\langle i|\mathbf{p}(-\mathbf{k}_1)\cdot\eta_1|g\rangle}{E_i - E_g - \Omega} \right. \\ \left.\left. \left. + \frac{\langle j|\mathbf{p}(\mathbf{k}_1)\cdot\eta_1|i\rangle\langle i|\mathbf{p}(-\mathbf{k}_2)\cdot\eta_2|g\rangle}{E_i - E_g + \omega} \right) \right] \right|^2 . \end{aligned} \tag{2}$$

Here, $|g\rangle$, $|i\rangle$, and $|j\rangle$ are initial, intermediate, and final states of the material system, respectively, E_g, E_i, and E_j are their energies, and η_1 and η_2 are polarization directions (unit vectors) of incident and emitted photons. We have used units of $\hbar = 1$ for simplicity, and $\mathbf{p}(\mathbf{k})$ and $\rho_{\mathbf{k}}$ are defined by $\mathbf{p}(\mathbf{k}) = \Sigma_n \mathbf{p}_n \exp(-i\mathbf{k}\cdot\mathbf{r}_n)$, and $\rho_{\mathbf{k}} = \Sigma_n \exp(-i\mathbf{k}\cdot\mathbf{r}_n)$. The three terms in the square bracket of W_{12} are shown in Fig. 1 as a diagram representation. The first term comes from a first-order perturbation of an A^2-type interaction, and this x-ray scattering is called Thompson scattering. If we take into account only the Thompson scattering, the scattering cross section is rewritten as the standard expression

$$\frac{d^2\sigma}{d\Omega_{\mathbf{k}_2} d\omega} = \frac{\omega}{\Omega}\left(\frac{e^2}{mc^2}\right)^2 (\eta_1 \cdot \eta_2)^2 S(\mathbf{k}_1 - \mathbf{k}_2, \Omega - \omega), \tag{3}$$

where $S(\mathbf{k}, \nu)$ is the dynamical structure factor defined by

$$S(\mathbf{k}, \nu) = \frac{1}{2\pi}\int_{-\infty}^{\infty} dt \exp(i\nu t)\langle g|\rho_{\mathbf{k}}(t)\rho_{-\mathbf{k}}|g\rangle. \tag{4}$$

Therefore Thompson scattering gives us direct information on the elementary excitation caused by charge fluctuation in materials.

When the incident-photon energy is close to or above the core electron excitation threshold, as in the case of RIXS, the contribution of the second term becomes dominant. Above the threshold the denominator $E_i - E_g - \Omega$ vanishes, so that the second-order perturbation calculation breaks down. However, if we take into account that the intermediate state has a finite lifetime $\tau_i (= \hbar/\Gamma_i)$ because of the lifetime of a core hole, then the energy E_i is replaced by a complex number $E_i + i\Gamma_i$ and the divergence is removed (see, for instance, Sakurai, 1967; Tulkki and Åberg, 1980). Removing unimportant factors in Eq. (2), we can then describe the essential part of the RIXS spectrum in the form

$$\begin{aligned} F(\Omega, \omega) = \sum_j \left| \sum_i \frac{\langle j|T|i\rangle\langle i|T|g\rangle}{E_g + \Omega - E_i - i\Gamma_i} \right|^2 \\ \times \delta(E_g + \Omega - E_j - \omega), \end{aligned} \tag{5}$$

where the operator T represents the radiative transition, and Γ_i represents spectral broadening due to the core-hole lifetime in the intermediate state. If we consider the optical dipole transition (long-wavelength limit of the photon), T is given by $T = \mathbf{p}(0)\cdot\eta$. The quantity Γ_i is a result of the Auger and radiative decays of the core hole and, in most cases, it can be taken approximately to be constant, independent of the index i.

As can be seen from the expression of $F(\Omega, \omega)$, RIXS is the coherent second-order process consisting of the x-ray absorption from $|g\rangle$ to $|i\rangle$ and the x-ray emission from $|i\rangle$ to $|j\rangle$. If the final state $|j\rangle$ is the same as the initial state $|i\rangle$, then the spectrum of Eq. (5) describes resonant elastic x-ray scattering, while if $|j\rangle$ is not the same as $|i\rangle$, it gives the RIXS spectrum. When both cases are combined, $F(\Omega, \omega)$ of Eq. (5) is called the resonant x-ray emission spectrum. As in the case of Thompson scattering, RIXS provides us with important information on the charge excitations in material systems. Further, RIXS is much more useful than Thompson scattering: Usually Thompson scattering is too weak to obtain precise information about electronic excitations, but the intensity of RIXS is stronger because of the resonance effect. Thompson scattering depends on Ω and ω only through $\Omega - \omega$, but RIXS depends on both of them independently. Therefore we can obtain more detailed information about the electronic excitations by tuning Ω to different intermediate states. Since the intermediate states are different for different atomic species, the information given by RIXS depends on the atomic species.

Before closing this subsection, let us mention briefly two pioneering works in RIXS. Sparks (1974) observed resonant scattering of Cu K_α x rays incident on various target metals, Ni, Cu, Zn, and so on. In the intermediate state of this experiment a $1s$ electron was excited virtu-

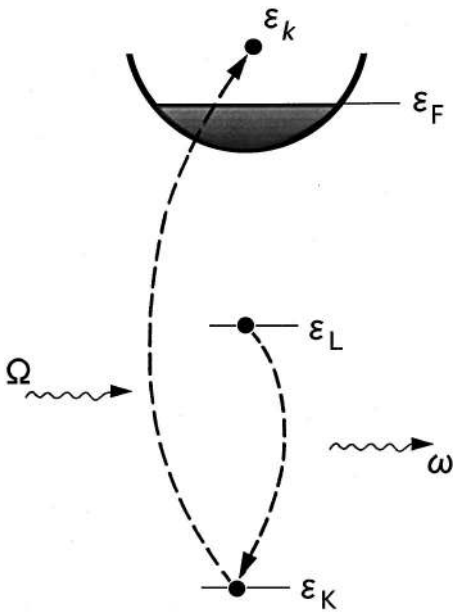

FIG. 2. Schematic representation of RIXS in Cu metal.

ally above the Fermi level ε_F, and in the final state a $2p$ electron made a radiative transition to the $1s$ state. Therefore the emitted photon was observed at $\omega \sim \Omega - (\varepsilon_F - \varepsilon_L)$, where $\varepsilon_F - \varepsilon_L$ corresponds to the binding energy of the $2p$ electron. It was found that the intensity of this emission was consistent with the resonant enhancement factor produced for each material.

Eisenberger *et al.* (1976a, 1976b) carried out the first RIXS experiment utilizing synchrotron radiation. Their experiment was performed for Cu metal. A schematic representation of the energy-level scheme of this experiment is given in Fig. 2. They changed the incident-photon energy Ω continuously around $(\varepsilon_F - \varepsilon_K)$ and observed the emitted photon in the neighborhood of $\omega \sim (\varepsilon_L - \varepsilon_K)$, where ε_K and ε_L are the Cu $1s$ and $2p$ core levels (more exactly, $2p_{3/2}$ in their experiments). The experimental result was consistent with what is expected from the second-order optical formula $F(\Omega,\omega)$ given by Eq. (5). If we disregard electron-electron interactions, $F(\Omega,\omega)$ is written, apart from unimportant factors, as

$$F(\Omega,\omega) \sim \sum_{\mathbf{k}(k>k_F)} \left| \frac{1}{\Omega - \varepsilon_{\mathbf{k}} + \varepsilon_K - i\Gamma_K} \right|^2 \delta(\omega + \varepsilon_{\mathbf{k}} - \varepsilon_L - \Omega)$$
$$= \begin{cases} \rho/[(\Delta E_0)^2 + \Gamma_K^2] & (\Delta E_0 \leqslant \Delta E_R) \\ 0 & (\Delta E_0 > \Delta E_R), \end{cases} \quad (6)$$

where

$$\Delta E_R = \Omega - (\varepsilon_F - \varepsilon_K), \quad (7)$$

$$\Delta E_0 = \omega - (\varepsilon_L - \varepsilon_K). \quad (8)$$

Here Γ_K and ρ are, respectively, the lifetime broadening of the $1s$ core level and the density of states of the conduction band. In the above expression for $F(\Omega,\omega)$ the effect of the lifetime broadening of the $2p$ core level (Γ_L) is disregarded for simplicity, but if it is taken into account, the discontinuity at $\Delta E_0 = \Delta E_R$ will be blurred out by the width Γ_L. In any case, the above calculation shows that for $\Delta E_R < 0$ the peak of $F(\Omega,\omega)$ occurs at $\Delta E_0 = \Delta E_R$ but for $\Delta E_R > 0$ it occurs at $\Delta E_0 = 0$. Furthermore, the half width at the half maximum of the peak should be minimized for $\Delta E_R = 0$. The experimental data of Eisenberger *et al.* were well explained by these facts.

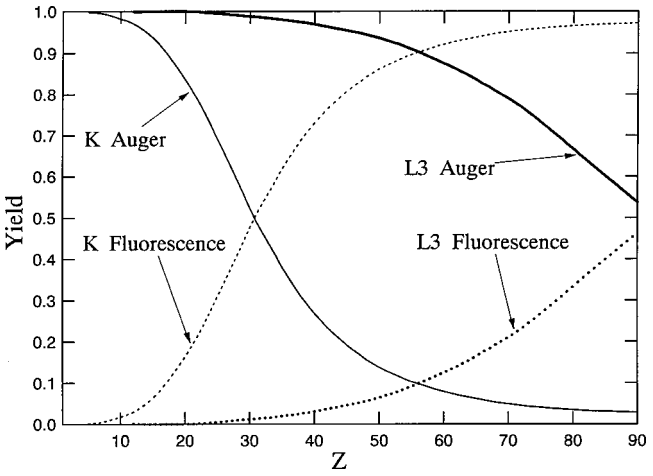

FIG. 3. Efficiencies of x-ray emission (fluorescence) compared to the Auger yield in a series of ions having S, L, and M angular momenta, based on the table by Krause (1979).

B. Experimental measurements

In spite of the long history of x-ray emission spectroscopy in solid-state physics, it is only recently that the study of XES in the soft-x-ray region has made much progress. This is because emission efficiency is quite low in the soft-x-ray region. Figure 3 shows the fluorescence and Auger yields for $1s$ (K) and $2p_{3/2}$ (L_3) subshells of different atoms. For light atoms, the Auger yield is larger than the fluorescence yield. The Auger yield decreases while the fluorescence yield increases, as the atomic number Z increases. There is a crossing around Zn for the K shell. The fluorescence efficiency is less than a few percent for light atoms. Furthermore, the extremely low optical reflectivity in the soft-x-ray region requires the grazing incidence configuration of the spectrometer, so that the solid angle that catches the emitted x rays becomes extremely small. Thus the development of XES is closely connected to that of state-of-the-art experimental instruments. In particular, it is tied to use of the recently developed brilliant undulator light sources as well as to use of a highly efficient detector.

A high-efficiency modern XES system has been developed by the Nordgren group (Nordgren, 1994) in Sweden and the Callcott and Ederer group (Callcott *et al.*, 1986; Ederer *et al.*, 1994) in the United States. Several groups in Japan (Shin *et al.*, 1995), Germany, and France have made similar types of experimental systems. A typical experimental system is shown in Fig. 4. Rowland mount-type grazing-incidence spectrometers are used. The typical spherical grating radii are from 3 to 10 m with a groove density from 300 to 2400 lines per mm.

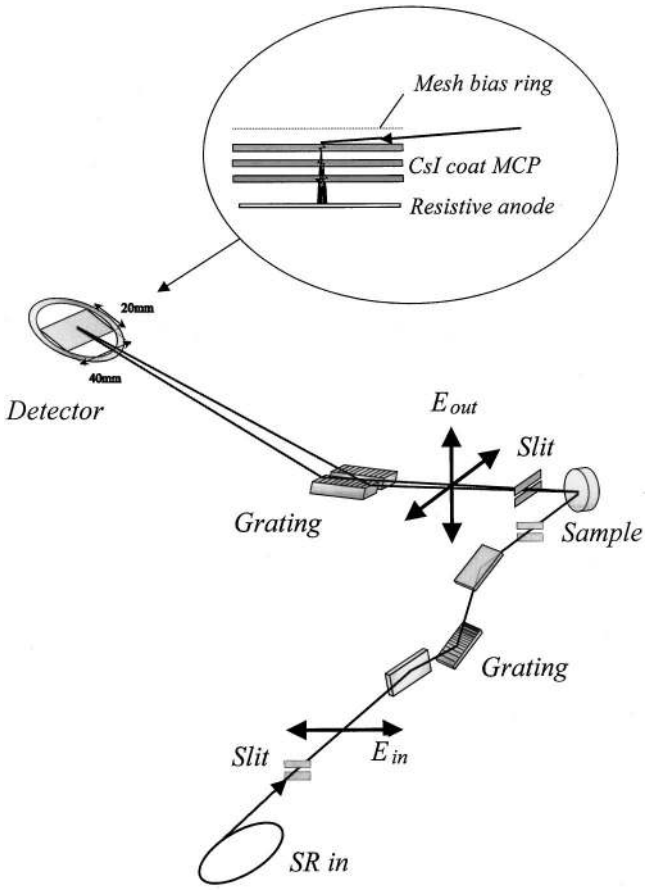

FIG. 4. Schematic illustration of the experimental setup for RIXS measurements.

Variable-pitched grating spectrometers have also been proposed instead of normal grating spectrometers (Callcott *et al.*, 1992; Muramatsu *et al.*, 1993). In each system, a slit is set just after the sample irradiated by the excitation x ray. The combination of slit width and dispersion of the grating, as well as optical distortion, mainly determine the resolution of the system. The highest-resolution $E/\Delta E$ so far has been about 1500. A small spot size is necessary for high resolution, and a high-brilliance light source is necessary in order to get a small spot size.

A highly sensitive detector is also important. For example, a two-dimensional position-sensitive detector with microchannel plates, usually 20–40 mm long. Large one-dimensional position-sensitive detectors have also been used. The thermal background has been diminished by the photon counting method. Usually the detector is used at grazing incidence, and the efficiency and position sensitivity of the microchannel plates is further enhanced by coating the photocathode with CsI and installing electron-retarding wires.

The photon energy calibrations of the beamline monochromator and the XES spectrometer are very important. In most cases, the spectrometer is calibrated by measuring the elastic x-ray scattering. Sometimes elastic scattering cannot be observed in the soft-x-ray region. In this case, NXES spectra of some metals, whose peak energy is listed in Bearden's table (Bearden, 1967), are used as the standard materials.

RIXS is a two-photon coherent optical process, so that it is thought that the polarization dependence of the incident and emitted x rays gives valuable information about the electronic structure (Guo, Wassdahl, *et al.*, 1995; Harada *et al.*, 1998). Figure 5 shows a front view of a spectrometer configured to measure the polarization dependence of RIXS. The analyzer chamber can be rotated by 90° together with the spectrometer around the axis of the incident-photon beam, where the center of rotation is located at the sample position. In the beamline, the electric field of the incident photon is polarized in the horizontal plane. When the RIXS is measured by the configuration shown in Fig. 5(a) (labeled ''depolarized configuration'') the polarization of the emitted x

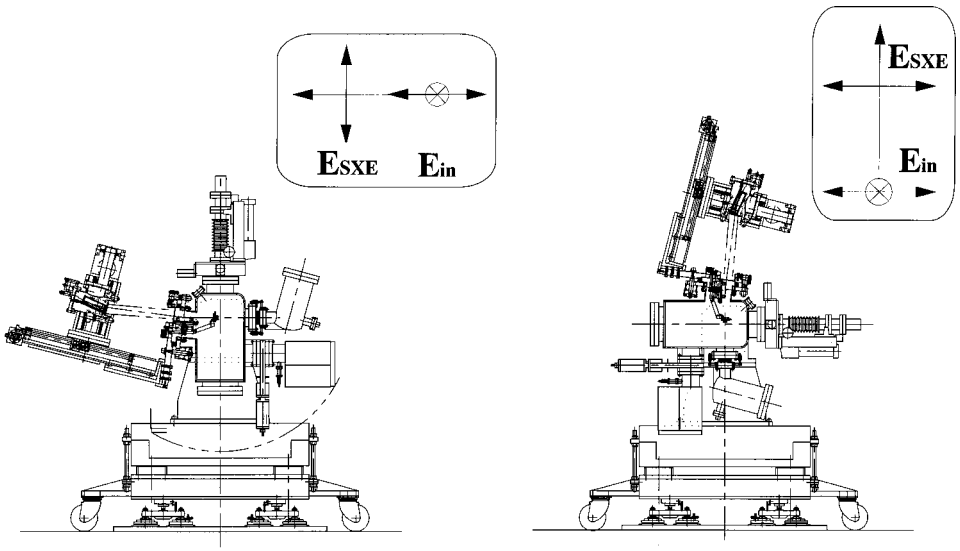

(a) depolarized configuration (b) polarized configuration

FIG. 5. Front view of spectrometer for polarized RIXS measurements. From Harada *et al.*, 1998.

ray is perpendicular to the polarization of the incident x ray. On the other hand, when the RIXS is measured by the configuration shown in Fig. 5(b) (labeled "polarized configuration"), the polarization of the emitted x ray is the same as that of the incident x ray. Some aspects of the polarization dependence in RIXS will be discussed in Secs. IV.E and V.C.

C. Theoretical models

In general there are two opposing approaches to describing electronic states in solids, the spatially extended model and the local model. The former treats an infinite number of atoms forming a periodic lattice with use of the energy-band theory (the band model). It is appropriate for application to s, p, and sometimes d electron systems with weak correlation. On the other hand, the latter treats a single atom or a cluster consisting of a small number of atoms (the free-atom or cluster model), and it is appropriate for application to f and d electron systems, which are relatively localized with strong correlation.

1. Energy-band model

Energy-band calculations commonly use the Kohn-Sham equation (Kohn and Sham, 1965) of density-functional theory (Hohenberg and Kohn, 1964):

$$\left\{-\frac{\hbar^2}{2m}\nabla^2+V_p(\mathbf{r})\right\}\phi_i(\mathbf{r})=\varepsilon_i\phi_i(\mathbf{r}), \tag{9}$$

with the periodic potential given by

$$V_p(\mathbf{r})=v_{ion}(\mathbf{r})+e^2\int d\mathbf{r}'\frac{n(\mathbf{r}')}{|\mathbf{r}-\mathbf{r}'|^2}+\frac{\delta E_{xc}[n(\mathbf{r})]}{\delta n(\mathbf{r})}, \tag{10}$$

where the electron density is represented by the eigenfunctions of the Kohn-Sham equation in the form

$$n(\mathbf{r})=\sum_i |\phi_i(\mathbf{r})|^2. \tag{11}$$

Here, $E_{xc}[n(\mathbf{r})]$ is the exchange-correlation energy, and $v_{ion}(\mathbf{r})$ is the potential of the ion lattice, which does not include the potential of the electrons under consideration. In order to obtain the expression for $E_{xc}[n(\mathbf{r})]$, one often uses a local-density-functional approximation (LDA), in which $E_{xc}[n(\mathbf{r})]$ is approximated by an electron gas whose density is the same as the local density of the system. However, the eigenenergies of the Kohn-Sham equation ε_i are not reliable as single-electron energies, so that, strictly speaking, we cannot use ε_i in the analysis of x-ray absorption or emission spectra. The density-functional theory is a powerful method for obtaining ground-state properties, but it is generally less accurate for excitations and for systems with strongly correlated electrons.

For systems with weak electron correlation, the Kohn-Sham equation reduces to the usual one-electron Schrödinger equation, so that its eigenenergy is useful as the single-electron energy, while its eigenfunction is useful as the single-electron wave function. Then Eq. (5) is reduced to

$$F(\Omega,\omega)=\sum_{i,j}\left|\sum_c\frac{\langle\phi_c|t|\phi_i\rangle\langle\phi_j|t|\phi_c\rangle}{\varepsilon_c+\Omega-\varepsilon_j-i\Gamma}\right|^2\delta(\varepsilon_i+\Omega-\varepsilon_j-\omega), \tag{12}$$

where the summations are taken over the core states c, occupied valence states i, and unoccupied valence states j (all in the one-electron description), and t is a one-electron operator of the optical transition. If we assume further that (i) the optical transition matrix element is constant and (ii) the selection rule due to momentum conservation can be disregarded, then Eq. (12) is simplified to

$$F(\Omega,\omega)\propto\int d\epsilon\frac{\rho(\varepsilon)\rho'(\varepsilon+\Omega-\omega)}{(\varepsilon-\varepsilon_L-\omega)^2+\Gamma^2}, \tag{13}$$

where ρ and ρ' are the partial densities of states for occupied and unoccupied states, respectively, and each has the symmetry allowed in the optical transition (Jiménez-Mier *et al.*, 1999). We can say that band theory is applicable to the analysis of x-ray absorption and emission for semiconductors and ionic insulators, but for f and d electron systems it has not often been used successfully in RIXS analysis.

2. Anderson impurity model

The cluster model or the so-called "Anderson impurity model" (which is also called the "impurity Anderson model") has been widely used for core-level spectroscopy, x-ray absorption and photoemission spectroscopy, and RIXS, of f and d electron systems. Especially for the analysis of the first-order optical processes, x-ray absorption and photoemission, the Anderson impurity model has been very successful (see, for instance, Kanamori and Kotani, 1988; Kotani, 1996). In this model, we consider only a single atom with f or d states, but at the same time the other more extended electrons such as conduction or valence electrons are described with the band model, and the hybridization between the localized f (or d) states and extended conduction (or valence) electron states is taken into account. The Anderson impurity model was originally proposed by Anderson (1961) in order to discuss the magnetic moment of an impurity atom of a $3d$ transition element in nonmagnetic host metals. Kotani and Toyozawa (1973a, 1973b, 1974) first analyzed x-ray photoemission and absorption of La metal by combining this model with the core-hole potential exerted on the $4f$ electrons in the final states of absorption and photoemission. After that, this model was extended to the analysis of x-ray absorption and photoemission spectra of mixed-valence Ce compounds by Gunnarsson and Schönhammer (1983). The Anderson impurity model can also be applied to insulating compounds with f or d electrons by replacing a conduction band with a completely filled valence band. For instance, Sawatzky and co-workers (Zaanen *et al.*, 1986) analyzed systematically the core-

level spectra of insulating $3d$ transition-metal compounds, and Kotani and co-workers (Kotani *et al.*, 1985; Kotani and Ogasawara, 1992) analyzed the core-level spectra of insulating rare-earth compounds.

The Hamiltonian of the model combined with the core-hole potential is described, for instance for rare-earth oxides, by

$$\begin{aligned} H=&\sum_{k,\nu}\epsilon_k a^\dagger_{k\nu}a_{k\nu}+\epsilon_f\sum_{\nu}a^\dagger_{f\nu}a_{f\nu}+\epsilon_c a^\dagger_c a_c \\ &+\frac{V}{\sqrt{N}}\sum_{k,\nu}(a^\dagger_{f\nu}a_{k\nu}+a^\dagger_{k\nu}a_{f\nu}) \\ &+U_{ff}\sum_{\nu>\nu'}a^\dagger_{f\nu}a_{f\nu}a^\dagger_{f\nu'}a_{f\nu'} \\ &-U_{fc}\sum_{\nu}a^\dagger_{f\nu}a_{f\nu}(1-a^\dagger_c a_c), \end{aligned} \tag{14}$$

where, ϵ_k, ϵ_f, and ϵ_c are the energies of the oxygen $2p$ valence band, the rare-earth $4f$ level, and the rare-earth core level, respectively. The index k denotes the energy level ($k=1\sim N$) in the valence band, and ν represents the combined indices for spin and orbital quantum numbers of the f symmetric state. It should be noted that the basis state of the valence band can approximately be taken as (k,ν) by an appropriate linear combination of Bloch states, as shown by Gunnarsson and Schönhammer (1983). The interactions V, U_{ff}, and $-U_{fc}$, respectively, are the hybridization between $4f$ and valence-band states, the Coulomb interaction between $4f$ electrons, and the core-hole potential acting on the $4f$ electron. This model has been further extended by including the intra-atomic multiplet coupling originating from multipole Coulomb interactions between $4f$ states, as well as between the $4f$ and core states, and the spin-orbit interaction of the $4f$ states and the core states.

In the case of transition-metal compounds, the $3d$ wave function of a transition metal is more extended than the $4f$ wave function of a rare earth, so that the $3d$ state is more sensitive to the local atomic arrangement around the transition-metal element. It is necessary to take into account the $3d$ energy level (including crystal-field splitting), which depends on the irreducible representation Γ of the local point-group symmetry, and also the hybridization strength $V(\Gamma)$ depending on Γ. Therefore the Hamiltonian of the Anderson impurity model for transition-metal compounds, for instance for transition-metal oxides, is

$$\begin{aligned} H=&\sum_{\Gamma,k,\sigma}\varepsilon_{\Gamma k}a^\dagger_{\Gamma k\sigma}a_{\Gamma k\sigma}+\sum_{\Gamma,\sigma}\varepsilon_{d\Gamma}a^\dagger_{d\Gamma\sigma}a_{d\Gamma\sigma} \\ &+\sum_{\mu}\varepsilon_p a^\dagger_{p\mu}a_{p\mu}+\sum_{\Gamma,k,\sigma}V(\Gamma k)(a^\dagger_{d\Gamma\sigma}a_{\Gamma k\sigma}+a^\dagger_{\Gamma k\sigma}a_{d\Gamma\sigma}) \\ &+U_{dd}\sum_{(\Gamma,\sigma)\neq(\Gamma',\sigma')}a^\dagger_{d\Gamma\sigma}a_{d\Gamma\sigma}a^\dagger_{d\Gamma'\sigma'}a_{d\Gamma'\sigma'} \\ &-U_{dc}\sum_{\Gamma,\sigma,\mu}a^\dagger_{d\Gamma\sigma}a_{d\Gamma\sigma}(1-a^\dagger_{p\mu}a_{p\mu}) \\ &+\frac{1}{2}\sum_{\nu_1,\nu_2,\nu_3,\nu_4}g_{dd}(\nu_1,\nu_2,\nu_3,\nu_4)a^\dagger_{d\nu_1}a_{d\nu_2}a^\dagger_{d\nu_3}a_{d\nu_4} \\ &+\sum_{\nu_1,\nu_2,\mu_1,\mu_2}g_{pd}(\nu_1,\nu_2,\mu_1,\mu_2)a^\dagger_{d\nu_1}a_{d\nu_2}a^\dagger_{p\mu_1}a_{p\mu_2} \\ &+\zeta_d\sum_{\nu_1,\nu_2}(\mathbf{l}\cdot\mathbf{s})_{\nu_1\nu_2}a^\dagger_{d\nu_1}a_{d\nu_2} \\ &+\zeta_p\sum_{\mu_1,\mu_2}(\mathbf{l}\cdot\mathbf{s})_{\mu_1\mu_2}a^\dagger_{p\mu_1}a_{p\mu_2}. \end{aligned} \tag{15}$$

Here $\varepsilon_{\Gamma k}$, $\varepsilon_{d\Gamma}$, and ε_p are energies of the oxygen $2p$ valence band, the transition-metal $3d$ state and a core level (with p symmetry), respectively. ν denotes the combined indices representing the spin (σ) and orbital (Γ) states, and μ is the spin and orbital states of the core level. g_{pd} represents the multipole components of the Coulomb interaction between $3d$ and core states, and g_{dd} that between $3d$ states, with both including the Slater integrals in their explicit forms. ζ_d and ζ_p are the spin-orbit coupling constants.

In the calculation of x-ray absorption, photoemission, and inelastic scattering spectra, for instance for rare-earth oxides in the nominally f^n ground state, the Hamiltonian is diagonalized taking into account the interatomic configuration interaction with a sufficient number of configurations, f^n, $f^{n+1}\underline{L}$, $f^{n+2}\underline{L}^2$, where $\underline{L}$ represents a hole in the oxygen $2p$ valence band. A similar calculation is also made for the final states of x-ray absorption and photoemission, as well as for the intermediate states of RIXS, which include a core hole. The main parameters of the Anderson impurity model are V, U_{ff}, U_{fc}, and the charge-transfer energy defined by

$$\Delta\equiv E(f^{n+1}\underline{L})-E(f^n),$$

where $E(f^n)$ is the energy averaged over multiplet terms of the f^n configuration. The Slater integrals and spin-orbit interaction constants, which describe the intra-atomic multiplet coupling, are obtained from a standard Hartree-Fock program (for instance, the program by Cowan, 1981).

For most rare-earth compounds and transition-metal compounds the Anderson impurity model has been successfully applied to the analysis of x-ray absorption and photoemission. However, its applicability to RIXS has not been well established. The first theoretical studies of XES and RIXS using this model were calculations of NXES for La compounds (Kayanuma and Kotani, 1988) and Ce compounds (Tanaka *et al.*, 1988, 1989), followed by studies of NXES and RIXS for Cu oxide systems (Tanaka, Okada, and Kotani, 1989, 1991), and RIXS for Ce oxides (Tanaka *et al.*, 1990). Only during the past several years has it become possible to obtain precise experimental RIXS data to compare with the theoretical predictions. The applicability of the Anderson impurity model to RIXS has been confirmed for many f electron systems. However, for d electron systems it has turned out that the model is not as applicable as it is for the description of x-ray absorption and photoemission. One

limitation is that, if the hybridization strength V is large, we have to take into account many configurations, d^n, $d^{n+1}\underline{L}$, $d^{n+2}\underline{L}^2$, ..., for the calculated results to converge. A more serious limitation in this case would be that the single metal-ion approximation breaks down, and we have to take into account the periodic arrangement of the metal ions, using an Anderson periodic model or a large cluster model including many metal ions.

3. Momentum selection rule

Resonant inelastic x-ray scattering is governed by several selection rules, one having to do with the electron wave vectors (the momentum selection rule) and another concerned with electron angular momentum (the dipole selection rule). To derive the momentum selection rule with the energy-band model, let us consider the situation in which the incident-photon energy is tuned to the excitation of a core electron to a conduction-electron state with energy $\epsilon_c(\mathbf{k}_c)$, that is,

$$\Omega = \epsilon_c(\mathbf{k}_c) - \epsilon_{core}(\mathbf{k}_{core}), \tag{16}$$

where $\mathbf{k}_{core}$ is the crystal momentum (wave vector) of the core electron. It is to be noted that the core electron state at each atomic site is degenerate, and we take their linear combination to construct the Bloch state $\phi_{core,\mathbf{k}_{core}}(\mathbf{r})$ with momentum $\mathbf{k}_{core}$. Then we obtain, from the dipole transition-matrix element [$T \simeq \mathbf{p}(0)\cdot\eta_1$ in Eq. (5)]

$$\langle i|T|g\rangle \simeq \int d\mathbf{r}\phi^*_{c,\mathbf{k}_c}(\mathbf{r})\mathbf{p}(0)\cdot\eta_1\phi_{core,\mathbf{k}_{core}}(\mathbf{r}), \tag{17}$$

where the momentum conservation is represented by

$$\mathbf{k}_c = \mathbf{k}_{core}. \tag{18}$$

Note that the wave vector of the incident photon is negligibly small in the soft-x-ray region. The emitted-photon energy is expressed as the energy difference between a valence electron and the core level:

$$\omega = \epsilon_v(\mathbf{k}_v) - \epsilon_{core}(\mathbf{k}'_{core}), \tag{19}$$

and momentum conservation gives

$$\mathbf{k}_v = \mathbf{k}_{core}. \tag{20}$$

Taking into account that RIXS is a coherent second-order process as described by Eq. (5), we find that $\mathbf{k}_{core} = \mathbf{k}'_{core}$, so that we obtain finally from Eqs. (18) and (20)

$$\mathbf{k}_c = \mathbf{k}_v. \tag{21}$$

Therefore inelastic x-ray scattering excites the electron-hole pair with vanishing total momentum. Equation (21) can be derived more directly from the total momentum conservation between the initial and final states, but the above argument is necessary to establish the value of $\mathbf{k}_c$ and also to discuss some relaxation effects in the intermediate state.

4. Normal XES

Equation (5) describes resonant x-ray scattering, but if we take Ω to be well above the x-ray absorption threshold, it can also describe normal x-ray emission. With sufficiently large Ω, a core electron is excited by the incident photon to a high-energy continuum (photoelectron state) $|\phi_\epsilon\rangle$ with energy ϵ, which can be treated as independent of other electrons. Then we put

$$|i\rangle = |\phi_\epsilon\rangle|i'\rangle, \quad E_i = E_{i'} + \epsilon, \tag{22}$$

$$|j\rangle = |\phi_\epsilon\rangle|j'\rangle, \quad E_j = E_{j'} + \epsilon, \tag{23}$$

into Eq. (5) and obtain

$$F(\Omega,\omega) = \sum_{j'} \int d\epsilon\rho(\epsilon)t^2 \left| \sum_{i'} \frac{\langle j'|T|i'\rangle\langle i'|a_c|g\rangle}{E_g + \Omega - E_{i'} - \epsilon - i\Gamma_{i'}} \right|^2 \times \delta(E_g + \Omega - E_{j'} - \epsilon - \omega), \tag{24}$$

where t ($\sim$ constant) is the dipole transition amplitude from a core state to the photoelectron state, a_c is the annihilation operator of the core electron, and $\rho(\epsilon)$ is the density of states (DOS) of the photoelectron. Performing the integration over ϵ and setting $\rho(\epsilon) \sim$ constant, we obtain

$$F(\Omega,\omega) = \rho t^2 \sum_{j'} \left| \sum_{i'} \frac{\langle j'|T|i'\rangle\langle i'|a_c|g\rangle}{E_{j'} - E_{i'} - \omega - i\Gamma_{i'}} \right|^2. \tag{25}$$

It is found that $F(\Omega,\omega)$ of NXES does not depend on Ω. Actually ρt^2 might depend on Ω, but the spectral shape of NXES is independent of Ω. Also, it is to be stressed that NXES is still a coherent second-order optical process, in which core-hole creation (i.e., the photoelectron excitation process) is correlated, in general, with the x-ray emission process (Tanaka *et al.*, 1989; Tanaka and Kotani, 1992). If we assume that the system is well described by a one-electron approximation (for instance, with the band model), then the effect of coherence is negligible. In this case, Eq. (25) reduces to

$$F(\Omega,\omega) = \rho t^2 \sum_{i}^{occ} \frac{|\langle\phi_c|t|\phi_i\rangle|^2}{(\omega - \epsilon_i + \epsilon_c)^2 + \Gamma_i^2}. \tag{26}$$

Therefore, if we assume that $|\langle\phi_c|t|\phi_i\rangle|^2 \sim$ constant and Γ_i is infinitesimally small, the NXES spectrum is proportional to the DOS of the occupied states i. Actually the NXES spectrum gives the partial DOS, which is symmetry-selected by the dipole transition $|\langle\phi_c|t|\phi_i\rangle|^2$ and broadened by the lifetime broadening Γ_i of the intermediate state.

If the incident-photon energy Ω is decreased down to the x-ray absorption threshold, t is no longer a constant and the excited electron couples with other electrons. Then $F(\Omega,\omega)$ depends strongly on Ω, and this is nothing but RXES (or RIXS). Thus RXES and NXES are two different aspects of the XES spectrum $F(\Omega,\omega)$, which are caused by the different characters of the intermediate states due to different choices of Ω. In between RXES and NXES, it is sometimes possible to observe an "NXES-like" spectrum, where the spectral shape of

$F(\Omega,\omega)$ is almost independent of Ω but depends on it slightly (see Secs. V.C and V.D).

The situation mentioned above is very similar to that found in Auger electron spectroscopy, the intermediate state of which is the same as that of XES, but the decay channel is the emission of an Auger electron rather than an x ray. Depending on whether Ω is near the threshold of XAS or well above the threshold, Auger electron spectroscopy is referred to as resonant (RAES) or normal (NAES), respectively, which are the counterparts of RXES and NXES. The kinetic energy of the Auger electron strongly depends on the incident-photon energy Ω for RAES, whereas it is independent of Ω for NAES. Some aspects of Auger electron spectroscopy are analogous to RXES (or RIXS) and NXES, which are discussed in the present paper.

III. RIXS IN SEMICONDUCTORS AND INSULATORS

A. Experimental data

RIXS in semiconductors has recently been measured extensively using synchrotron radiation, and it has given valuable information about the electronic structures. The site and symmetry selectivity, as well as the surface insensitivity, are especially distinctive properties of the spectroscopy. The RIXS transition is caused mainly within the same atomic species, because the core hole is strongly localized, so that information obtained via RIXS is mainly connected with a specific atomic species.

Inelastic scattering spectra for semiconductors and insulators have been obtained especially for the light elements, such as B, C, N, O, Si, S, Al, Mg, and P. So far, resonant (and normal) emission spectra have been analyzed for graphite (Carlisle, Shirley, *et al.*, 1995, 1999; Skytt *et al.*, 1994), Si (Rubensson *et al.*, 1990; Ma *et al.*, 1993; Miyano *et al.*, 1993; Eisebit *et al.*, 1996; Shin *et al.*, 1996), MgO, Al_2O_3, and SiO_2 (O'Brien, Jia, Callcott, Rubensson, *et al.*, 1991; O'Brien, Jia, Dong, Callcott, Mueller, *et al.*, 1991; O'Brien *et al.* 1992, 1993a, 1993b, 1993), B_2O_3 and silicides (Jia *et al.*, 1991, 1992), Li halides (Tsang *et al.*, 1987), cBN (Agui *et al.*, 1997; Hanamura *et al.*, 1997), hBN (Muramatsu *et al.*, 1993; Jia *et al.*, 1996), CdS and ZnS (Zhou *et al.*, 1997), diamond (Ma *et al.*, 1992), CaF_2 (Rubensson *et al.*, 1994a, 1994b; Jia *et al.*, 1998), $CaSi_x$ (Jia *et al.*, 1995), $Al_xGa_{1-x}As$ (Dong *et al.*, 1992), $Al_xGa_{1-x}N$ (Duda, Stagarescu, *et al.*, 1998), C_{60} (Luo *et al.*, 1995; Guo, Glans, *et al.*, 1995), Y_2O_3 (Mueller *et al.*, 1996), and GaN (Stagarescu *et al.*, 1996).

In this section, the RIXS of several semiconductors and insulators is discussed in order to clarify its mechanism. Since the electron correlation in semiconductors is weaker than in $3d$ and $4f$ compounds, RIXS is interpreted, on the basis of the energy-band model, in the independent-electron approximation. The energy eigenvalue of the Kohn-Sham Eq. (9) is regarded as the one-electron excitation energy, and the effects of exciton formation or electron-phonon interaction are incorporated in the band model, if necessary.

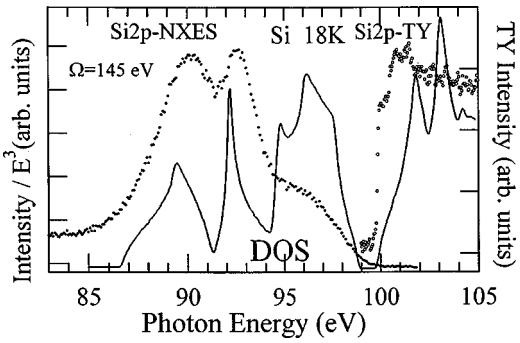

FIG. 6. Normal x-ray emission (NXES) spectrum of silicon measured at $\Omega=145.0$ eV and the total electron yield (TY) spectrum in comparison with the total DOS curve. From Shin *et al.*, 1996.

B. Silicon and graphite

Let us consider RIXS in Si as an example. Before discussing RIXS, we show in Fig. 6 experimental NXES data on Si $2p$, which are closely related to the inelastic scattering spectra to be considered later. Here solid circles show the normal x-ray emission measured with $\Omega=145.0$ eV (Shin *et al.*, 1996), while the total electron yield spectrum (which corresponds to Si $2p$ x-ray absorption) is plotted with open circles, in comparison with the total density of states (DOS) of valence and conduction bands (solid curves) obtained by energy-band calculations (Chelikowsky and Cohen, 1976). For the DOS of the valence band, it is known that the Si $3s$ component is dominant at lower energies, while the $3p$ component is dominant at higher energies. Since the $2p$ normal emission spectrum reflects the s and d partial DOS around a Si atom, it is reasonable that the observed NXES is relatively stronger than the calculated total DOS for $\omega=85-95$ eV, but relatively weaker for $\omega=95-100$ eV. The difference between the observed total yield and the calculated DOS of the conduction band originates mainly from the core exciton effect.

Experimental RIXS results at the Si $2p$ threshold are shown in Fig. 7 (Shin *et al.*, 1996), together with the energy-band dispersion curves calculated by Chelikowsky and Cohen (1976). The energy of the band dispersion curve is adjusted so that the valence-band maximum coincides with that of the RIXS spectrum. The incident-photon energies are taken at $\Omega=99.70$ and 101.46 eV, respectively, as shown with the arrows, which are located near the bottom of the conduction band (see the Si $2p$ total yield spectrum shown here again). For $\Omega=99.70$ eV, which corresponds to the bottom of the conduction band, the conduction electron at the X point (with X_1 symmetry) is selectively excited. Then, due to the momentum conservation rule, Eq. (21), the valence electron that makes a radiative transition to the core level should also be located at the X point. The two scattering peaks observed at $\omega=91.1$ and 96.0 eV correspond to the X_1 and X_4 states of the valence band. On the other hand, for $\Omega=101.46$ eV, the conduction electron at the L point (L_1 symmetry) is resonantly excited, and the observed three RIXS peaks at $\omega=90.2$, 92.5, and

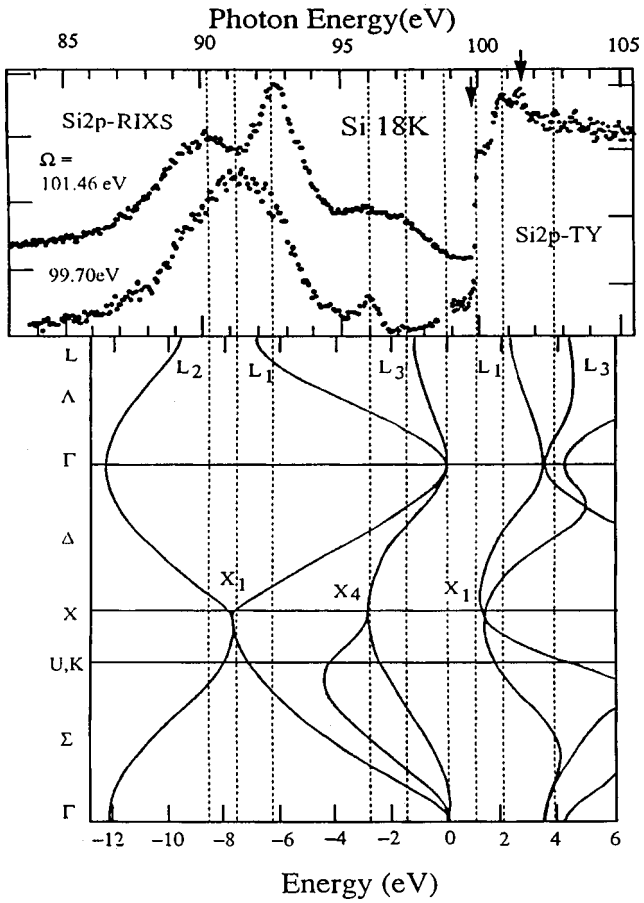

FIG. 7. RIXS spectra of Si measured at $\Omega = 101.46$ and 99.70 eV and the total electron yield (TY) spectrum in comparison with energy band dispersion curves. From Shin *et al.*, 1996.

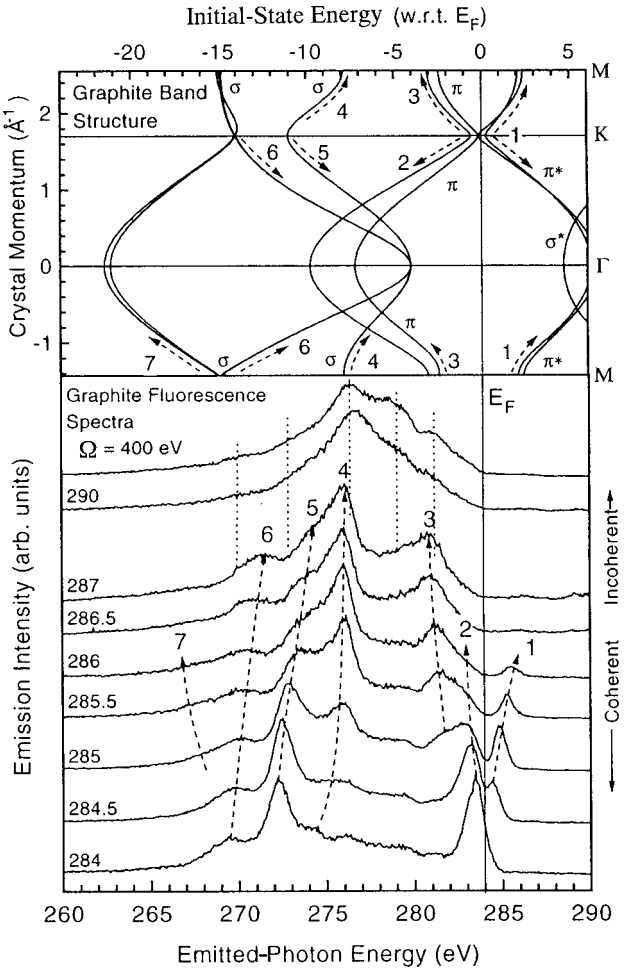

FIG. 8. RIXS spectra (fluorescence) of graphite and the energy-band dispersion curves. From Carlisle, Shirley *et al.*, 1995.

97.3 eV correspond to the $L_{2'}$, L_1, and $L_{3'}$ states of the valence band. In this way, the RIXS spectra strongly reflect the energy dispersion of the valence and conduction bands.

In the lower panel of Fig. 8 we show another example of RIXS measured for highly oriented pyrolytic graphite, a semimetal with a layered structure (Carlisle, Shirley, *et al.*, 1995). A carbon 1*s* electron is excited to the π^* band above the Fermi energy and an electron in the π and σ bands below the Fermi level makes a radiative transition to the 1*s* level. The upper panel is the graphite band structure with the energy axis matched to the emitted-photon energy of the RIXS data. The dispersive features labeled 1–7 in the spectrum are associated with the positions 1–7 of the band dispersion indicated by the dashed lines and arrows in the upper panel. Since the energy-band dispersion changes sharply near the Fermi level at the *K* point, the observed RIXS shape changes drastically with a small change in the incident-photon energy Ω around 284 eV. For $\Omega = 400$ eV, the observed spectrum corresponds to normal x-ray emission.

It is interesting to separate the contributions from π and σ bands by changing the direction of the emitted photon. In Fig. 8 the takeoff angle α of the emitted photon is near grazing ($\alpha = 25°$), where α is defined by the complementary angle between the emitted-photon direction and the sample surface normal. Since the π orbital (the p_z orbital) extends in the direction normal to the sample surface, x-ray emission from the π orbital is forbidden for a normal emission angle ($\alpha = 90°$), while emission from both π and σ orbitals is allowed for a grazing emission angle. In Fig. 9(a), the RIXS spectra observed for near-grazing ($\alpha = 25°$) and near-normal ($\alpha = 70°$) emission angles are shown. It can be clearly seen that the bands near the Fermi level are the π bands, and the σ bands are lower in energy. This is consistent with the fact that the hopping integral of the π orbitals is much smaller than that of the σ orbitals. Carlisle *et al.* also calculated the RIXS spectra based on *ab initio* energy-band calculations, and a comparison of Fig. 9(b) with Fig. 9(a) shows good agreement between the experimental and theoretical results. Two points are to be remarked here. (i) Since the π and π^* wave functions have opposite phase relations regarding their amplitudes on the two C atoms in the graphite unit cell, the strong π emission intensity observed near the threshold (π^* excitation) cannot be explained by a simple theory. In the calculation given in Fig. 9(b), the inequivalence of the two C atoms is assumed to reproduce the experimental intensity. (ii) The calculation is made using the coherent

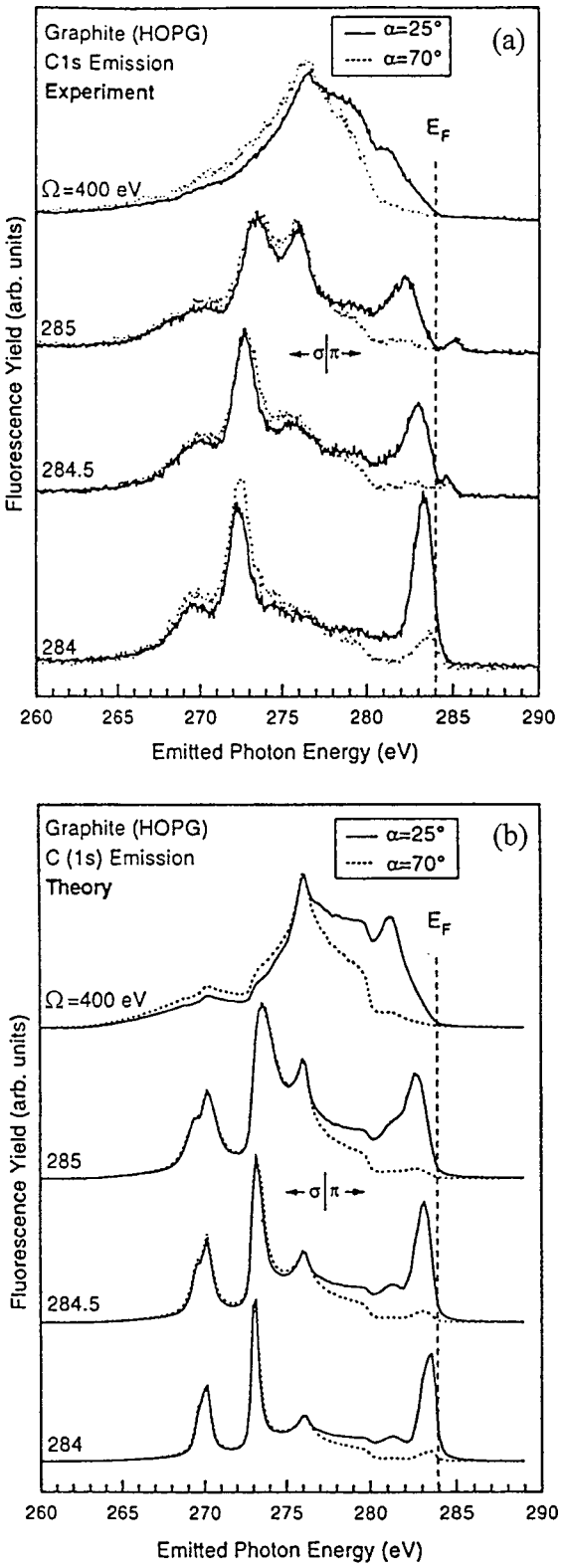

FIG. 9. Comparison between (a) experimental and (b) calculated results of RIXS for graphite. From Carlisle, Shirley *et al.*, 1995.

second-order optical formula, Eq. (5), but Fig. 9(b) is obtained by adding a small fraction (0.2–0.4) of the incoherent spectrum (with a spectral shape similar to that of NXES) to the calculated coherent spectra. Without the incoherent spectrum, the intensity at 276 eV is much smaller than the experimental one. This point will be discussed briefly in the next subsection.

In the rest of this subsection, we discuss the selection rules pertaining to RIXS and to interband optical absorption (Shin *et al.*, 1997). Figures 10(a) and (b) compare the RIXS spectrum of Si and the imaginary part of the dielectric function ε_2, calculated by Phillipp and Ehrenreich (1959), which is proportional to the interband optical absorption. The abscissa of the RIXS spectrum represents the energy loss $\Omega-\omega$ (Raman shift), which is compared with the absorbed photon energy in the ε_2 spectrum. The transition from the X_1 valence band to the lowest X_1 conduction band is observed around 8.5 eV in resonant inelastic scattering, but it is not found in the ε_2 spectrum, while the strong X_4 structure around 4 eV is found in the ε_2 spectrum, but it is very weak in RIXS. These facts suggest that the RIXS and ε_2 spectra in Si have different selection rules.

On the other hand, the RIXS and ε_2 spectra are very similar in *c*BN. Figures 10(c) and (d) compare the RIXS spectra excited at the conduction-band threshold and the ε_2 spectrum (Yokohama *et al.*, 1989). The strongest structure is located around 11.5 eV and is assigned to be X_5 (Agui *et al.*, 1997). The structures around 9 and 16 eV are also seen in both spectra. Thus we can see a marked contrast between Si and *c*BN when we compare RIXS and ε_2 spectra.

Here, one should remember that the selection rules for Raman scattering and the absorption spectrum have been studied for a long time by ordinary laser Raman scattering in the visible-light region. The situation in RIXS is essentially the same as in Raman scattering. The centrosymmetry of the crystal gives important and basic information on the selection rule. In the case of centrosymmetric crystals, the dipole mode is the ungerade mode and the Raman mode is the gerade mode. The dipole and Raman modes are complementary to each other. In fact, the transition from the X_1 valence band to the X_1 conduction band in Si is Raman active. On the other hand, the transition from the X_4 valence band to the X_1 conduction band is dipole allowed but is not Raman active. The X_4 band is observed weakly in RIXS, but it disappears when the incident-photon energy is well below the threshold, where the Raman selection rule is applicable more strictly. It is well known that the Raman selection rule is often broken in the resonant Raman process.

C. Effects of core exciton and phonon relaxation

In the theoretical calculation of Carlisle, Shirley, *et al.* (1995), which is displayed in Fig. 9(b), the effect of the core exciton in the intermediate state is disregarded. van Veenendaal and Carra (1997) theoretically studied the core exciton effect on the RIXS spectra of graphite, where they took into account a local core-hole potential U acting on the excited conduction electron and the value of U was taken as an adjustable parameter. For the energy band of graphite, they used the Slater-Koster

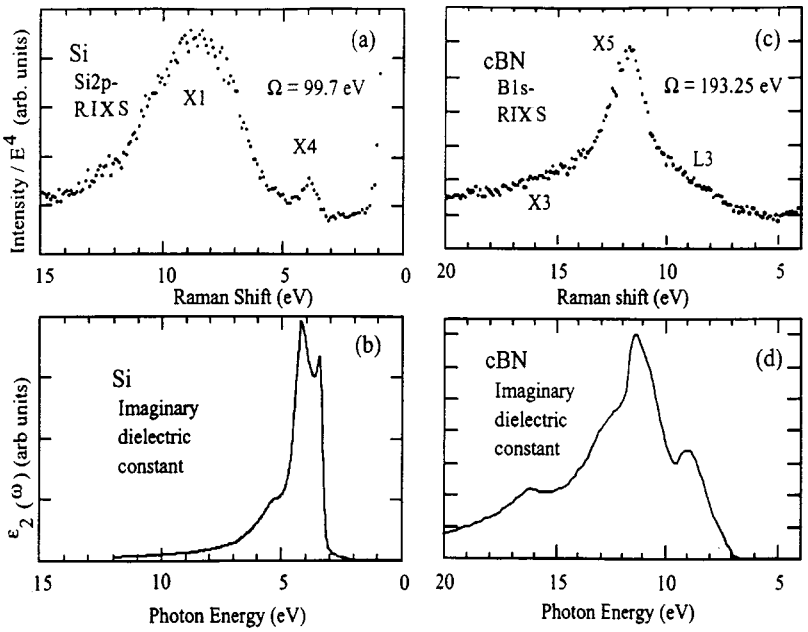

FIG. 10. Comparison between (a) RIXS and (b) ε_2 spectra of Si, and that between (c) RIXS and (d) ε_2 spectra of *c*BN. From Shin *et al.*, 1997.

tight-binding parametrization scheme. According to their results, the core exciton effect modifies the RIXS spectrum so as to enhance the intensity of the 276-eV peak in Fig. 9(a), so that the experimental results are reproducible without adding the incoherent contribution. It is to be noted that the core-hole potential exists only in the intermediate state, so that momentum conservation between the initial and final states [Eq. (21)] still holds, but the resonance condition [Eq. (16)] is now modified by the core exciton effect. Therefore, if the core hole potential is strong enough, the RIXS spectra can be affected significantly.

After van Veenendaal and Carra, Shirley (1998) treated the same problem by performing an *ab initio* energy-band calculation and by solving the Bethe-Salpeter equation (in the Tamm-Dancoff approximation) for the electron/core-hole scattering (the core exciton effect). The result of Shirley is in strong contrast with that of van Veenendaal and Carra: (i) In the absence of the core-hole effect, Shirley obtained a small RIXS peak at $\omega \sim 276$ eV (for $\Omega \sim 285$ eV) due to the σ band emission, and its intensity was enhanced by the π^* band resonance around the M point for $\Omega \sim 286$ eV (see the band structure shown in Fig. 8). On the other hand, the energy of the σ band around the M point of van Veenendaal and Carra is considerably higher than that of Shirley, so that there is no RIXS peak at $\omega \sim 276$ eV in the absence of the core hole. (ii) Shirley showed that the RIXS spectra with the core exciton effect are almost the same as those without the core exciton effect, though the x-ray absorption is strongly modified by the core hole in the manner shown by van Veenendaal and Carra. On the other hand, the core exciton effect caused, in the calculation by van Veenendaal and Carra, a strong enhancement of the RIXS intensity at 276 eV, as mentioned before.

Therefore the problem has not been resolved completely. The quantitative result of the core exciton effect on RIXS so far discussed depends on the model and the approximation used. A model RIXS calculation was also carried out by Minami (1998) taking into account both core exciton and valence exciton effects, but the results are qualitative and not useful in judging whether these effects are quantitatively important in the RIXS of graphite.

More recently, Carlisle *et al.* (1999) have made a more complete study of RIXS for graphite, as well as for *h*BN, both experimentally and theoretically. Their theoretical result is essentially the same as that of Shirley (1998), for Ω in the same energy range (π^* resonance region) as that in Fig. 8. However, in the higher energy region of Ω (σ^* resonance region) the core exciton effect contributes significantly to RIXS. So long as the RIXS spectrum is at $\omega \sim 276$ eV, we can say, from comparison of their experimental and theoretical results, that in order to reproduce the experimental RIXS spectra it is necessary to superpose some fraction of the NXES-like (incoherent) spectrum on the calculated coherent RIXS spectrum as shown in Fig. 9 (the situation is somewhat complicated because the intensity of the 276-eV peak comes from both the σ emission at the M point and the NXES). Therefore it is interesting to discuss what causes the incoherent contribution (NXES-like spectrum). A possible origin is the phonon relaxation effect. If the momenta $\mathbf{k}_c$ and $\mathbf{k}_{core}$ of the conduction electron and the core hole [in Eq. (18)] in the intermediate state are changed by interaction with phonons (by emitting or absorbing phonons), then conservation of the electron momentum [Eq. (21)] breaks down. If the electron (or hole) momentum distribution is relaxed sufficiently by electron-phonon scattering, then the RIXS spectrum tends to the partial DOS of the valence band, which has the same spectral shape as the normal x-ray emission spectrum. This is essentially the same as the "dephasing relaxation," a well-known second-order optical process in the visible region (Toy-

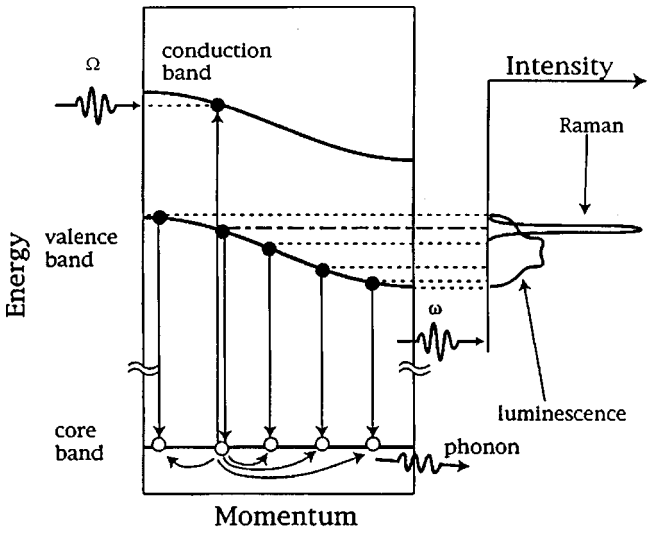

FIG. 11. Schematic model representing the effect of phonon relaxation in RIXS (left portion). The spectra of "Raman scattering" and "luminescence" are shown in the right portion. From Minami and Nasu, 1998.

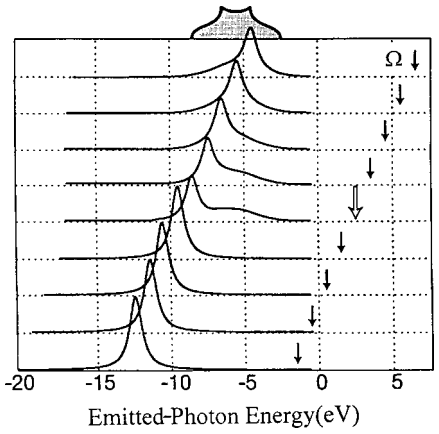

FIG. 12. Calculated RIXS for various positions (indicated by the arrows) of the incident photon. The shaded curve is the DOS. From Minami and Nasu, 1998.

ozawa, 1976; Takagawara *et al.*, 1977; Toyozawa *et al.*, 1977), in which a coherent Raman scattering spectrum is changed into an incoherent luminescence spectrum by the electron-phonon interaction.

There has been no quantitative calculation of phonon relaxation effects on the RIXS of graphite (or any realistic system), but a model calculation has been made by Minami and Nasu (1998). Their model is shown schematically in Fig. 11. They consider a conduction band and a valence band, both of which are represented by tight-binding s bands in the simple cubic lattice, and a dispersionless core band. In the intermediate state, they take into account the core-hole/phonon interaction given by the following site-diagonal linear coupling:

$$H_{c-pn}=-N^{-1/2}\sum_{\mathbf{q},\mathbf{l}}\Omega_{\mathbf{q}}S_{\mathbf{q}}^{1/2}e^{i\mathbf{q}\cdot\mathbf{l}}c_{\mathbf{l}}^{\dagger}c_{\mathbf{l}}(B_{\mathbf{q}}^{\dagger}+B_{-\mathbf{q}}), \quad (27)$$

where N is the number of lattice sites and $\Omega_{\mathbf{q}}$ is the phonon energy with wave vector $\mathbf{q}$. If the lifetime of the core hole is much shorter than the phonon relaxation time, the spectrum is given by the RIXS indicated by "Raman" in Fig. 11. On the other hand, if the lifetime is much longer than the relaxation time, the memory of the core-hole momentum is lost by phonon scattering, so that the spectrum tends to the DOS of the valence band as indicated by "luminescence." An example of the numerical calculation of RIXS spectra is given in Fig. 12, where the core-hole/phonon coupling constant $S(=N^{-1}\Sigma_{\mathbf{q}}S_{\mathbf{q}})$ is taken as 1.5 (weak-coupling regime), and the core-hole lifetime is taken to be almost comparable with the phonon relaxation time. The incident-photon energies are shown with solid arrows, and the specially outlined large arrow indicates the resonance energy with the lowest edge of the conduction band. When the incident-photon energy is below the conduction-band threshold, we have only the "Raman" spectra with virtual intermediate states. For incident-photon energy above the threshold, a Raman peak with no phonon relaxation and a broad luminescence coexist with comparable intensity. The luminescence spectrum reflects, more or less, the DOS of the valence band, which is depicted as the shaded curve at the top.

In the case of graphite, the lattice relaxation energy, which is represented in Minami and Nasu's model by

$$E_L=N^{-1}\sum_{\mathbf{q}} S_{\mathbf{q}}\Omega_{\mathbf{q}}, \quad (28)$$

is too small to be observed in the RIXS spectra. In the case of diamond, the lattice relaxation around a core hole is large, and this gives rise to a characteristic spectrum. Ma *et al.* (1993) observed resonant inelastic scattering in diamond just at the C 1s core exciton located at the absorption edge. In Fig. 13(a), their RIXS data are shown, where curves 1 and 2 are emission spectra with incident-photon energies at 289.6 eV (core exciton peak) and 294.5 eV (conduction band), respectively (see the C 1s x-ray absorption shown with the dotted curve). For spectrum 2, we see a band gap of about 6 eV, while for spectrum 1 we find an additional spectrum peaking at 289 eV and a long tail which fills the whole band-gap region. The absorption and emission spectra (for spectrum 1) in the band-gap region are shown by open and filled diamonds, respectively, in Fig. 13(b), where the results of their simple calculation are also shown by solid and dotted curves. Ma *et al.* interpreted these spectra as arising from phonon relaxation [Jahn-Teller distortion in the (111) direction] of the core exciton, and they calculated the intensity of phonon structures in the RIXS spectrum by the Franck-Condon factors

$$\left|\int X_m(Q)X_n'(Q-Q_0)dQ\right|^2, \quad (29)$$

where X_n is the nth vibrational function of a harmonic potential and Q is the C-C stretching coordinate, using $Q_0=0.2$ Å, $n=8$, and $m=0-30$.

A more interesting calculation of these spectra was made by Tanaka and Kayanuma (1996). They used a small cluster model consisting of five C atoms with the

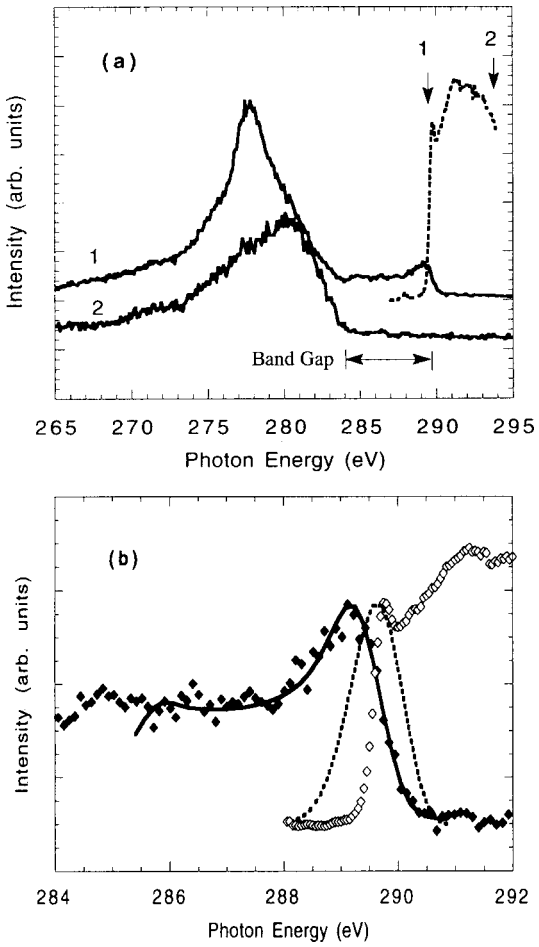

FIG. 13. Experimental and calculated C 1s spectra of diamond: (a) x-ray absorption (XAS) compared to RIXS spectra measured with excitation energies of 289.6 eV (curve 1) and 294.5 eV (curve 2); (b) XAS and RIXS spectra in the band-gap region; filled diamonds, experimental RIXS; open diamonds, XAS spectra; solid curve, the calculated Franck-Condon phonon spectra for RIXS; dashed curve, the calculated phonon-broadened absorption spectrum. From Ma *et al.*, 1993.

core excited atom at the center. For simplicity, they took into account the displacement of only the central atom in the (111) direction, which belongs to the T_2 irreducible representation of the T_d symmetry of the cluster. In the ground state the Hamiltonian is given by

$$H_0=\sum_{i=x,y,z}\frac{1}{2}(P_i^2+Q_i^2), \tag{30}$$

where Q_i denotes the coordinate for the T_2 local coupling mode and P_i means the momentum conjugate with Q_i. The x, y, and z directions are taken in the cubic axes of the diamond.

In the intermediate state, a C 1s electron in the central atom is excited to the antibonding orbitals between the sp^3 orbitals on the central and neighboring C atoms. If we consider only the four antibonding orbitals, the Hamiltonian is written as

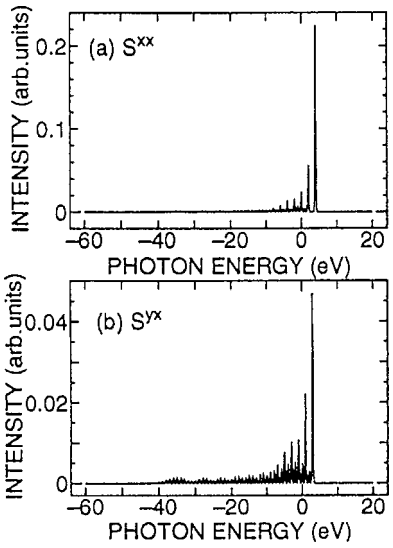

FIG. 14. Calculated RIXS spectra of diamond with the incident-photon energy at the core exciton peak. Two independent components, (x,x) and (y,x), are shown in (a) and (b). From Tanaka and Kayanuma, 1996.

$$H_e=\begin{pmatrix} \varepsilon_s & \alpha Q_x & \alpha Q_y & \alpha Q_z \\ \alpha Q_x & \varepsilon_p & -\beta Q_z & -\beta Q_y \\ \alpha Q_y & -\beta Q_z & \varepsilon_p & -\beta Q_x \\ \alpha Q_z & -\beta Q_y & -\beta Q_x & \varepsilon_p \end{pmatrix}+H_0, \tag{31}$$

where ε_s and ε_p are the core exciton energy with s and p symmetries, respectively, and α and β are the exciton-phonon coupling constants for the s and p symmetric states. The RIXS calculation is made by diagonalizing exactly the Hamiltonians H_0 and H_e, taking into account the vibronic effect. The results are shown in Fig. 14, where the incident-photon energy is taken at the core exciton peak of the x-ray absorption spectrum, and (a) and (b) are the spectra for two independent polarization components (x,x) and (y,x). These spectra show a conspicuous low-energy tail, similar to that of the experimental data. The origin of the tail is the so-called *hot luminescence*, which occurs just after the core exciton excitation, when the central C atom starts to displace in the (111) direction, and an x ray is emitted in the course of this displacement. In the calculation of Tanaka and Kayanuma the dissipation of the phonon energy is not explicitly taken into account, but since the core-hole lifetime is comparable with the dissipation time, the essential behavior of the resonant inelastic scattering spectrum will not be changed seriously by dissipation. They also calculated the x-ray absorption spectrum and showed that the width of the core exciton peak is as small as the experimental result, whereas the calculated width is smaller than the result of Ma *et al.* (see Fig. 13). This narrowing of the absorption peak can be explained by the vibronic effect for finite $\varepsilon_p-\varepsilon_s$, that is, the *dynamical pseudo Jahn-Teller effect.*

Phonon relaxation effects have also been found for normal x-ray emission in the wide-gap insulators, such as

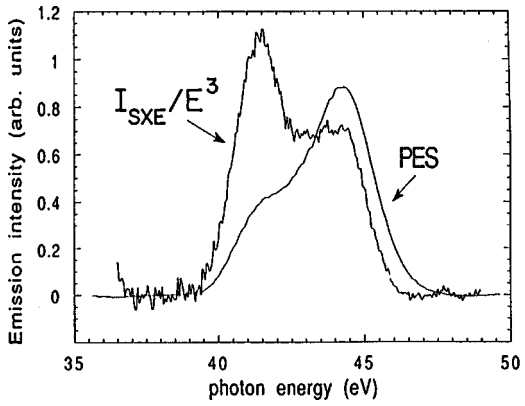

FIG. 15. Comparison of normal emission for soft x rays (SXE) and photoemission (PES) spectra of MgO. From O'Brien *et al.*, 1993a.

Al_2O_3, SiO_2, and MgO, by O'Brien *et al.* (1993a). They observed the valence-band structure from normal x-ray emission and compared it with the valence-band photoemission spectra. Figure 15 compares the Mg $2p$ NXES and photoemission for MgO. Both spectra show the same valence-band structure, and there are two structures with a good correspondence, though the difference in intensities is due to the difference in cross sections. However, one can find some energy shift between the two spectra. This shift (about 0.5 eV) seems to be due to phonon relaxation around a core hole and is known as a Stokes shift. Large Stokes shifts are also observed in Al_2O_3 (0.9 eV) and SiO_2 (1.2 eV), but no shift is observed in the Mg and Al metals or Si.

IV. RARE-EARTH SYSTEMS

A. Experimental data for rare-earth metals and compounds

In this subsection we show some typical examples of RIXS experimental data on rare-earth systems. In Figs. 16 and 17 (the curves indicated by "exp") are shown the RIXS spectra from the excitation Ce $3d\rightarrow4f\rightarrow3d$ of CeF_3 and CeO_2, respectively (Butorin, Mancini, *et al.*, 1996; Nakazawa *et al.*, 1996). In these data, the uppermost curve represents the Ce $3d$ x-ray absorption spectrum, where we see two prominent features which correspond to the Ce $3d_{3/2}$ and $3d_{5/2}$ core levels, and some fine structures in each feature. Then, the incident-photon energy Ω is tuned to the x-ray absorption structures A, B, and C, for CeF_3 for instance, and the observed RIXS spectra are depicted by the curves A, B, and C, respectively, in the lower panel as a function of the emitted photon energy ω. For CeF_3, the observed spectrum consists of a single peak at $\omega=\Omega$, corresponding to elastic x-ray scattering. For CeO_2, on the other hand, the spectrum consists of two peaks, corresponding to elastic and inelastic scattering. In this sense, these RIXS spectra of CeF_3 and CeO_2 are more appropriate by called resonant x-ray emession spectra.

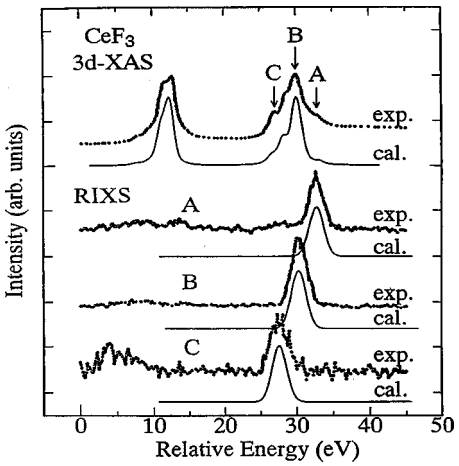

FIG. 16. Experimental and calculated results of Ce $3d$ absorption (XAS) and $3d\rightarrow4f\rightarrow3d$ RIXS for CeF_3. The RIXS results A, B, and C are obtained by tuning the incident-photon energy to A, B, and C of the absorption spectrum. From Nakazawa *et al.*, 1996.

As another example, we show in Fig. 18 the Tm $3d$ x-ray absorption spectrum and the fluorescence yield of the $3d\rightarrow4f\rightarrow3d$ RIXS in Tm metal (Pompa *et al.*, 1997; Nakazawa *et al.*, 1998). The fluorescence yield is the intensity of resonant x-ray emission (both elastic and inelastic x-ray scattering spectra) integrated over the emitted-photon energy and then measured as a function of the incident-photon energy. The observed fluorescence yield is similar to x-ray absorption, but we recognize a clear difference between them; the Tm $3d_{5/2}$ x-ray absorption spectrum shows three-peak structure, but the lowest energy peak is almost missing from the fluorescence yield.

Resonant inelastic x-ray scattering has also been measured for the rare-earth $4d$ and $2p$ core levels. Figure 19 shows the difference between the Nd $4d\rightarrow4f\rightarrow4d$ (upper panel) and $3d\rightarrow4f\rightarrow3d$ transition for Nd_2O_3

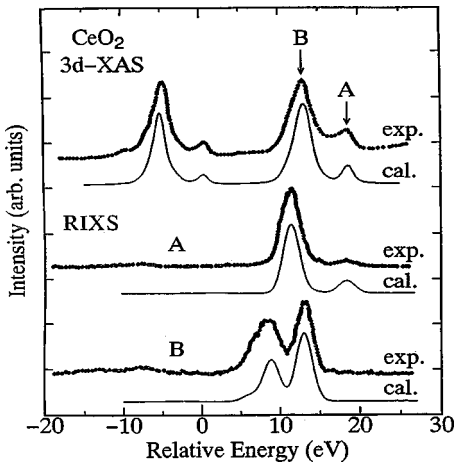

FIG. 17. Experimental and calculated results of Ce in CeO_2 analogous to Fig. 16. The RIXS results A and B are obtained by tuning the incident-photon energy to A and B of the absorption spectrum. From Nakazawa *et al.*, 1996.

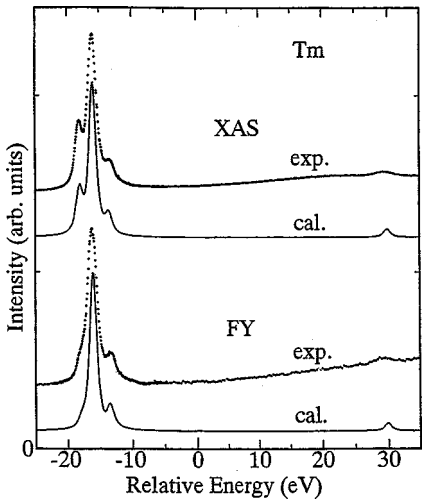

FIG. 18. Experimental and calculated x-ray absorption spectra (XAS) of Tm $3d_{5/2}$ and the corresponding total fluorescence yield (TY) of Tm metal. From Nakazawa *et al.*, 1998.

(Moewes *et al.*, 1999). The abscissa is the energy loss, which is defined here as the difference between the emitted-photon and incident-photon energies. In each panel the upper curve is the experimental result, where the incident-photon energy is taken to be 133.5 eV (for the $4d$ excitation) and 1002.4 eV (for the $3d$ excitation). It is to be noted that the final states of these RIXS processes are common but the observed spectra are different because of the difference in the intermediate states. Figure 20 displays the Dy $4d$ absorption spectrum (uppermost panel) and the Dy $4d \rightarrow 4f \rightarrow 4d$ RIXS spectra of DyF_3 for the incident-photon energies **a**–**m** (Butorin, Guo, *et al.*, 1997; Kotani, 1999). Figures 21(a)–(c) are concerned with the Dy $2p$ core excitation of $Dy(NO_3)_3$ (Hämäläinen *et al.*, 1991). In Fig. 21(a) the experimental

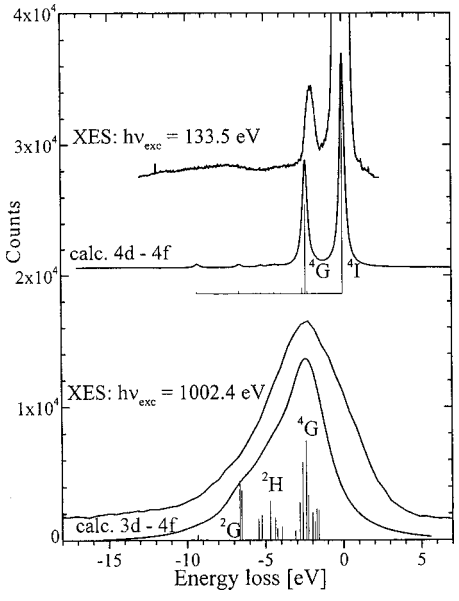

FIG. 19. Experimental and calculated resonant spectra for the Nd transitions $4d \rightarrow 4f \rightarrow 4d$ (upper panel) and $3d \rightarrow 4f \rightarrow 3d$ (lower panel) in Nd_2O_3. From Moewes *et al.*, 1999.

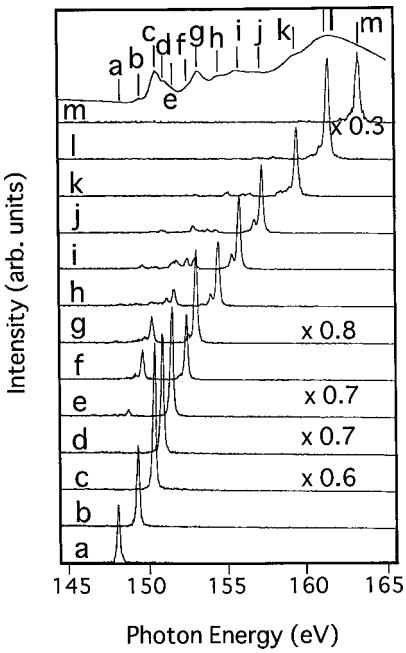

FIG. 20. Experimental spectra of Dy $4d$ absorption and $4d \rightarrow 4f \rightarrow 4d$ RIXS for DyF_3. From Butorin, Guo, *et al.*, 1997.

Dy fluorescence for the transition $3d_{5/2} \rightarrow 2p_{3/2}$ is shown, where a Dy $2p_{3/2}$ core electron is excited to the high-energy continuum, and then a Dy $3d_{5/2}$ electron makes a radiative transition to the $2p_{3/2}$ level. In this case, the emitted-photon energy is fixed at the maximum position of the normal emission spectrum with a high analyzer resolution (as high as 0.3 eV), as shown with the dotted curve, and the change in emitted-photon intensity is observed as a function of the incident-photon energy near the $2p_{3/2}$ threshold. The observed excitation spectrum is shown in Fig. 21(b) together with the Dy $2p$ absorption spectrum measured by the transmission method. As can be seen, the spectral width of the excitation spectrum is smaller than that of the absorption spectrum, and some weak structures are observed in the pre-edge region, which are invisible in conventional XAS. The observed pre-edge structure of the excitation spectrum is shown in Fig. 21(c) with an enhanced scale.

These experimental data indicate, as discussed in the following subsections, the importance of intra-atomic multiplet coupling, as well as of interatomic hybridization, in RIXS.

B. Effect of intra-atomic multiplet coupling

We consider first the case in which the system is well described by the atomic Hamiltonian, and the solid-state effect can be disregarded. One of the simplest examples is the Ce $3d$ absorption and $3d \rightarrow 4f \rightarrow 3d$ resonant emission of CeF_3 (Fig. 16), where Ce is well described by an isolated Ce^{3+} free ion and the process of resonant x-ray emission is described by the transitions $3d^{10}4f^1 \rightarrow 3d^9 4f^2 \rightarrow 3d^{10}4f^1$.

We show in Fig. 16 the calculated absorption and emission results (Nakazawa *et al.*, 1996) and compare

them with the experimental data. The $3d$ absorption spectrum shows the multiplet structure characteristic of the atomic $3d^9 4f^2$ configuration, for both the $3d_{3/2}$ and the $3d_{5/2}$ core levels. On the other hand, the emission spectra always show a single peak. This peak corresponds to elastic x-ray scattering without any inelastic x-ray scattering. This is because the final state ^2F in the $4f^1$ configuration is the same as the initial state (note that there is no multiplet splitting for the single-electron $4f^1$ configuration). More exactly, the initial state is the $^2F_{5/2}$ ground state, while the final state includes a $^2F_{7/2}$ excited state in addition to the ground state. However, the energy difference between the $^2F_{5/2}$ and $^2F_{7/2}$ states is about 0.3 eV ($4f$ spin-orbit splitting), which is too small (much smaller than the experimental resolution) to be resolved as an inelastic x-ray scattering spectrum.

As an example of the atomic multiplet effect in resonant x-ray emission, we consider Tm $3d$ absorption and emission in the $3d \rightarrow 4f \rightarrow 3d$ transition of Tm metal, where, again, Tm is well approximated by a free Tm^{3+} ion. We show in Fig. 22 the calculated results of Tm $3d$ x-ray absorption and $3d \rightarrow 4f \rightarrow 3d$ resonant emission (Nakazawa *et al.*, 1998). The ground state of Tm^{3+} (with $4f^{12}$ configuration) is the $^3H_6$ state. The Tm $3d$ absorption spectrum shows four peaks, A, B, C, and D, which correspond to the multiplet terms of the $3d^9 4f^{13}$ configuration; peak A corresponds to a pure $^3H_6$ term, peak B mainly to a $^3G_5$ term, while peaks C and D correspond to strongly mixed states between $^3H_5$ and $^1H_5$ terms due to the spin-orbit interaction. The resonant x-ray emission spectra with the incident-photon energy tuned to A, B, C, and D are shown in the lower panel of Fig. 22. It is found that for A and B the spectra are given mostly by an elastic x-ray scattering peak, where the final state is the same multiplet term $^3H_6$ as the ground state, while for C and D we have a strong inelastic x-ray scattering peak corresponding to a spin flip excited state $^1I_6$, in addition to the elastic scattering peak. This is because the x-ray absorption final states C and D are mixed states between $^1H_5$ and $^3H_5$, and then the $^1H_5$ component decays to the $^1I_6$ final state, while the $^3H_5$ component decays to the $^3H_6$ final state.

There has been no direct experimental observation of these resonant emission spectra in Tm^{3+}, but the fluorescence yield data shown in Fig. 18 strongly support this RXES process. The calculated fluorescence yield, which is obtained by integrating the calculated resonant x-ray emission (both elastic and inelastic x-ray scattering spectra; Fig. 22) over the emitted-photon energy, is in good agreement with the experimental result, as shown in Fig. 18. From this calculation it becomes clear why the lowest absorption peak A is missing from the fluorescence yield. If we take into account only the elastic x-ray scattering, we have a single dominant peak B in the fluorescence yield, because the intensity ratio of the three fluorescence yield peaks for the elastic x-ray scattering is roughly the square of that of that for the three absorption peaks. Then the contribution from the inelastic x-ray scattering to the fluorescence yield gives a peak at position C, but no peak at A because of almost vanishing inelastic x-ray scattering. In other words, the difference between the fluorescence yield and the absorption spectra comes from the fact that the radiative decay rate is not constant but depends on each intermediate state,

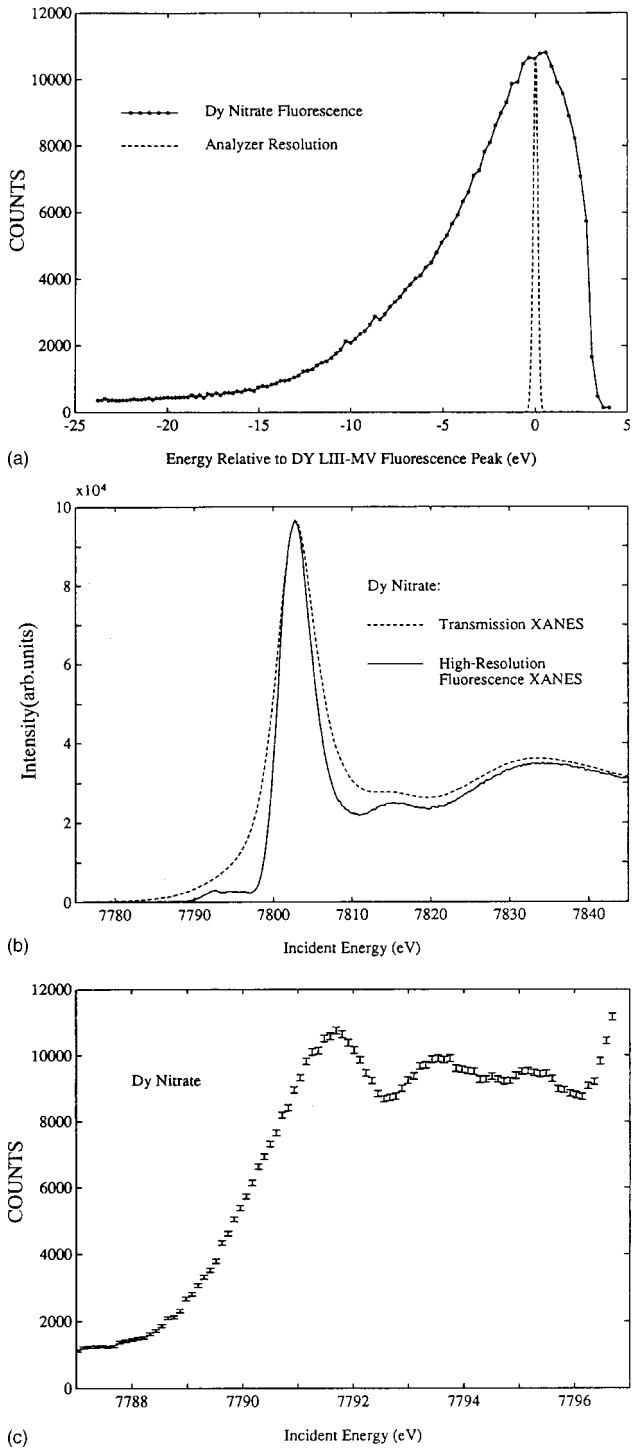

FIG. 21. Experimental results on dysprosium in Dy $(NO_3)_3$: (a) Dy normal x-ray emission (fluorescence) for the transition $3d_{5/2} \rightarrow 2p_{3/2}$; (b) Dy $2p_{3/2}$ absorption near-edge structure (XANES) and the corresponding excitation spectrum; (c) the enlarged pre-edge structure of the excitation spectrum. From Hämäläinen *et al.*, 1991. X-ray absorption near edge structure (XANES) is a common nomenclature for x-ray absorption (XAS) for energies close to the absorption edge.

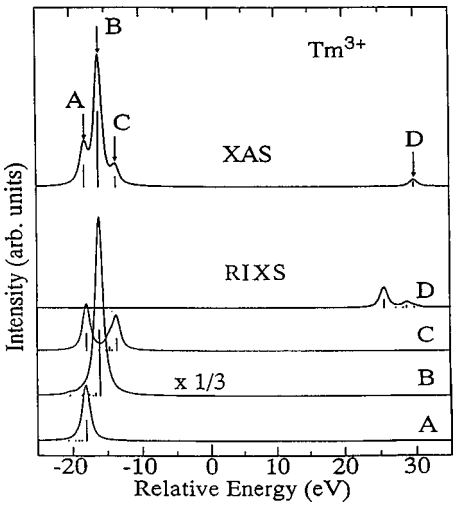

FIG. 22. Calculated results on $3d$ absorption and $3d \rightarrow 4f \rightarrow 3d$ RIXS for a Tm^{3+} ion. The RIXS spectra A, B, C, and D are obtained by tuning the incident-photon energy to A, B, C, and D of the absorption spectrum. From Nakazawa *et al.*, 1998.

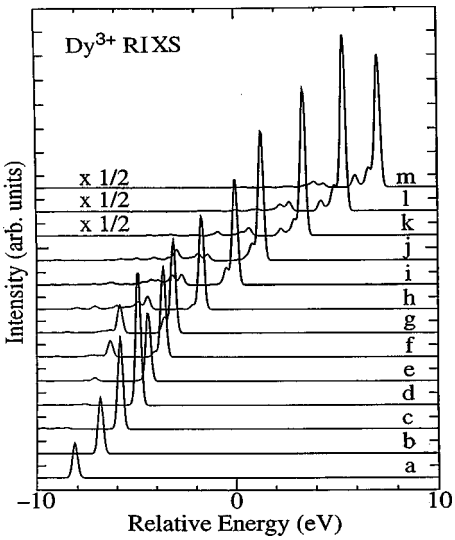

FIG. 23. Calculated $4d \rightarrow 4f \rightarrow 4d$ RIXS of a Dy^{3+} ion. From Nakazawa, 1998.

as discussed by de Groot, Arrio, *et al.* (1994) for different systems. van Veenendaal and Benoist (1998) calculated and compared $3d$ x-ray absorption spectra and fluorescence yield of $3d \rightarrow 4f \rightarrow 3d$ resonant emission of trivalent rare-earth ions from Ce to Yb, as well as their magnetic circular dichroism.

The RIXS of Nd_2O_3 shown in Fig. 19 can also be explained by the atomic multiplet effect. The ground state of a Nd^{3+} ion is in the ${}^4I_{9/2}$ state of the $4f^3$ configuration, and the final inelastic scattering states are ${}^4G$, ${}^2H$, ${}^2G \cdots$ states. The results of atomic calculations are also shown in Fig. 19 with the line spectra, as well as with the continuous spectra which are obtained by broadening the line spectra by 0.45 eV for the transition $4d \rightarrow 4f \rightarrow 4d$ and by 3.3 eV for the transition $3d \rightarrow 4f \rightarrow 3d$ (note that the resolution of the former is better than that of the latter because of the shallower core level). The difference between the $4d$ and $3d$ excitation spectra is due to the difference in the intermediate states. The ${}^4G$ final state is observed in both cases, because it is a spin-allowed transition, but ${}^2H$ and ${}^2G$ final states are spin forbidden, so their intensities are much stronger in the $3d$ excitation than in the $4d$ excitation because of the much stronger spin-orbit interaction in the $3d$ excited intermediate state.

In order to analyze precisely the inelastic scattering from the transition $4d \rightarrow 4f \rightarrow 4d$ in rare-earth systems, as in Fig. 20, it is necessary to take into account the Fano effect (Fano, 1961). Let us assume that the ground state $|g\rangle$ is in the $4d^{10}4f^n$ configuration. This state can be excited by the incident photon to the $4d^9 4f^{n+1}$ configuration (written hereafter as the state $|\alpha\rangle$) by the $4d \rightarrow 4f$ dipole transition T_1, as well as to the $4f^{n-1}\epsilon$ configuration ($|k\beta\rangle$, where k denotes the electron excited to the ionization continuum ϵ and β represents the $4f^{n-1}$ configuration) by the $4f \rightarrow \epsilon$ dipole transition T_2. The excited states $|\alpha\rangle$ and $|k\beta\rangle$ are coupled by the super Coster-Kronig transition T_A. X-ray emission occurs from $|\alpha\rangle$ to $|f\rangle$ (the $4f^n$ configuration) by the $4f \rightarrow 4d$ dipole transition T_3.

The RIXS spectrum is given by

$$F(\Omega,\omega) = \sum_f \left| \sum_{\alpha,\alpha'} \langle f|T_3|\alpha'\rangle\langle\alpha'|G|\alpha\rangle\langle\alpha|T_{eff}|g\rangle \right|^2 \times \delta(E_g + \Omega - E_f - \omega), \tag{32}$$

where

$$\langle\alpha'|G|\alpha\rangle = \langle\alpha'| \frac{1}{E_g + \Omega - H_0 - \Sigma} |\alpha\rangle. \tag{33}$$

Here H_0 is the atomic Hamiltonian without the transition T_A, and the self-energy operator Σ is defined by

$$\langle\alpha'|\Sigma|\alpha\rangle = \sum_{k\beta} \frac{\langle\alpha'|T_A|k\beta\rangle\langle k\beta|T_A|\alpha\rangle}{E_g + \Omega - E_{k\beta} + i\eta} \tag{34}$$

with $\eta \rightarrow +0$. The operator $T_{\rm eff}$ represents the effective transition operator from $|g\rangle$ to $|\alpha\rangle$:

$$\langle\alpha|T_{\rm eff}|g\rangle = \langle\alpha|T_1|g\rangle - i\pi \sum_{k\beta} \langle\alpha|T_A|k\beta\rangle \times \langle k\beta|T_2|g\rangle \delta(E_g + \Omega - E_{k\beta}). \tag{35}$$

The calculated result for Dy^{3+} resonant emission via the $4d \rightarrow 4f \rightarrow 4d$ channel (Butorin, Guo, *et al.*, 1997; Nakazawa, 1998; Kotani, 1999), which corresponds to the experimental RIXS spectra in Fig. 20, is shown in Fig. 23 (for the calculated Dy $4d$ absorption spectrum, see Ogasawara and Kotani, 1995). In each emission spectrum from **a** to **m**, the sharp peak at the highest emitted-photon energy corresponds to elastic x-ray scattering, while the structures on the lower-energy side are inelastic x-ray scattering spectra, caused by the atomic multiplet excitation. The calculated result is in good agreement with the experimental data. Similar experimental RIXS measurements of the transition $4d \rightarrow 4f \rightarrow 4d$ have also

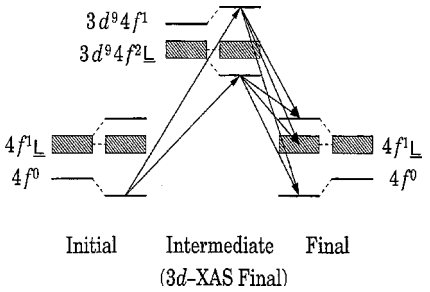

FIG. 24. Schematic energy-level diagram of the resonant $3d \rightarrow 4f \rightarrow 3d$ elastic and inelastic transitions for Ce in CeO_2.

been made for Gd^{3+} in $(Y,Gd)_2O_3$ by Moewes, Eskildson, *et al.* (1998). On the other hand, Gallet *et al.* (1996) have measured the Gd $5p \rightarrow 4d$ emission at the $4d \rightarrow 4f$ excitation threshold of Gd metal [see also similar RIXS measurements for BaF_2 by Rubensson *et al.* (1995)].

It should be mentioned that the atomic multiplet coupling and the Fano effect are important in explaining the $4d \rightarrow 4f \rightarrow 4d$ RIXS spectrum of rare-earth compounds, while the Fano effect is not important in $3d$ XAS and $3d \rightarrow 4f \rightarrow 3d$ RIXS spectra because the transition T_A is weak.

C. Effect of interatomic hybridization

In contrast to CeF_3, the Ce $4f$ state in CeO_2 is strongly mixed with the O $2p$ states by covalency hybridization (Kotani *et al.*, 1985, 1988). Therefore, in the calculation of the Ce $3d$ x-ray absorption spectrum and RIXS of CeO_2, it is essential to use the Anderson impurity model instead of the free-atom model. The experimental result (Fig. 17; Butorin, Mancini, *et al.*, 1996) has been analyzed theoretically by Nakazawa *et al.* (1996) with the Anderson impurity model. The calculated spectra are also shown in Fig. 17, and good agreement can be seen between the calculated and experimental results.

The total energy-level scheme of CeO_2 is shown schematically in Fig. 24. The ground state is a bonding state between $4f^0$ and $4f^1\underline{L}$ configurations ($\underline{L}$ being a hole in the valence band), and the intermediate states are bonding, antibonding, and nonbonding states between the $3d^9 4f^1$ and $3d^9 4f^2\underline{L}$ configurations. The main peak B and the satellite A of the $3d$ absorption spectrum correspond to the transitions to bonding and antibonding states, respectively, while the transition to the nonbonding state is almost forbidden. The final states of the $3d \rightarrow 4f \rightarrow 3d$ resonant emission spectrum have the same configuration as the initial one, and it is possible to make a transition to both nonbonding and antibonding states, in addition to the bonding state (i.e., the ground state) which corresponds to elastic x-ray scattering. When Ω is fixed at the main peak position, which corresponds to selecting the bonding state in the intermediate state, we have a strong transition to the bonding state, a somewhat weaker transition to the nonbonding state, and a weak transition to the antibonding state in the final state. When Ω is fixed at the satellite peak position, which corresponds to the antibonding state in the intermediate state, we have a strong transition to the antibonding state and a weak transition to the bonding state. This is the reason why the spectrum in CeO_2 has a two-peak structure. The difference in the relative intensity of the two peaks for different Ω originates from the different character of the intermediate states.

When the incident-photon energy is tuned to the satellite peak A of the $3d$ x-ray absorption spectrum of CeO_2, the antibonding state between $3d^9 4f^1$ and $3d^9 4f^2\underline{L}$ configurations is selectively excited as the intermediate state. If this intermediate state decays to the ground state (bonding state between $4f^0$ and $4f^1\underline{L}$ configurations), we have an elastic x-ray scattering peak, while if it decays to the excited state (antibonding state between $4f^0$ and $4f^1\underline{L}$ configurations), we have an RIXS peak. The ratio between the elastic and inelastic x-ray scattering peaks depends on the intermediate state, reflecting the different character of the intermediate states.

It can be clearly seen from the x-ray absorption and resonant emission (curve A in Fig. 17) that the energy difference of the two absorption peaks is smaller than that of the peaks in the resonant emission spectrum. Therefore the energy difference between the antibonding and bonding states with a core hole is smaller than that without a core hole. It is to be noted that these energy differences are mainly determined by covalency hybridization. Therefore the covalency hybridization strength V is smaller with a core hole than without a core hole. This is because the $4f$ wave function is contracted by the attractive potential of the core hole. We define the reduction factor R_c by

$$V(\text{with core hole}) = R_c \times V(\text{without core hole}).$$

The value of R_c, as well as the other parameters of the Anderson impurity model, can be estimated by analyzing the resonant x-ray emission (and absorption) spectra. The estimated values are $R_c = 0.6$, V (without core hole) $= 1.0$ eV, $\Delta = 2.0$ eV, $U_{ff} = 9.0$ eV, and $U_{fc} = 12.6$ eV (Butorin, Mancini, *et al.*, 1996; Nakazawa *et al.*, 1996).

There have been many experimental data for x-ray absorption and x-ray photoemission associated with various core levels in CeO_2, and most of them were successfully reproduced by theoretical calculations using the Anderson impurity model with $R_c = 1.0$ (the other parameters are $V = 0.76$ eV, $\Delta = 1.6$ eV, $U_{ff} = 10.5$ eV, and $U_{fc} = 12.5$ eV; Kotani *et al.*, 1988; Kotani and Ogasawara, 1992). The only exception is the analysis of valence x-ray photoemission spectroscopy (VXPS) and bremsstrahlung isochromat spectroscopy (BIS). According to the experimental results of VXPS and BIS for CeO_2 (Wuilloud *et al.*, 1984), the energy difference between the lowest affinity state and the first ionization state is about 4.5 eV, which corresponds to the insulating energy gap of CeO_2. A previous calculation (Nakano *et al.*, 1987) of VXPS and BIS with $R_c = 1.0$ gave an insulating gap (about 2.0 eV) much smaller than the experimental value. Then Nakazawa *et al.* (1996) calcu-

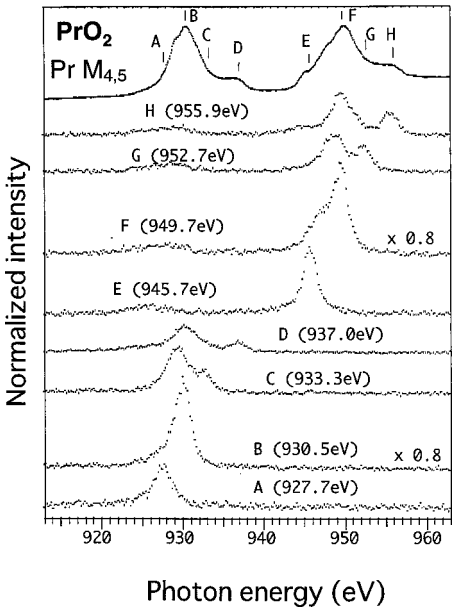

FIG. 25. Experimental spectrum of Pr $3d$ absorption and Pr $3d \rightarrow 4f \rightarrow 3d$ RIXS in PrO_2. In the RIXS results A–H, the incident-photon energy is tuned to the energy positions A–H in the absorption spectrum. From Butorin *et al.*, 1997b.

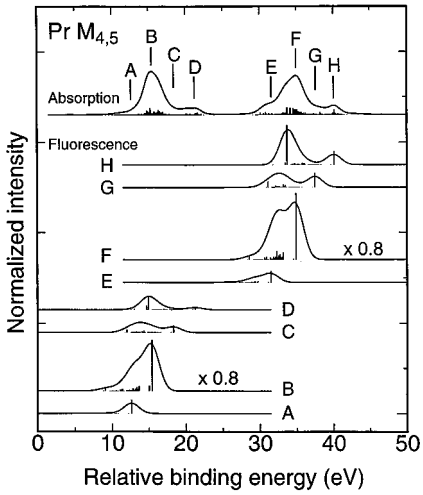

FIG. 26. Calculated RIXS spectra for the Pr $3d \rightarrow 4f \rightarrow 3d$ transition in PrO_2. From Butorin, Duda, *et al.*, 1997.

lated the valence photoemission and bremsstrahlung isochromat spectra with their new parameters with $R_c = 0.6$, and found that the experimental value of the insulating energy gap was well reproduced by their calculation. It was also checked that the other experimental data, the Ce $3d$ x-ray photoemission, $4d$ absorption, and $4d$ photoemission spectra for CeO_2, were well reproduced by the new parameter values. In this way, the resonant emission spectroscopy gives us important information on the hybridization strength in both the ground-state configuration and the core electron excited state.

More recently Butorin, Duda, *et al.* (1997) measured a similar inelastic scattering spectrum for PrO_2, and analyzed the result with the Andersion impurity model. The experimental and theoretical results are shown in Figs. 25 and 26, respectively. The ground state of PrO_2 is a bonding state between $4f^1$ and $4f^2\underline{L}$ configurations, and the final state of the Pr $3d$ x-ray absorption consists of bonding and antibonding states between $3d^9 4f^2$ and $3d^9 4f^3 \underline{L}$ configurations. The main peak in the region A, B, and C (and also E, F, and G) is the bonding state with some multiplet structure, and the satellite D (and H) corresponds to the antibonding state. The resonant inelastic scattering spectra A–H are obtained by tuning the incident-photon energy to the absorption spectra positions A–H, and the calculated results are in fair agreement with the experimental ones. The parameter values used are $V = 0.8$, $\Delta = 0.5$, and $U_{fc} - U_{ff} = 5.0$ (in units of eV), and the reduction factor $R_c = 0.7$ is essential in reproducing the experimental results. It is to be stressed that the interplay between the interatomic hybridization and the intra-atomic multiplet coupling plays an essential role in the RIXS of PrO_2, while the latter is less important in CeO_2.

It is well known that some intermetallic compounds of Ce, as well as those of Yb, exhibit anomalous physical properties such as mixed valence (or valence fluctuation), heavy fermions, Kondo insulators, and other behaviors (Bickers *et al.*, 1985; Lawrence *et al.*, 1985; Susaki *et al.*, 1996). In order to explain these properties, the Anderson impurity model, as well as a periodic Anderson model, has been widely used. Especially for the study of mixed-valence states in intermetallic Ce compounds, Anderson impurity model analysis for x-ray photoemission and absorption data has played an essential role. For instance, Gunnarsson and Schönhammer (1983) analyzed x-ray photoemission data of various Ce compounds with the Anderson impurity model by using the $1/N_f$ expansion method, in which the spectral intensity is expanded in a power series of $1/N_f$, where N_f is the degeneracy number of the $4f$ state (Gunnarsson and Schönhammer, 1983; Allen *et al.*, 1986). From the analysis, they could estimate the average $4f$ electron number n_f in the ground state of various mixed-valence Ce compounds and revealed that the value n_f is almost always larger than about 0.7, ranging mainly between 0.8 and 1.0. More recently, however, it has been found that surface Ce states give a different contribution to the x-ray photoemission from that of the bulk Ce states (Laubschat *et al.*, 1990; Braicovich, Brookes, *et al.*, 1997), so that we need to take into account the surface contribution in the analysis of x-ray photoemission.

It is to be noted that the RIXS is free from surface contributions. Therefore it is very useful to apply the RIXS technique to studying the electronic states of metallic Ce compounds. So far, only a small number of such experiments have been performed with almost no theoretical analysis. As an example, we show in Fig. 27 the resonant emission spectra for the transition $4d \rightarrow 4f \rightarrow 4d$ of CeB_6 (Butorin *et al.*, 1999). The upper panel shows the total fluorescence yield, and the RIXS spectra are displayed in the lower panel for the incident-photon energy indicated by arrows in the upper panel. The lowest inelastic-scattering structure has an energy loss of about 3.7 eV, the origin of which is interpreted as the

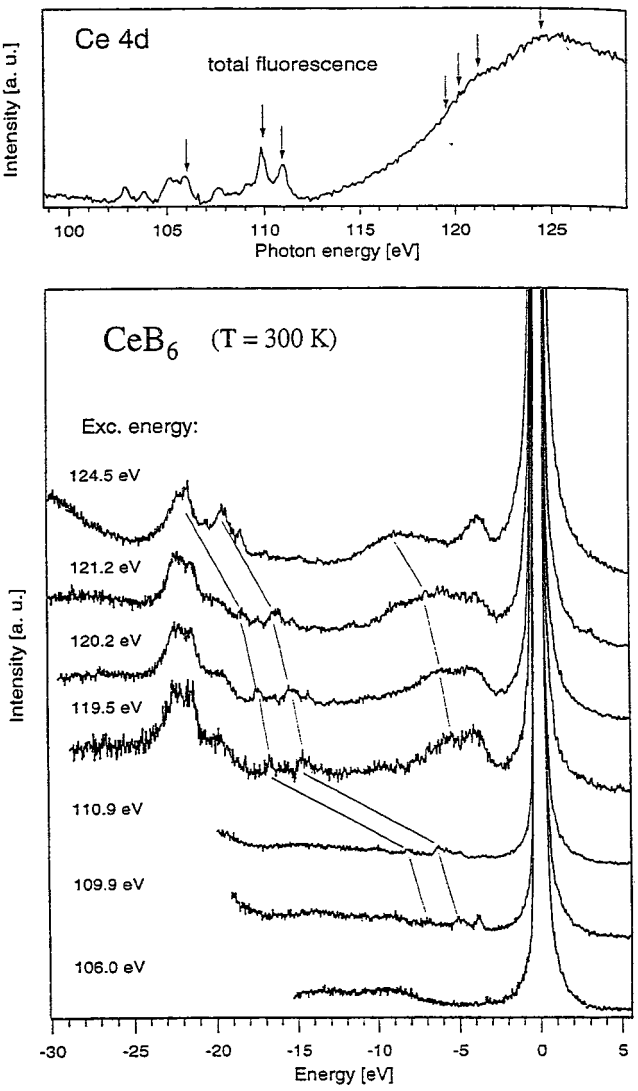

FIG. 27. Experimental RIXS spectra for the Ce $4d \rightarrow 4f \rightarrow 4d$ transition in CeB_6. The elastic peak is set at 0 eV. The excitation energies used to obtain these spectra are indicated by arrows on the total fluorescence spectrum at the $4d$ edge shown in the upper panel. From Butorin *et al.*, 1999.

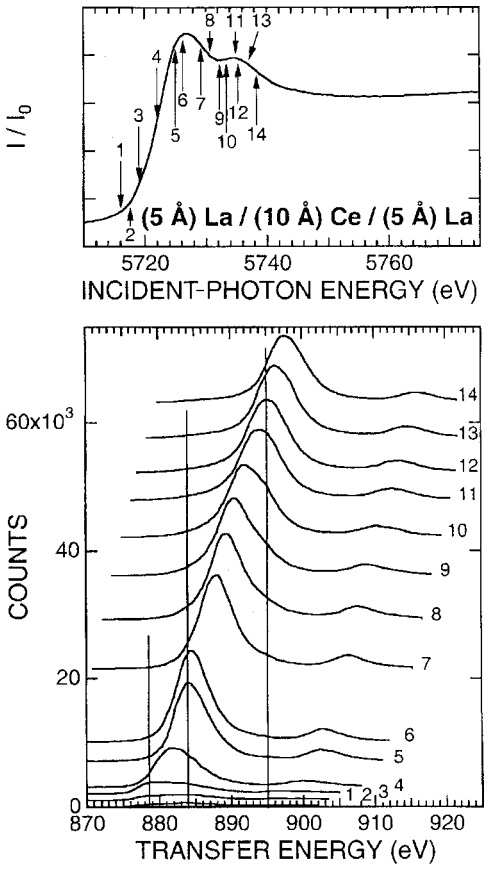

FIG. 28. Experimental RIXS data on the Ce $3d_{5/2} \rightarrow 2p_{3/2}$ transition at the Ce $2p_{3/2}$ excitation threshold of a [(5 Å) La/(10 Å) Ce/(5 Å) La/(30 Å) Fe]$\times n$ multilayer. The incident-photon energies are indicated by arrows on the Ce $2p_{3/2}$ absorption spectrum in the upper panel. From Mariot *et al.*, 1999.

excitation of the f^2 configuration in the final state in a more recent paper by Magnuson *et al.* (2001). Another example of RIXS in mixed-valence Ce systems has been measured for multilayer samples. Figure 28 shows the Ce $3d \rightarrow 2p$ RIXS under the $2p \rightarrow 5d$ resonant excitation for a [(5 Å) La/(10 Å) Ce/(5 Å) La/(30 Å) Fe]$\times n$ multilayer (Mariot *et al.*, 1999). The upper panel shows the Ce $2p \rightarrow 5d$ x-ray absorption spectrum, which exhibits a double-peak structure characteristic of the mixed-valence Ce systems. The observed transfer energy of the RIXS peak depends strongly on the incident-photon energy, and Mariot *et al.* interpreted the transfer energy of about 884 eV as corresponding to the Ce $4f^1$ configuration and that of about 895 eV as corresponding to the Ce $4f^0$ configuration. The Ce $3d \rightarrow 4f \rightarrow 3d$ resonant inelastic scattering spectrum for a [(10 Å) Ce/(30 Å) Fe]$\times n$ multilayer has also been measured by Journel *et al.* (1999).

In mixed-valence systems hybridization between $4f^n$ and $4f^{n+1}$ configurations ($n=0$ for Ce) occurs in the ground state. It is to be noted that even in some integral valence systems, hybridization between $4f^n\underline{c}$ and $4f^{n+1}\underline{c}$ configurations can occur in the intermediate state of normal x-ray emission (i.e., the final state of x-ray photoemission). This is well known in the photoemission spectroscopy of various rare-earth oxides (see Kotani and Ogasawara, 1992). For these systems therefore a charge-transfer excitation due to hybridization may be observed in NXES. Moewes, Stadler, *et al.* (1998) measured this type of charge-transfer excitation in NXES by the $3d$ core excitation of Nd_2O_3 and $LaAlO_2$, and found a charge-transfer energy of 2.3 eV for Nd_2O_3 and 7.5 eV for $LaAlO_2$.

It is highly desirable that high-resolution RIXS measurements be performed for other mixed-valence systems, heavy-fermion systems, and Kondo insulators, and also that they be analyzed theoretically in the future.

D. Narrowing of spectral width in the excitation spectrum

In the conventional $2p_{3/2}(L_3)$ absorption spectroscopy of rare earths, in general, the spectrum is broadened by a short lifetime of the $2p$ core hole, so that fine

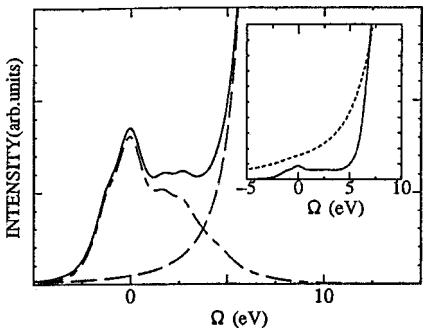

FIG. 29. Calculated excitation spectrum in the pre-edge region of L_3 for a Dy^{3+} system. The total spectrum (solid curve) consists of the quadrupole (dot-dashed curve) and dipole (long-dashed curve) contributions. In the inset, the calculated excitation spectrum (solid curve) is compared with the theoretical result of the conventional XAS (short-dashed curve). From Kotani, 1993.

structures in $2p$ absorption spectra are often smeared out. However, Hämäläinen *et al.* (1991) attained a dramatic improvement in resolution far beyond the limit imposed by the $2p_{3/2}$ core hole lifetime in the excitation spectrum of Dy $3d_{5/2} \rightarrow 2p_{3/2}$ RIXS for $Dy(NO_3)_3$ in the region of the Dy $3d_{5/2} \rightarrow 2p_{3/2}$ absorption edge. With this technique, they revealed a fine pre-edge structure of Dy $2p_{3/2}$ edge which is invisible using the conventional x-ray absorption spectroscopy technique, and interpreted this structure as originating from the $2p_{3/2} \rightarrow 4f$ optical quadrupole transition.

Theoretical analysis of these experimental data was made by Tanaka *et al.* (1994) in the pre-edge region of Dy $2p_{3/2}$ x-ray absorption for the Dy^{3+} system. With the incident- and emitted-photon energies Ω and ω, respectively, the excitation spectrum is given, from Eq. (5), by

$$F(\Omega,\omega)=\sum_j \left| \sum_i \frac{\langle j|T_2^\dagger|i\rangle\langle i|T_1|g\rangle}{E_g+\Omega-E_i-i\Gamma_L} \right|^2 \times \frac{\Gamma_M/\pi}{(E_j+\omega-E_g-\Omega)^2+\Gamma_M^2}, \tag{36}$$

where T_1 represents both the $2p_{3/2} \rightarrow 4f$ quadrupole transition and the $2p_{3/2} \rightarrow 5d$ dipole transition, T_2 represents the $3d_{5/2} \rightarrow 2p_{3/2}$ dipole transition, and Γ_L and Γ_M represent the lifetime broadening of the $2p_{3/2}$ and $3d_{5/2}$ core holes, respectively. The values of Γ_L and Γ_M are taken to be 2.1 and 0.7 eV, respectively. The intra-atomic multiplet coupling between $4f$ electrons, that between $4f$ electrons and $2p$ hole (in the intermediate state), and that between $4f$ electrons and $3d$ hole (in the final state) are fully taken into account.

The calculated excitation spectrum in the $2p_{3/2}$ pre-edge region is shown in Fig. 29 (Kotani, 1993; Tanaka *et al.*, 1994) by the solid curve, where the energy ω is fixed at the peak position of the normal x-ray emission spectrum for the transition $3d_{5/2} \rightarrow 2p_{3/2}$ under x-ray excitation well above the $2p_{3/2}$ absorption edge. The spectrum consists of the two contributions: the quadrupole excitation (dot-dashed curve) and the low-energy tail of the $2p_{3/2} \rightarrow 5d$ dipole excitation (long-dashed curve).

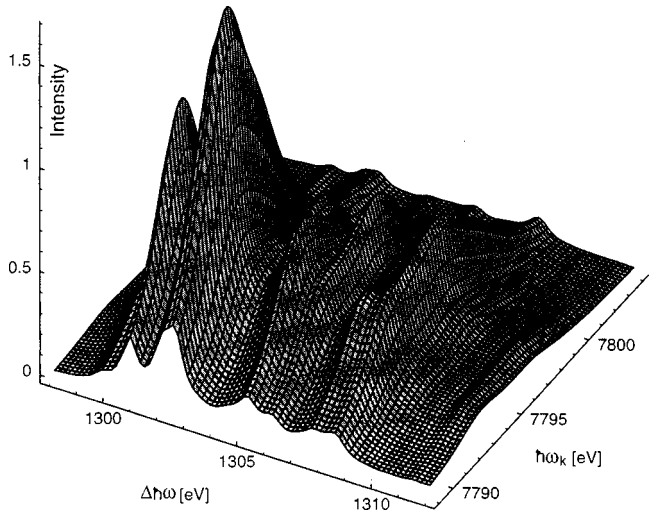

FIG. 30. Calculated RIXS result for the $3d_{5/2} \rightarrow 2p_{3/2}$ transition in the $2p_{3/2} \rightarrow 4f$ excitation due to the quadrupole transition of a free Dy^{3+} ion. The intensity of the inelastic scattering is shown as a function of the incident and transferred photon energies. From Carra *et al.*, 1995.

The dipole excitation is calculated by assuming that the density of states of the Dy $5d$ conduction band is given by a semielliptic shape, for simplicity. The conventional absorption spectrum is also calculated with the same model, and the result is shown in the inset of Fig. 29 with the short-dashed curve and compared with the excitation spectrum (solid curve). The pre-edge structure which can be clearly seen in the excitation spectrum is invisible in the conventional absorption spectrum. These results are in good agreement with the experimental results of Hämäläinen *et al.* [1991; Figs. 21(b) and (c)]. The calculated excitation spectrum corresponds to a fictitious x-ray absorption spectrum with a spectral width smaller than the conventional one.

A similar calculation was also made by Carra *et al.* (1995). In Fig. 30 their result is shown, where the RIXS intensity due to the $2p_{3/2} \rightarrow 4f$ quadrupole excitation and $3d_{5/2} \rightarrow 2p_{3/2}$ dipole x-ray emission is displayed as a function of incident-photon energy Ω (written as $\hbar\omega_k$ in the figure) and the transferred photon energy $\Omega-\omega$ (written as $\Delta\hbar\omega$). The values of Γ_L and Γ_M are taken as 2 and 0.15 eV, respectively. As can be seen from Eq. (36), parallel to the $\Omega-\omega$ axis, the final-state structure is scanned with the resolution Γ_M, while parallel to the Ω axis it is scanned with the resolution Γ_L. Keeping ω fixed, while varying Ω, as performed by Hämäläinen *et al.* (1991), amounts to moving along the 45° line in the Ω and $\Omega-\omega$ plane of Fig. 30. In this case, if the condition $\Gamma_L \gg \Gamma_M$ is satisfied, the spectral broadening is controlled by Γ_M. As shown by Tanaka *et al.*, the observed excitation spectrum tends to the Dy $2p_{3/2}$ absorption spectrum simply with a smaller spectral width Γ_M, when the following three conditions are fulfilled: (a) The multiplet coupling between the core hole (both $2p_{3/2}$ and of $3d_{5/2}$) and the $4f$ electrons is much smaller than that between $4f$ electrons. (b) Γ_M is much smaller than Γ_L. (c) The x-ray emission energy ω is taken as the difference of the

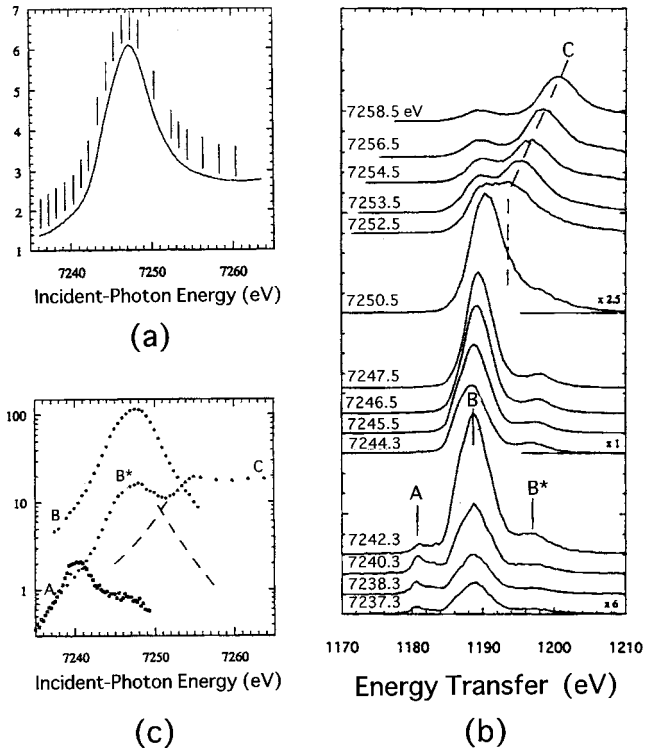

FIG. 31. Experimental results: (a) Gd $2p_{3/2}$ x-ray absorption in $Gd_3Ga_5O_{12}$ garnet, (b) RIXS in the transition Gd $3d_{5/2} \rightarrow 2p_{3/2}$ with various incident-photon energies, and (c) intensity of RIXS for the structures A, B, B*, and C as a function of the incident-photon energy. From Krisch *et al.*, 1995.

binding energies between $2p_{3/2}$ and $3d_{5/2}$ core levels.

In actual Dy^{3+} compounds, conditions (a) and (b) are satisfied approximately, although they are not satisfied exactly. Therefore the structure of the excitation spectrum does not coincide with that of the narrower absorption spectrum in the strict sense, but there is a good correspondence between them. As a matter of fact, Loeffen *et al.* (1996) compared a similar excitation spectrum observed for $Ho(NO_3)_3$ with a deconvolved Ho $2p_{3/2}$ absorption spectrum of the same material, and found that the excitation spectrum reproduced broadly the deconvolved spectrum, but lacked some structure on the higher-energy side of the white line. Moreover the pre-edge feature of the excitation spectrum (by the quadrupole transition) was weaker and offset by about 1.7 eV.

Another way to separate the quadrupole and dipole excitations in $2p$ absorption spectra of rare-earth systems is to measure RIXS as a function of Ω with a fixed energy transfer $\Omega - \omega$. An example is given in Fig. 31 for Gd in $Gd_3Ga_5O_{12}$ garnet as measured by Krisch *et al.* (1995). Figure 31(a) shows the experimental x-ray absorption of the Gd $2p_{3/2}$ spectrum, and Fig. 31(b) shows the RIXS for Gd $3d_{5/2} \rightarrow 2p_{3/2}$, where the incident-photon energy is fixed to various values [positions shown with bars in Fig. 31(a)]. A and B in Fig. 31(b) represent the RIXS originating from the Gd $2p_{3/2} \rightarrow 4f$ quadrupole excitation and the Gd $2p_{3/2} \rightarrow 5d$ dipole excitation, respectively, and they are separately observed because of the large difference in their final-state energies. Then, by taking the energy transfer at A and B, the RIXS intensity is shown as a function of Ω in Fig. 31(c). The maxima of the curves A and B in Fig. 31(c) correspond to the intensity maxima of the absorption spectrum due to the quadrupole and dipole transitions, respectively. We cannot see the quadrupole contribution in Fig. 31(a), but we can estimate the intensity and energy position of the quadrupole transition from Fig. 31(c). It should be mentioned that the structure B* is an exchange satellite of B, so that the relative intensity between B* and B are almost constant with the change in incident-photon energy in Fig. 31(c). The structure C behaves as normal x-ray emission, where ω is constant instead of $\Omega - \omega$, because the incident-photon energy is in the high-energy continuum of the x-ray absorption spectrum. More recently, Iwazumi *et al.* (1998) made similar measurements for Gd in the ferrimagnetic Gd-Co compounds, and Krisch *et al.* (1996) and Iwazumi *et al.* (1998) observed the dependence of RIXS in Gd on circularly polarized incident photons.

Systematic measurements in a manner similar to that leading to curves A and B, in Fig. 31(c) have been made by Bartolomé *et al.* (1997) for the rare earths $R = $Nd, Sm, Gd, Tb, Dy, Ho, Er, and Tm in $R_2Fe_{14}B$. They determined the quadrupole and dipole excitation energies in the $2p_{3/2}$ absorption, and compared them with the structures observed in magnetic circular dichroism (MCD) of the XAS. It is interesting that they could observe a double-peak structure in the quadrupole transition of the light rare-earth systems Nd and Sm, which correspond to the spin-up and spin-down transition with respect to the ground-state spin direction. A similar experiment was also made by Gallet *et al.* (1999) for Sm metal. In the magnetic circular dichroism of rare-earth $2p$ absorption, the assignment of the observed structures (including the dipole and quadrupole contributions) has not been well established, so that the information given by RIXS is very important.

E. Polarization dependence and magnetic circular dichroism

In all the calculations (except for the case of Tm) given in Sec. IV, the polarization dependence of resonant x-ray emission (both elastic and inelastic scattering) is disregarded for simplicity by taking the average of the emission spectra over all polarization directions, x, y, and z for both incident and emitted photons. In actual experiments, it is not easy to measure the polarization of the emitted photon as well as the dependence of the resonant emission spectrum on the angle between incident- and emitted-photon propagation directions. In general, the emission spectrum depends, more or less, on the polarization direction and the scattering angle.

The fluorescence yield in Tm (Fig. 18) was measured with the geometrical arrangement shown in Fig. 32. The polarization of the incident photon is in the z direction, and the scattering angle θ is 90°. If we assume the incident-photon polarization in the z direction and take

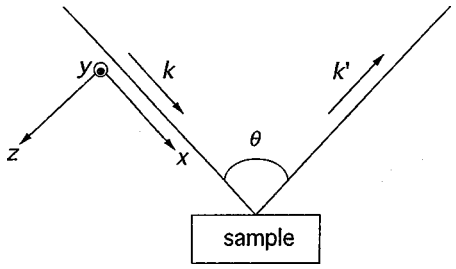

FIG. 32. Geometrical arrangement of RIXS.

a general scattering angle θ, the resonant emission spectrum is expressed as (Nakazawa *et al.*, 1998)

$$F(\Omega,\omega)=\sum_q \sum_j \left| \sum_i \frac{\langle j|C_q^{(1)}|i\rangle\langle i|C_0^{(1)}|g\rangle}{E_g+\Omega-E_i-i\Gamma_i} \right|^2 \times A_q(\theta)\,\delta(E_g+\Omega-E_j-\omega), \tag{37}$$

where $C_q^{(k)}$ is defined by

$$C_q^{(k)}=\sqrt{\frac{4\pi}{2k+1}}Y_{kq} \tag{38}$$

with the spherical harmonics Y_{kq}, and the angle-dependent factor $A_q(\theta)$ is given by

$$A_q(\theta)=\begin{cases} \frac{1}{2}(1+\sin^2\theta) & q=1,-1, \\ \cos^2\theta & q=0. \end{cases} \tag{39}$$

The intensity of the fluorescence yield is given by integrating the emission spectrum $F(\Omega,\omega)$ over the emitted-photon energy ω:

$$F_{\mathrm{FY}}(\Omega)=\int d\omega F(\Omega,\omega)=\sum_q f_q(\Omega)A_q(\theta), \tag{40}$$

where

$$f_q(\Omega)=\sum_j \left| \sum_i \frac{\langle j|C_q^{(1)}|i\rangle\langle i|C_0^{(1)}|g\rangle}{E_g+\Omega-E_i-i\Gamma_i} \right|^2. \tag{41}$$

The calculated fluorescence yield and RIXS with these expressions ($\theta=90°$) were shown in Figs. 18 and 22. According to the experiments of Pompa *et al.* (1997), the θ dependence of the fluorescence yield is very small for Tm^{3+}, but considerably larger for Sm^{3+}. The experimental and theoretical θ dependence of the fluorescence yield (for the $3d_{5/2}$ core level) of Sm are compared in Fig. 33. Nakazawa *et al.* (1998) observed that as a general trend the difference between f_0 and $f_{\pm1}$ is large for rare-earth elements with the $4f$ shell less than half filled and small for those that are more than half filled. Their calculated results for Tm^{3+} and Sm^{3+} show that the relative weights of f_0 and $f_{\pm1}$ depend on θ, thus explaining the observations of differing fluorescence yield for Tm^{3+} and Sm^{3+}.

Polarization dependence is one of the most important and useful aspects of RIXS. Since it is a coherent second-order process, there are selection rules involving both incident and outgoing photons, analogous to those of Raman scattering. The observed polarization dependences of the scattering can be used to sort out the symmetries of the excitations and mechanism for electron-light and electron-electron coupling. Examples include the excitation of the Ce $4f$ electrons in CeO_2 and Ti $3d$ electrons in TiO_2 (see Sec. V.C), where the polarization dependence was used to make predictions and comparisons with experiment on resonent x-ray emission (both elastic and inelastic scattering spectra) and x-ray absorption. Let us discuss the difference in the emission spectra of CeO_2 with the polarized and depolarized configurations introduced in Sec. II.B. We consider the geometry shown in Fig. 32 with $\theta=90°$. The incident-photon polarization is in the y direction for the polarized and in the z direction for the depolarized configuration. The experimental results in Fig. 17 were observed with the polarized configuration, but what happens if we use the depolarized configuration? From Eqs. (37) and (39), $F(\Omega,\omega)$ is written, for the depolarized configuration, as

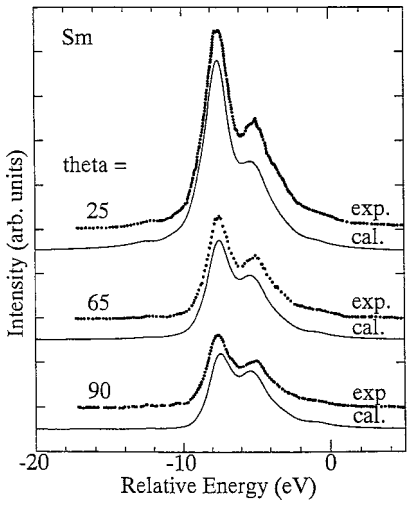

FIG. 33. Experimental and calculated scattering angle dependence of the fluorescence yield for Sm. From Nakazawa *et al.*, 1998.

$$F(\Omega,\omega)=\sum_{q=\pm1} \sum_j \left| \sum_i \frac{\langle j|C_q^{(1)}|i\rangle\langle i|C_0^{(1)}|g\rangle}{E_g+\Omega-E_i-i\Gamma_i} \right|^2 \times \delta(E_g+\Omega-E_j-\omega). \tag{42}$$

Then the elastic scattering spectrum is found to be forbidden, because the total angular momentum $J=0$ (so that $J_z=0$) in $|g\rangle$ of CeO_2 and $|j\rangle=|g\rangle$ for elastic x-ray scattering. Note that in order to obtain a finite RIXS intensity in Eq. (42) the J_z of $|j\rangle$ should be 1 or -1. Since the antibonding state between $4f^0$ and $4f^1\underline{L}$ configurations (i.e., the final state of the inelastic scattering in curve A of Fig. 17) is also the state with $J=J_z=0$, this peak disappears in the depolarized configuration. On the other hand, the nonbonding states (the main part of inelastic scattering in curve B) do not disappear because they have finite values of J_z including ±1 (see, for further details, a recent paper by Nakazawa *et al.*, 2000). Very recent experimental measurements of resonant emission in CeO_2 with the depolarized configuration are consistent with this expectation (Watanabe *et al.*, 2000)

and give strong support for the present interpretation of resonant emission using the Anderson impurite model, although the result has not as yet been published.

Another interesting phenomenon that has some bearing on the polarization dependence of XES is magnetic circular dichroism (MCD) in ferromagnetic systems. Pioneering work in this field was done by Hague and co-workers. The first experimental observation of MCD in XES was made by Hague *et al.* (1993) for the $2p$ edge of Fe metal, and the result was compared with calculations using the fully relativistic local spin-density approximation (LSDA). This work will be described in greater detail in Sec. VI.B.

de Groot *et al.* (1997) considered the situation in which a photon with circular polarization (+ or − helicity) is incident on the sample with the angle φ from the sample surface normal, and the emitted photon is detected with the angle θ from the surface normal without analyzing the polarization, where the surface normal is perpendicular to the magnetization of the sample, and all the directions of incident and emitted photons, surface normal and the magnetization are in the same plane. Then they showed that the MCD of RIXS, i.e., the difference of RIXS for the incident photons with + and − helicities, is given by

$$\Delta F_{\mathrm{MCD}}(\Omega,\omega) = -\frac{1}{2}\sin\varphi[(1+\sin^2\theta)(F_{1-1}+F_{-1-1} - F_{11}-F_{-11}) + 2\cos^2\theta(F_{0-1}-F_{01})], \tag{43}$$

where $F_{q'q}$ is defined by

$$F_{q'q} = \sum_j \left| \sum_i \frac{\langle j|C^{(1)}_{q'}|i\rangle\langle i|C^{(1)}_{q}|g\rangle}{E_g+\Omega-E_i-i\Gamma_i} \right|^2 \times \frac{\Gamma_j/\pi}{(E_g+\omega-E_j)^2+\Gamma_j^2} \tag{44}$$

with the polar axis (for $C^{(1)}_q$) taken in the direction of the magnetization.

An example is shown in Fig. 34. Here, the experimental data (dots; Krisch *et al.*, 1996; de Groot *et al.*, 1997) are shown for the x-ray emission and its MCD for ferromagnetic Gd metal, where a $2p_{3/2}$ core electron is excited to the high-energy continuum and a $3d_{5/2}$ electron makes a radiative transition to the $2p_{3/2}$ state. The angles φ and θ are taken as 60 and 30°, respectively. The calculated results (de Groot *et al.*, 1997) with a Gd^{3+} ion model are also shown with the solid curves. The agreement with the experimental results is good. As found from Eq. (43), the spectral shape of the magnetic circular dichroism does not change with the change of φ (only with the change of MCD amplitude), but it depends on the angle θ. An example of the θ dependence was calculated by de Groot *et al.* (1997) for Gd. Experiments and calculations similar to Fig. 34 but for the $4d$ core level (instead of the $3d$ level) were also made by Krisch *et al.* (1996) and by de Groot *et al.* (1997). Similar NXES calculations were made by Jo and Tanaka (1998) both for $3d$ and $4d$ core levels of Nd^{3+}, Gd^{3+}, and Dy^{3+} ions.

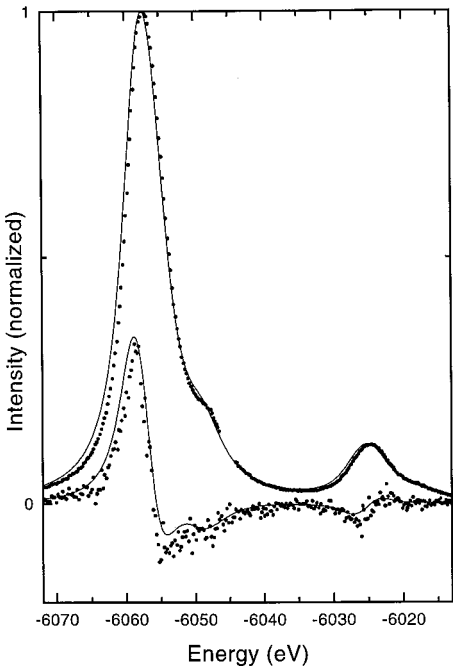

FIG. 34. Gd $4f\rightarrow 3d$ x-ray emission spectrum (upper curve) and its magnetic circular dichroism (lower curve) under the excitation of a $3d$ core electron to the high-energy continuum by circular polarized incident x rays. Solid curves and dots represent theoretical and experimental results, respectively. From de Groot *et al.*, 1997.

In deriving Eq. (43), an approximation has been made, in which some interference terms are disregarded for simplicity. The interference terms are negligibly small in the calculation shown in Fig. 34 (where $\varphi=60°$), but in the case of normal incidence ($\varphi=0°$) and a nonzero takeoff angle θ they can give a finite contribution to the magnetic circular dichroism. This is in contrast to the situation in XAS, where the MCD as well as $\Delta F_{\mathrm{MCD}}(\Omega,\omega)$ of Eq. (43) vanishes for $\varphi=0°$. Very recently, Braicovich *et al.* (1999) succeeded in measuring such MCD spectra (for $\varphi=0°$) for the Ni $3s\rightarrow 2p$ RIXS of $NiFe_2O_4$ and the Co $3s\rightarrow 2p$ RIXS of Co metal under the $2p\rightarrow 3d$ excitation. The physical mechanism of this phenomenon is explained by two antagonistic effects: One is that the spin-orbit interaction prefers the core-hole orbital moment in the intermediate state to align along the magnetization (spin) direction, and the other is that the selection rules for optical excitation result in a preferred alignment of the orbital moment parallel to the helicity vector of the circularly polarized light. As a result, the core-hole orbital moment direction is asymmetric with respect to the emitted-photon direction for the + and − helicities of the incident photon, and we have a finite magnetic circular dichroism in the RIXS.

As mentioned in the preceding subsection, Krisch *et al.* (1996) and Iwazumi *et al.* (1997) observed the MCD of Gd $3d_{5/2}\rightarrow 2p_{3/2}$ RIXS in the $2p_{3/2}$ excitation threshold. Compared with the MCD of NXES in Fig. 34, RIXS has similar global features, but some fine struc-

tures change with the incident-photon energy. The calculation of the MCD for RIXS is more difficult than for normal emission in which the electron excited to the continuum can be treated as free, and detailed theoretical calculations are left for future investigations. It is well known that the MCD of XAS and its sum rules (Thole *et al.*, 1992; Carra *et al.*, 1993) are very useful in the study of orbital and spin magnetism of the ground state, but the information given by MCD on inelastic scattering has not been well understood. RIXS can provide us with information on both the ground state and the intermediate state, hence giving much more information than XAS. How to derive effectively information on magnetic properties from the MCD of RIXS remains an open problem.

It should be mentioned here that van Veenendaal *et al.* (1996) discussed whether the sum rules of MCD in XAS could be applied to the MCD of the total fluorescence yield of RIXS. As we have discussed before, fluorescence yield does not necessarily coincide with x-ray absorption, but they showed that the integrated MCD intensity of fluorescence yield is useful, through the sum rules, for obtaining ground-state expectation values of L_z and S_z in the situation where no intermediate states with high LS purity are reached. Since fluorescence yield has the advantage over electron yield (which is often used in MCD observations) that it is less surface sensitive and free from magnetic-field problems, we expect that fluorescence yield will become more and more useful in MCD analysis of ferromagnetic systems.

V. TRANSITION-METAL COMPOUNDS

In general the $3d$ wave function of transition-metal compounds is more localized than s and p wave functions of semiconductors, but more extended than the $4f$ wave function of rare-earth systems. Therefore the electron correlation effect in RIXS of transition-metal compounds is intermediate between that of semiconductors, discussed in Sec. III, and that of rare-earth systems, discussed in Sec. IV. It is most interesting to study the interplay between the intra-atomic Coulomb interaction and interatomic hopping motion of $3d$ electrons in the RIXS of transition-metal compounds. Theoretical calculations of RIXS in transition-metal compounds have so far been made mainly with the Anderson impurity model (or small-cluster model), but it is desirable to go beyond the impurity model.

A. Crystal-field level excitation and charge-transfer excitation in copper oxide systems

In order to calculate the RIXS of transition-metal compounds, we have to take into account the anisotropy of the hybridization between the transition-metal $3d$ state and the ligand state. For instance, we consider the RIXS for Cu in the transition channel $2p \rightarrow 3d \rightarrow 2p$ in La_2CuO_4, a high-T_c cuprate. The local symmetry around the Cu ion in La_2CuO_4 is D_{4h}, and the hybridization strength $V(\Gamma)$ depends on the irreducible representation $\Gamma = b_{1g}$, a_{1g}, e_g, and b_{2g}. The ground state is a strongly mixed state (bonding state) between $3d^9(\Gamma)$ and $3d^{10}\underline{L}$ (Γ) configurations with $\Gamma = b_{1g}$ (we take the coordinate axes so that the z axis is perpendicular to the CuO_2 plane and the b_{1g} orbit is represented by $d_{x^2-y^2}$), and the weight of the $3d^9(b_{1g})$ configuration is about 60% (see, for instance, Kotani and Okada, 1990). Above the ground state there are bonding states with other irreducible representations (denoted by crystal-field levels) and nonbonding and antibonding states (denoted by charge-transfer states). The energy-level scheme is shown in Fig. 35(a). The intermediate state of the present RIXS (which is the same as the final state of Cu $2p$ x-ray absorption) is in the single configuration of $2p^5 3d^{10}$, and the incident-photon energy is tuned to the energy of this intermediate-state excitation. If the $2p^5 3d^{10}$ intermediate state decays to the ground state, we have an elastic x-ray scattering peak, while if it decays to some excited states above the ground state we have inelastic x-ray scattering structures.

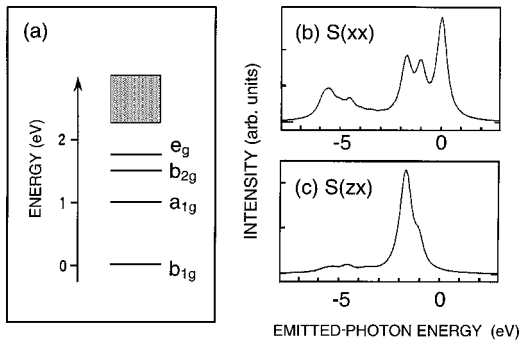

FIG. 35. (a) Energy-level diagram of crystal-field levels and charge-transfer continuum in La_2CuO_4, (b) calculated RIXS spectra for Cu $2p_{3/2} \rightarrow 3d \rightarrow 2p_{3/2}$ in La_2CuO_4 with the incident- and emitted-photon polarizations in the x direction, and (c) the same as (b) but with the incident- and emitted- photon polarizations in the x and z directions, respectively. From Kotani, 1998.

A theoretical calculation of the Cu $2p_{3/2} \rightarrow 3d \rightarrow 2p_{3/2}$ RIXS for La_2CuO_4 was made with the Anderson impuring model by Tanaka and Kotani (1993). Their results are shown in Figs. 35(b) and (c). Here, the polarization dependence of the resonant emission is studied, and the RIXS spectra S_{xx} and S_{zx} are shown to exhibit different features, when the incident-photon polarization is taken in the x direction, perpendicular to the crystalline c axis ($\| z$), and that of the emitted photon is in the x (for S_{xx}) and z (for S_{zx}) directions. In these figures, the origin of the emitted-photon energy is at the threshold for elastic scattering, and it can be seen that the inelastic scattering spectrum exhibits strong crystal-field level excitations for $0 < \Delta\omega < 2.0$ eV, where $\Delta\omega$ is the energy loss (Raman shift), while for $\Delta\omega > 2.0$ eV it shows weak and broad RIXS features due to the charge-transfer excitation. From this calculation, Tanaka and Kotani showed that the polarization dependence of the inelastic scattering provides us with important information on the symmetry of electronic states. However, a direct experimen-

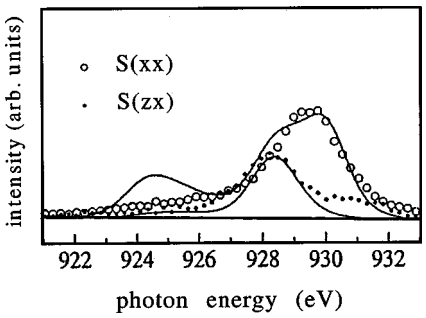

FIG. 36. Experimental data on polarization dependence in RIXS of La_2CuO_4. The open and closed circles are S_{xx} and S_{zx}, respectively. Calculated results are also shown with the solid curves, which are broadened versions of Figs. 34(b) and (c). From Duda, 1996.

tal measurement of the polarization dependence of RIXS is very difficult because of the problem of detecting the polarization of the emitted photon.

A few years after the theoretical calculation, the RIXS of La_2CuO_4, including its polarization dependence, was observed experimentally by using a sophisticated geometrical arrangement in which a spectrometer could be rotated around the incident beam axis and a sample could also be rotated around its surface normal (Duda, 1996; Duda, Stagarescu, *et al.*, 1998). The result (Duda, 1996) is shown in Fig. 36, where the open circles and dots are the experimental data corresponding to S_{xx} and S_{zx}, respectively. Unfortunately, the resolution is not very good. In order to compare the data with the theoretical results, S_{xx} and S_{zx} in Figs. 35(b) and (c) are broadened and plotted in Fig. 36 with solid curves. The experimental and theoretical results are in fair agreement, although the intensity of the charge-transfer excitation is weaker in the experimental data. If the experimental resolution is improved, polarization-dependent RIXS will become a powerful tool in the study of electronic-state symmetry in various materials in future.

The polarization dependence of RIXS has also been measured by Kuiper *et al.* (1998) for the Cu $3p \rightarrow 3d \rightarrow 3p$ transition in $Sr_2CuO_2Cl_2$. They observed RIXS by changing the angle between the x-ray emission direction and the sample normal (z axis), while keeping scattering angle to 90° and the polarization direction of the incident photon always in the xy plane. Then, the relative intensity of various crystal-field level excitations change with the angle, which made it possible for them to estimate the crystal-field excitation energies. For instance, the $e_g(d_{yz},d_{xz})$ to $b_{2g}(d_{xy})$ intensity ratio in RIXS increases when the angle changes from nearly grazing emission to nearly vertical emission. Kuiper *et al.* estimated that the transition from the $b_{1g}(d_{x^2-y^2})$ ground state to the b_{2g} state occurs at 1.35 eV and that to the e_g state at 1.7 eV. They also made some calculations to compare with the experimental data and obtained the result that the $a_{1g}(d_{3z^2-r^2})$ orbital energy is at 1.5 eV and the a_{1g} transition is accompanied by a local spin-flip excitation (see also de Groot *et al.*, 1998).

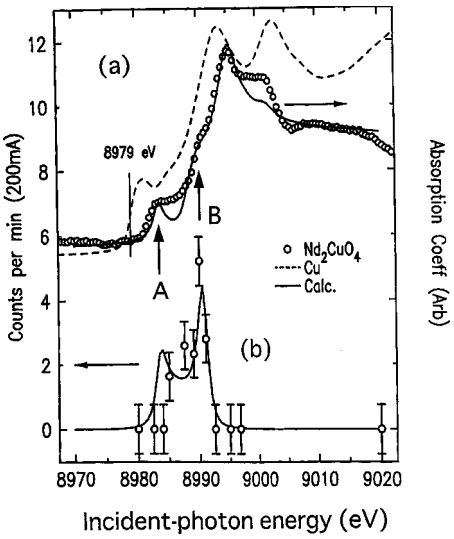

FIG. 37. Experimental data (open circles) and calculated results (solid curves) for (a) the Cu $1s$ x-ray absorption and (b) the intensity of the 6-eV feature of the Cu $1s \rightarrow 4p_\pi \rightarrow 1s$ RIXS in Nd_2CuO_4. Experimental absorption spectrum of the Cu $1s$ edge in Cu metal is also shown with the dashed curve. From Hill *et al.*, 1998.

Another interesting topic on divalent Cu oxides is the Cu $4p \rightarrow 1s$ emission in response to the Cu $1s \rightarrow 4p$ resonant excitation in Nd_2CuO_4. Hill *et al.* (1998) measured the Cu $1s \rightarrow 4p_\pi \rightarrow 1s$ RIXS, where a Cu $1s$ electron is excited to the Cu $4p_\pi$ conduction band by an incident photon with nearly z polarization, and then the Cu $4p_\pi$ electron makes a radiative transition to the $1s$ level. The local electronic structure around the Cu ion in Nd_2CuO_4 is almost the same as that in La_2CuO_4. The intermediate state of the present RIXS consists of two configurations: $1s^1 3d^{10}\underline{L} 4p_\pi$ (main peak of the Cu $1s$ absorption spectrum) and $1s^1 3d^9 4p_\pi$ (satellite), where the former is about 7 eV lower in energy than the latter. The experimental absorption spectrum (open circles) of the Cu $1s \rightarrow 4p$ excitation is shown in Fig. 37(a), where the spectral features A and B correspond to $1s^1 3d^{10}\underline{L} 4p_\pi$ and $1s^1 3d^9 4p_\pi$ configurations. According to these experiments, the inelastic-scattering spectra show a broad peak at about 6 eV from the elastic-scattering energy as shown in Fig. 38. The intensity of the 6-eV peak is strongly enhanced at the absorption feature B but displays almost no resonance at A. The observed intensity of the 6-eV peak is shown as a function of the incident-photon energy with the open circles in Fig. 37(b).

Theoretical analysis of this RIXS data has been made with the Anderson impurity model, and the 6-eV excitation assigned to the charge-transfer excitation [more exactly, the transition from the ground state to the antibonding state between $3d^9(b_{1g})$ and $3d^{10}\underline{L}(b_{1g})$ configurations]. The calculated result is shown with the solid curve in Fig. 37(b). Within the Anderson impurity model, however, resonance enhancement occurs for both the main peak and the satellite. As a possible reason for the suppression of the resonance at the main peak, the effect of nonlocal screening in the intermedi-

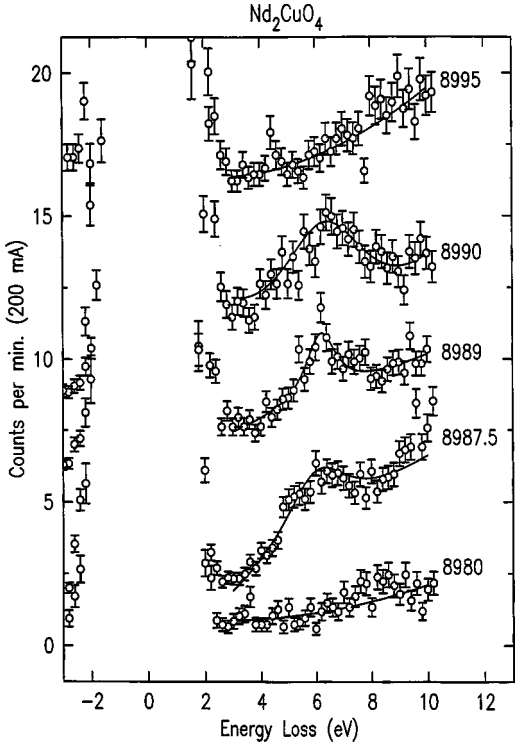

FIG. 38. Experimental RIXS data for the Cu $1s \rightarrow 4p_\pi \rightarrow 1s$ transition in Nd_2CuO_4 shown as a function of energy loss. Data are offset vertically for clarity and the solid curves are guides to the eye. From Hill *et al.*, 1998.

ate state was proposed. This will be discussed later in this section.

It should be mentioned that a similar measurement of $1s \rightarrow 4p \rightarrow 1s$ scattering has been made for NiO by Kao *et al.* (1996). The observed RIXS spectra were more complicated than those of Nd_2CuO_4, and two peaks were found at 4.9 and 7.8 eV, the relative intensity of which change with incident-photon energy. These peaks were considered to originate from charge-transfer excitations, but no detailed theoretical analysis was made.

B. Multiplet coupling effect and spin-dependent excitation spectra in Mn compounds

In the case of high-spin Mn^{2+} compounds, the Mn $3d$ shell is filled by five parallel-spin electrons to form a stable state, so that the hybridization effect between the $3d$ and ligand states is not very important. Therefore the so-called crystal-field model, in which only the effects of intra-atomic multiplet coupling and the electrostatic crystal field are taken into account (disregarding the hybridization effect), can describe the electronic states fairly well (see, for instance, de Groot, 1994). In Fig. 39, we show experimental results for the Mn $2p$ x-ray absorption (upper panel) and the Mn $2p \rightarrow 3d \rightarrow 2p$ RIXS (dots) of MnO, as well as the calculated RIXS results (solid curve) with the crystal-field model (Butorin, Guo, *et al.*, 1996). The RIXS structures within 7 eV from the elastic scattering peak (the origin of the abscissa) are reproduced fairly well by the calculation, and these

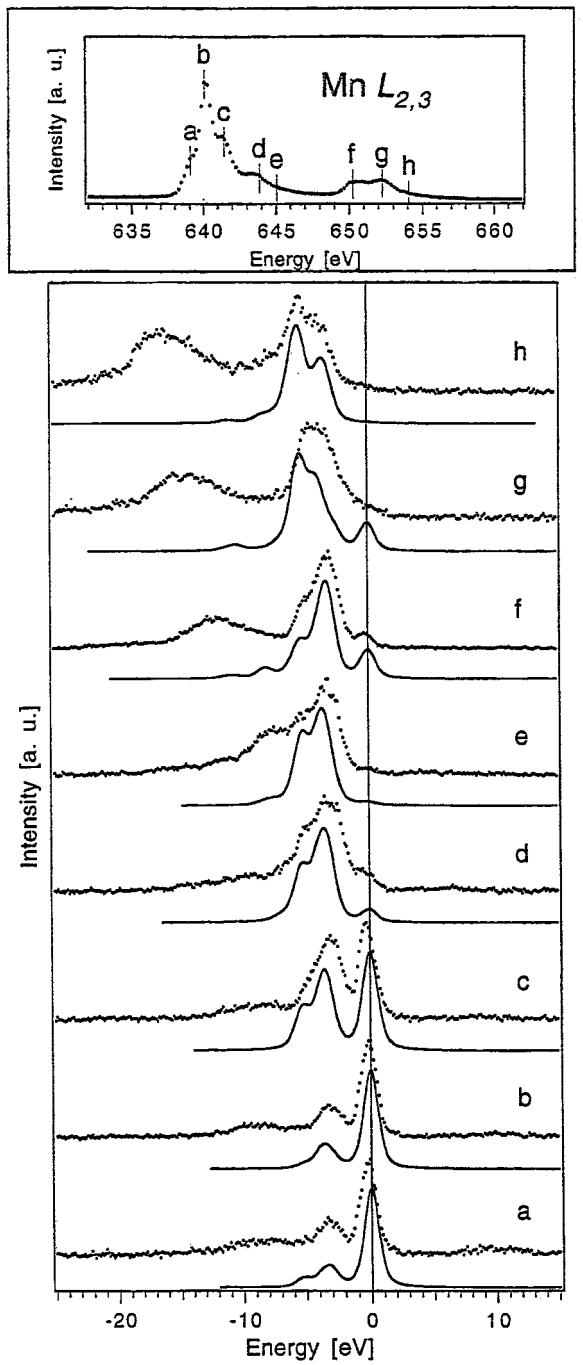

FIG. 39. Experimental results (dots) for the Mn $2p \rightarrow 3d \rightarrow 2p$ RIXS of MnO compared with calculated ones (solid curves) with the crystal-field model. The incident-photon energies a–h are taken at the positions shown in the Mn $2p$ absorption spectrum in the uppermost panel. From Butorin, Guo, *et al.*, 1996.

structures originate from the atomic multiplet term excitations modified by the crystal field (the so-called d-d excitation). According to the calculation, taking into account the hybridization effect, a charge-transfer satellite is found around 10 eV from the elastic scattering peak, but its intensity is small (Taguchi, 1998).

It should be mentioned that, for Mn^{3+} (as well as $Mn^{3.5+}$) compounds, the effect of interatomic hybridiza-

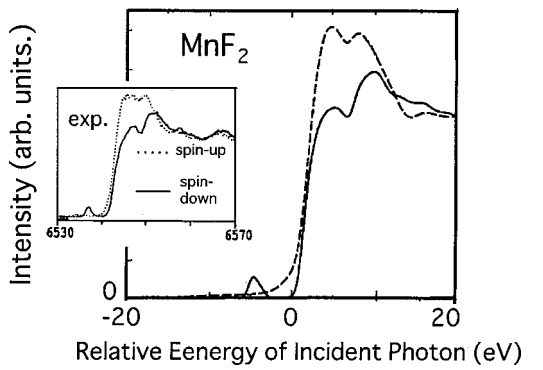

FIG. 40. Calculated spin-dependent excitation spectra for MnF_2, compared with experimental ones in the inset. From Taguchi, 1998.

tion is much more important. Kurmaev *et al.* (1999) measured the Mn $2p \rightarrow 3d \rightarrow 2p$ RIXS and the O $1s \rightarrow 2p \rightarrow 1s$ RIXS in $Pr_{0.5}Sr_{0.5}MnO_3$. From these data (as well as x-ray photoemission) and LSDA band-structure calculations, they concluded that the valence electronic structure of this compound consists mainly of Mn $3d$ and O $2p$ states which are hybridized over the whole valence band.

Spin-dependent excitation spectra in Mn compounds offer another interesting example of RIXS. Let us consider the situation in which a Mn $1s$ electron in MnF_2 is excited to a Mn $4p$ conduction band by the incident x ray, and then a Mn $3p$ electron makes a transition to the $1s$ state by emitting an x-ray photon. If we consider the case in which the excited Mn $1s$ electron has a down-spin (here the down-spin means that the spin direction is antiparallel to the $3d$ spin direction in the same atomic site), then the net spin of the $3p$ state in the final state is parallel to the $3d$ spin, and the RIXS spectrum (not shown here) exhibits a high-energy main peak ^7P because of the gain in the $3p$-$3d$ exchange interaction. On the other hand, if the excited Mn $1s$ electron has an up-spin, then the net Mn $3p$ spin is antiparallel to the $3d$ spin and we have a low-energy satellite with ^5P in the inelastic scattering spectrum. Therefore, if one fixes the emitted-photon energy at the main peak and measure the change in the inelastic scattering intensity by changing the incident-photon energy near the threshold of the Mn $1s$ absorption spectrum, then the excited Mn $1s$ electron has necessarily a down-spin, and the observed excitation spectrum is expected to reflect the partial density of states of the conduction band with down-spin. Conversely, if one fixes the emitted-photon energy at the satellite, the excited Mn $1s$ electron will have an up-spin and the observed spectrum should reflect the partial DOS of a conduction hand with up-spin.

Such experiments have been carried out by Hämäläinen *et al.* (1992) for MnF_2 and MnO, and the results for MnF_2 are shown in the inset of Fig. 40. The spin-down and spin-up curves correspond to the excitation spectra at the main peak and the satellite, respectively. These spectra were found not to agree well with the spin-dependent density of states of the Mn $4p$ conduction band of MnF_2, calculated by the spin-dependent linearized augmented plane-wave method (Dufek *et al.*, 1992). In order to explain the mechanism of these spin-dependent excitation spectra, Taguchi *et al.* (1997) calculated the excitation spectra with a MnF_6 cluster model (local ligand-state version of the Anderson impurity model) using the second-order optical formula, in which a model of the spin-dependent Mn $4p$ density of states was taken from energy-band calculations. In the calculation of the excitation spectra, they took into account the following effects: (i) core-hole potential acting on the conduction-band states, (ii) term-dependent lifetime broadening of the Mn $3p$ core hole, (iii) spin-flip effect by the $3d$-$3d$ exchange interaction, and (iv) covalency hybridization between Mn $3d$ and F $2p$ states. They obtained the excitation spectra shown in Fig. 40, which are in good agreement with the experimental data. From this analysis, it is concluded that the effects of the core-hole potential and term-dependent lifetime broadening are very important in explaining the difference between the excitation spectra and the density of states.

After the measurements by Hämäläinen *et al.* (1992), similar spin-dependent excitation spectra were observed for Fe compounds (Peng *et al.*, 1994; Wang *et al.*, 1995) and Ni compounds (de Groot, Fontaine, *et al.*, 1994; Wang *et al.*, 1997). In some of these studies, measurements of spin-dependent excitation spectra for $2p \rightarrow 1s$ inelastic scattering (instead of $3p \rightarrow 1s$ inelastic scattering) were also reported. In the case of $2p \rightarrow 1s$, the spin dependence comes mainly from the spin-orbit interaction of the $2p$ state, whereas it comes mainly from the $3p$-$3d$ exchange interaction in the $3p \rightarrow 1s$ transition, as mentioned before. As another example of exchange splitting in RIXS, Braicovich *et al.* (1997) measured the Ni $3s \rightarrow 2p$ RIXS of NiO at the Ni $2p \rightarrow 3d$ excitation threshold. In this case the $3s$-$3d$ exchange interaction plays an essential role in the final state, instead of the $3p$-$3d$ exchange interaction.

In Fig. 40 a weak pre-edge peak is found below the absorption threshold of the spin-down spectrum, but no pre-edge peak for the spin-up spectrum. This pre-edge peak originates from the Mn $1s$-$3d$ quadrupole excitation. For Mn^{2+} the $3d$ majority spin states are completely filled, so that the quadrupole transition is forbidden for the spin-up spectrum. Recently, Mn $3p$-$1s$ scattering in MnF_2 has been measured by tuning the incident-photon energy to the pre-edge peak excitation, and the results have been analyzed theoretically with the cluster model by Taguchi *et al.* (2000). The results are shown in Fig. 41. The structures A and B of the pre-edge peak of XAS experiments, which are shown in the inset of Fig. 41, correspond to crystal-field splitting of the Mn $3d$ state, and the experimental Mn $3p$-$1s$ RIXS spectra with the incident-photon energy tuned to A and B are shown with the dotted curves A and B, respectively, in Fig. 41. The dotted curve of the normal x-ray emission is observed for the incident-photon energy well above the absorption edge. The solid curves in Fig. 41 are the calculated results, and we find a good agreement between the theoretical and experimental results. The RIXS due to the $1s$-$3d$ pre-edge-peak excitation was also mea-

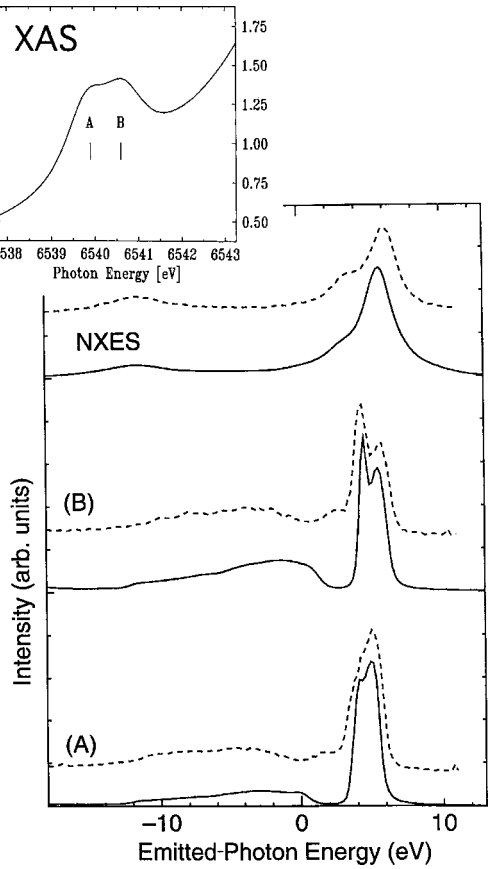

FIG. 41. Experimental data on a pre-edge peak of the Mn 1*s* absorption spectrum (inset) and Mn 3*p*-1*s* RIXS (dashed line) in MnF_2. The calculated RIXS results are shown with the solid curves. (A) and (B) of RIXS correspond to the incident photon energies A and B in XAS, respectively, while NXES is obtained for the incident photon energy well above the absorption threshold. From Taguchi *et al.*, 2000.

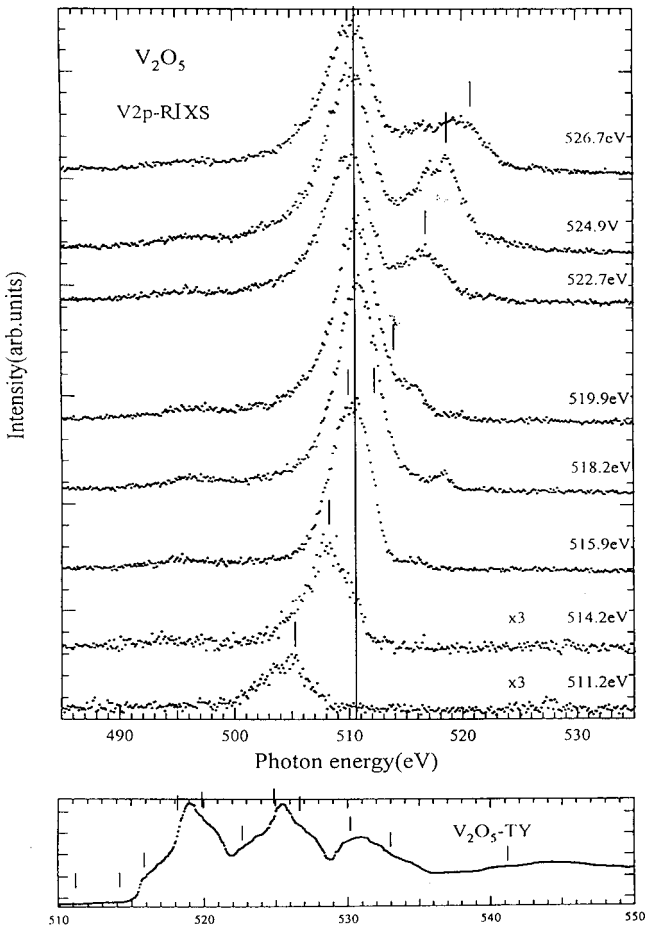

FIG. 42. Experimental data on the V 2*p* RIXS in V_2O_5. The lower panel shows the total electron yield (TY) spectrum. The vertical bars in the lower panel correspond to the photon energies where the RIXS spectra were measured. From Shin *et al.*, 1998.

sured by Caliebe *et al.* (1998) for the Fe $2p \rightarrow 1s$ transition in α-Fe_2O_3. Those authors also made a theoretical analysis of the RIXS data.

Although the quadrupole transition is much weaker than the dipole transition, RIXS with a quadrupole excitation (or quadrupole deexcitation) is becoming an interesting research subject with third-generation synchrotron radiation.

C. Early transition-metal compounds and the effect of carrier doping

It is known that the late transition-metal compounds belong to charge-transfer-type systems, where the charge-transfer energy Δ is smaller than the Coulomb interaction energy U_{dd}. On the other hand, early transition-metal compounds belong to Mott-Hubbard-type systems, where U_{dd} is smaller than Δ. Furthermore, as a general trend, the hybridization strength between the 3*d* and ligand states increases with decreasing atomic number, so that the 3*d* state in early transition-metal compounds is more itinerant than that in late transition-metal compounds. Recently, experimental studies of RIXS have been carried out for several early transition-metal compounds, such as TiO_2, VO_2, $FeTiO_3$, and $SrVO_3$, and it is interesting to study whether the band model or the Anderson impurity model (local model) can better explain the RIXS data of early transition-metal compounds.

As typical cases of early transition-metal compounds, let us consider nominally d^0 compounds. RIXS of nominally d^0 compounds, $SrTiO_3$, $BaTiO_3$ (Jiménez-Mier *et al.*, 1999), TiO_2 (Tezuka *et al.*, 1996; Jiménez-Mier *et al.*, 1999), Sc compounds, V_2O_5 (Shin *et al.*, 1998), and $KMnO_4$ (Butorin, Guo, Magnuson, and Nordgren, 1997) have been measured so far. Figure 42 shows an example of RIXS in V_2O_5. A peak is observed at around 6.2 eV from the elastic scattering line, as indicated by vertical bars. This peak can be explained by the charge transfer excitation. If we use the Anderson impurity model, the character of the charge-transfer excitation in the d^0 systems is very similar to that of the f^0 systems, such as CeO_2, although the value of the charge-transfer excitation energy and the relative intensity between inelastic and elastic scattering peaks are different for d^0 and f^0 systems. On the other hand, a prominent inelastic scat-

tering peak appears at about $\omega = 510.5$ eV for the incident-photon energy Ω larger than 515.9 eV (threshold of V $2p$ x-ray absorption). The peak energy is close to that of NXES, which is obtained for Ω well above the threshold, but the peak energy, as well as the spectral shape, changes slightly (but significantly) with the change of Ω in the threshold region. Therefore we denote this peak as the "NXES-like" peak, to discriminate from the true NXES peak. This NXES-like peak is absent from the RIXS of CeO_2 (see Fig. 17), and it cannot be explained by the Anderson impurity model.

Recently Jiménez-Mier *et al.* (1999) measured the RIXS of the nominally d^0 systems $BaTiO_3$ and TiO_2 and analyzed the spectra based on the energy-band model. The resonant inelastic scattering in these d^0 systems is qualitatively the same as that in V_2O_5. The observed total electron yield (TY) and RIXS spectra for TiO_2 are shown in Figs. 43(a) and (b), respectively, where the RIXS spectrum is displayed as a function of the emitted-photon energy. A peak is observed at 7.8 eV from the elastic scattering line (indicated by E) and a prominent NXES-like peak (indicated by 3) at $\omega \sim 451$ eV.

In order to analyze the RIXS spectra, Jiménez-Mier *et al.* made the energy-band calculation with the LMTO method and within the local-density approximation for $E_{xc}[n(\mathbf{r})]$ in Eq. (10). Then they calculated the RIXS spectra using Eq. (13). In this case, the quantities ρ and ρ' in Eq. (13) are the d-symmetric partial densities of states of the valence and conduction bands, respectively. They published the calculated results only for Ω near the absorption threshold; these are displayed in Fig. 44(b) in comparison with the corresponding experimental data [Fig. 44(a)]. The calculated results are in good agreement with the experimental ones below the threshold (for $\Omega < 459$ eV). The main inelastic scattering peak (indicated by 3) originates from the excitation of a valence electron to the conduction band, which is a band-model version of the charge-transfer excitation in the Anderson impurity model. However, if we look carefully at the result for $\Omega = 461.1$ eV, we find a difference between the calculated and experimental spectra. The calculated peak 3 is still an inelastic scattering peak, which shifts parallel with the elastic scattering peak, but the experimentally observed peak 3 is not a simple inelastic scattering peak but the NXES-like peak, and the inelastic peak corresponding to the calculated one is seen as a shoulder on the higher-energy side of peak 3. If the incident-photon energy is increased further, the inelastic scattering peak and the NXES-like peak should form two prominent peaks as found in Fig. 43(b).

It is to be remarked that Jiménez-Mier *et al.* disregarded the core-hole effect (in the intermediate state), which is much more important in this case than in graphite (see Sec. III.C) because the Ti $3d$ state is more localized than the C $2p$ state. If the core-hole potential U_{dc} is included in the calculation, the Coulomb interaction U_{dd} between $3d$ electrons should also be taken into account (otherwise, the core-hole potential is overscreened by the $3d$ electrons). Probably, the independent-particle approximation breaks down in describing the core level spectra including RIXS in transition-metal compounds even for the nominally d^0 systems. In this connection, it should be mentioned that the Anderson impurity model (or small-cluster model) can well describe $2p$ photoemission and $2p$ absorption of nominally d^0 systems (Okada and Kotani, 1993; de Groot, 1994), but there has been no report (to the authors' knowledge) that these spectra are well reproduced by the energy-band model. Nevertheless, the Anderson impurity model also fails in describing the NXES-like spectra, as mentioned before.

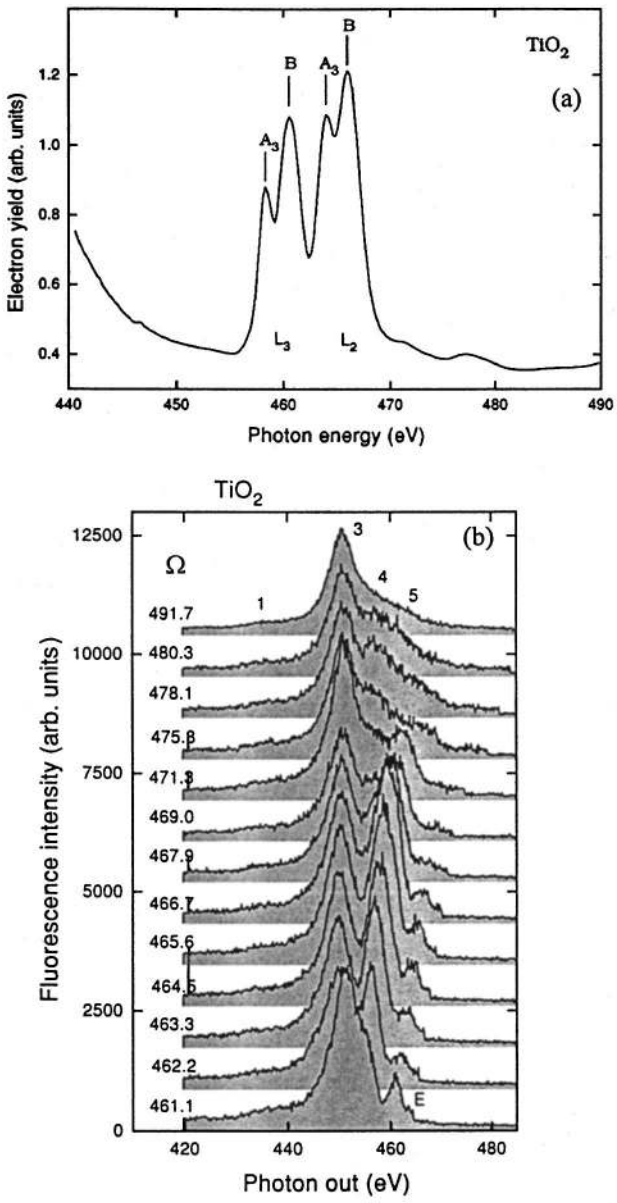

FIG. 43. Experimental data on (a) Ti $2p$ total electron yield and (b) Ti $2p$ RIXS in TiO_2. From Jiménez-Mier *et al.*, 1999.

More recently, Finkelstein *et al.* (1999) have made similar calculations of RIXS in TiO_2 but with a restricted joint density-of-states model, taking into account the effect of momentum conservation. However, their results did not reproduce the coexistence of the two prominent peaks, the inelastic scattering and NXES-like peaks, in

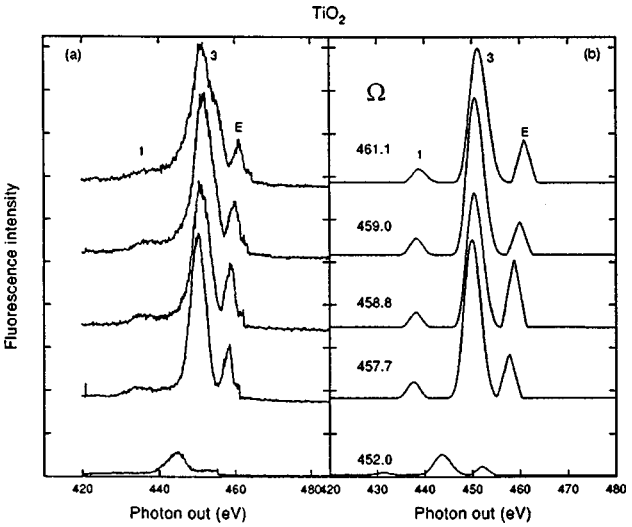

FIG. 44. Comparison of (a) experimental data and (b) calculated RIXS for the Ti $2p \rightarrow 3d \rightarrow 2p$ transition for incident-photon energies at and below the threshold. From Jiménez-Mier *et al.*, 1999.

the experimental data. In the next subsection some attention will be devoted to an approach that goes beyond the band model and Anderson impurity model.

In Fig. 43(a), the four main peaks of the Ti $2p$ XAS in TiO_2 are due to the spin-orbit splitting of the $2p$ level (L_2 and L_3) and the crystal-field splitting of the $3d$ state (A and B), but we can see weak satellite peaks about 13 eV from the main peak. According to the cluster-model calculation, these satellites are interpreted as the excitation of the antibonding state between $3d^0$ and $3d^1\underline{L}$ configurations (i.e., the charge-transfer excitation), similarly to the satellites in CeO_2. However, another interpretation has also been proposed by van der Laan (1990), namely, that these satellites originate from a "polaronic" effect. The polarization dependence of the RIXS will give important information on the mechanism of the satellite. The situation is essentially the same as that for the nominally f^0 systems such as CeO_2 (see Sec. IV.E). The results in Fig. 43(b) were observed with the depolarized configuration. From the analogy with the RIXS of CeO_2 (except for the existence of an NXES-like peak), we expect that if the cluster model calculation is applicable, a strong RIXS peak corresponding to excitation of the antibonding state occurs when the incident-photon energy is tuned to the satellite position of the x-ray absorption spectrum with the polarized configuration. The RIXS peak at 7.8 eV corresponds to excitation of the nonbonding state, and the peak corresponding to the antibonding state (which is absent from the depolarized configuration) is estimated to occur at about 14 eV with the cluster model (Matsubara *et al.*, 2000). An experimental observation of RIXS in TiO_2 has also been made very recently with both polarized and depolarized configurations (Harada *et al.*, 2000), and the result is just as expected here; it strongly supports the charge-transfer mechanism of the XAS satellite. As mentioned before in this subsection, the small-

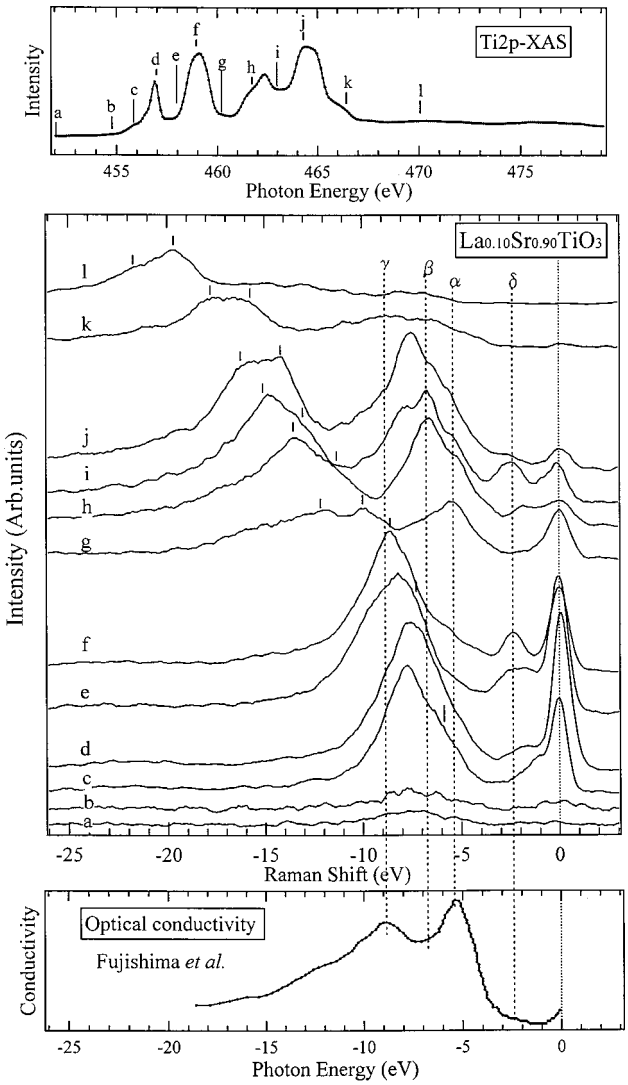

FIG. 45. Ti $2p$ RIXS spectra of $Sr_{0.90}La_{0.10}TiO_3$ excited at incident-photon energies **a**–**l**, which are indicated in the Ti $2p$ absorption spectrum in the top panel. For comparison, the optical conductivity spectrum is also shown in the bottom panel. From Higuchi *et al.*, 1999.

cluster model fails in reproducing the NXES-like spectrum, which includes a spatially extended electronic state, but can describe quite well the charge-transfer excitation, which is rather localized, and also the charge-transfer satellite in the absorption spectrum.

Next we consider the more interesting but more complicated systems with carrier doping. $SrTiO_3$ is an insulator with nominally d^0 configuration, but when Sr is partially substituted for La the system becomes metallic with carriers doped in the $3d$ conduction band. The $3d$ band is split into t_{2g} and e_g subbands by the crystal-field effect, and the carriers are in the t_{2g} band. Figure 45 shows the RIXS spectra of metallic $La_{0.10}Sr_{0.90}TiO_3$ (Higuchi *et al.*, 1999), where the incident-photon energies are taken at **a**–**l** and shown in the top panel (total-yield spectrum) and the emitted-photon energy (abscissa) is measured with the elastic scattering energy peak as origin, i.e., the abscissa is the Raman shift. We

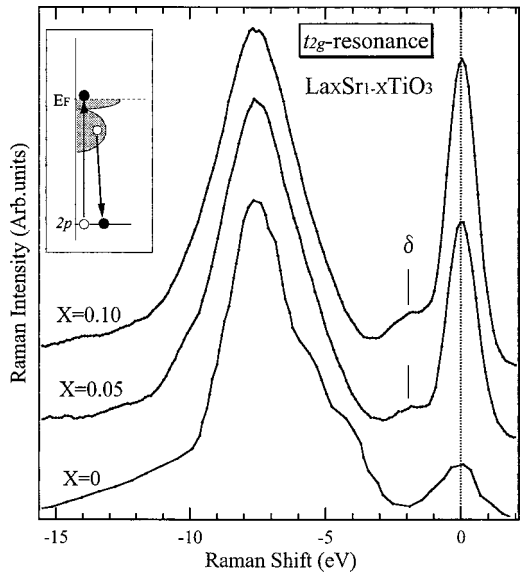

FIG. 46. Comparison of the Ti $2p$ RIXS spectra of $La_xSr_{1-x}TiO_3$ for $X=0, 0.05, 0.10$. From Higuchi *et al.*, 1999.

see strong NXES-like spectra, shown with vertical bars, where the emitted-photon energy is nearly constant, but at the same time some inelastic scattering peaks are shown with $\alpha \sim \delta$. It is interesting to compare the inelastic scattering spectra with the experimental data on optical conductivity (Fujishima *et al.*, 1993), which is shown in the bottom panel, because both of them represent the same elementary excitations in the final state, although the selection rule is different. The optical conductivity shows a Drude-type photoresponse below 1.5 eV due to the charge carriers and interband transitions above 3 eV. The interband transition at 5.2 eV corresponds to α in RIXS, and it is interpreted as the transition from the O $2p$ band to the Ti t_{2g} subband. The energy difference between α and β corresponds to that between the t_{2g} and e_g subbands, so that the β peak is interpreted as the transition from the O $2p$ to the Ti e_g subband, although the structure β is not seen clearly in the optical conductivity. The origin of the second peak (γ) in the optical conductivity is not clear, and the intensity of γ for RIXS is very small. The peak δ is seen only in RIXS, probably because it originates from a transition within the d states (locally forbidden in the optical conductivity). It will be shown below that the peak δ is sensitive to carrier doping. It should be mentioned that the Drude-type contribution can also be observed, in principle, as a quasielastic component in RIXS. However, the width of the elastic scattering peak is too large in the present experiment to separate the quasielastic and elastic scattering spectra. If the resolution is improved in future, it will be very interesting to study the Drude-type quasielastic scattering spectrum separately from the elastic scattering peak.

Figure 46 shows the doping dependence of the RIXS spectra for $La_xSr_{1-x}TiO_3$ ($x=0,0.05,0.10$), where the incident-photon energy is taken at **d** of Fig. 45 (Higuchi *et al.*, 1999). Comparing each spectrum, one can find that the intensity of the δ peak becomes stronger with an increase in La doping. One possible interpretation is that this peak comes from the t_{2g} to e_g excitation, i.e., the crystal-field level excitation, which is absent in nominally d^0 systems and becomes stronger with increasing t_{2g} electron occupation number. Another interpretation is that this originates from the correlation effect of the metallic carriers. According to the Fermi-liquid theory, the conduction-electron state near the Fermi level is renormalized by the electron correlation effect into a quasiparticle state (called the *coherent part*) with an appropriate mass renormalization. The spectral weight of the quasiparticle (with momentum $\mathbf{k}$) is reduced to $Z_{\mathbf{k}}$, where $Z_{\mathbf{k}}$ is the quasiparticle pole strength, and the remaining weight $1-Z_{\mathbf{k}}$ forms a broad high-energy spectrum, called the *incoherent part*. As shown in the inset of Fig. 46, the RIXS peak δ could be interpreted as the excitation of a coherent-electron/incoherent-hole pair in the Ti t_{2g} conduction band. The doping effect is an interesting problem for more detailed study in the near future. A theoretical study of RIXS with the Hubbard model has recently been made by Okada and Kotani (2000), including the effects of carrier doping.

D. Limitations of the band model and the Anderson impurity model

As mentioned in Sec. II.C, the energy-band model is more appropriate for the calculation of ground-state properties than for the excitation spectra, and is more appropriate to describe systems with weak correlation than those with strong correlation. In the analysis of core-level spectroscopy, the band model has been applied successfully to semiconductors and ionic insulators, but not very successfully to f and d electron systems. Especially in the final state of core level spectra of rare-earth compounds and transition-metal compounds, the f and d electron states are more localized by the effect of the attractive core-hole potential (if the core hole is on the rare-earth or transition-metal site), and then the intra-atomic electron correlation and the multiplet coupling effect, which cannot be described well by the band model, become more important. Even in the early transition-metal compounds, such as CaF_2 and TiO_2, where the $3d$ wave function is expected to be more extended than in other transition-metal compounds, x-ray absorption and photoemission are known to be described well by the cluster model or Anderson impurity model (Okada and Kotani, 1993; de Groot, 1994) but the band model seems to break down.

Let us discuss the applicability of the local model (cluster model or Anderson impurity model) to RIXS in f and d electron systems. The spatial extension of the transition-metal $3d$ wave function is larger than that of the rare-earth $4f$ wave function. Therefore it is expected that the RIXS of transition-metal compounds will be more sensitive to cluster size. We have shown that the RIXS of CeO_2 can be well analyzed with the Anderson impurity model, but the applicability of such a model to the analysis of RIXS in TiO_2 is questionable (note that CeO_2 and TiO_2 are nominally $4f^0$ and $3d^0$ systems, re-

spectively, with some similarity in their electronic structure). As discussed in the preceding subsection, neither the Anderson impurity model nor the band model can reproduce well the experimental results of the Ti $2p \rightarrow 3d \rightarrow 2p$ RIXS in TiO_2 (shown in Fig. 43) by Jiménez-Mier *et al.* (1999), especially for NXES-like spectra. Therefore it is interesting to study the effect of cluster size on the RIXS of CeO_2 and TiO_2.

It is also interesting to compare the cluster size dependence of RIXS with that of XAS. The cluster size dependence is expected to be different for the second-order optical process of RIXS and the first-order optical processes of photoemission and absorption, because RIXS is sensitive to the electron dynamics (which should depend on the cluster size) in the intermediate state. As is well known, the experimental results of XPS and XAS for both CeO_2 and TiO_2 can be quite well reproduced by the Anderson impurity model or small-cluster model.

In order to study these points, Idé and Kotani (1998) made a model calculation using the following one-dimensional (1D) d-p Hamiltonian as a model of TiO_2:

$$
\begin{aligned}
H=&\sum_{l,\sigma}\left[(\Delta+\varepsilon_p)\, d^{\dagger}_{l\sigma}d_{l\sigma}+\varepsilon_p\, p^{\dagger}_{l\sigma}p_{l\sigma}\right]\\
&+\sum_{\langle i,j\rangle}\sum_{\sigma}\left[v\, d^{\dagger}_{i\sigma}p_{j\sigma}+v^{*}p^{\dagger}_{j\sigma}d_{i\sigma}\right]\\
&-U_{dc}\sum_{l}\left(\sum_{\sigma} d^{\dagger}_{l\sigma}d_{l\sigma}\right)\left(\sum_{\sigma'} c_{l\sigma'}c^{\dagger}_{l\sigma'}\right)\\
&+U_{dd}\sum_{l} d^{\dagger}_{l\uparrow}d_{l\uparrow}d^{\dagger}_{l\downarrow}d_{l\downarrow}+\sum_{l,\sigma}\varepsilon_c\, c^{\dagger}_{l\sigma}c_{l\sigma}. \qquad (45)
\end{aligned}
$$

Here, $d^{\dagger}_{l\sigma}$ ($p^{\dagger}_{l\sigma}$) is a creation operator of a σ spin electron on the d (p) site in the lth unit cell, Δ is the charge-transfer energy between d and p orbitals, v is the nearest-neighbor d-p hopping, U_{dd} is the on-site d-d Coulomb interaction, and U_{dc} is the intra-atomic core-hole potential. $c^{\dagger}_{l\sigma}$ ($c_{l\sigma}$) is a creation or annihilation operator of the core electrons, and ε_c is the core electron energy. The effect of orbital degeneracy is disregarded, for simplicity.

The geometry of the system is shown at the top of Figs. 47 and 48. The d_1p_2 cluster with the *open boundary condition* (Fig. 47) is used as a reference system representing the smallest cluster with a single metal ion, and the effect of larger clusters is studied using the d_Np_N clusters with the *periodic boundary condition* (Fig. 48). The number of valence electrons in the ground state is taken as $2N$ for d_Mp_N system.

Although orbital degeneracy is not considered in this model, its effect on d-p hopping can partly be taken into account by putting $v=\sqrt{[2V(e_g)^2+3V(t_{2g})^2]}/2$, where $V(e_g)$ and $V(t_{2g})$ are hybridization strengths of e_g and t_{2g} states of the TiO_6 cluster model. Using the parameter values $V(e_g)=3.0$ and $V(t_{2g})=-1.5$ (in units of eV) after Okada and Kotani (1993), one obtains $v=3.5$ eV. Other parameters are chosen to be $\Delta=4.0$, $U_{dd}=4.0$, and $U_{dc}=6.0$ (in eV). These will be referred to as "TiO_2-like" parameters. The present model can also be used for the RIXS calculation of the Ce $3d \rightarrow 4f \rightarrow 3d$ transition in a "CeO_2-like" system by regarding d, p, and c as Ce $4f$, O $2p$, and Ce $3d$ orbitals, respectively, and by taking appropriate values for the model parameters.

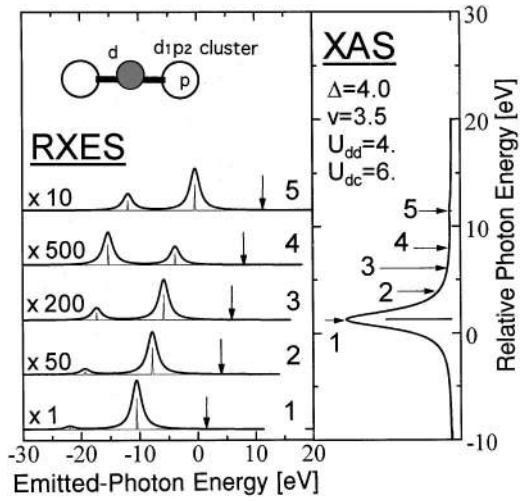

FIG. 47. Calculated x-ray absorption (XAS) and RIXS spectra (here termed RXES following the original reference) for TiO_2-like parameters in a d_1p_2 cluster, the geometry of which is shown in the inset. From Idé and Kotani, 1998.

The RIXS spectrum is calculated using the coherent second-order optical formula [Eq. (5)]. The operator T of the optical dipole transition is now written as $T=\Sigma_{l,\sigma}(d^{\dagger}_{l\sigma}c_{l\sigma}+c^{\dagger}_{l\sigma}d_{l\sigma})$. It is essential to take the summation over all l sites in T in order to take into account the effect of wave-vector conservation in RIXS.

Figures 47 and 48 show the absorption and inelastic scattering spectra for the TiO_2-like parameters in d_1p_2 and d_6p_6 clusters, respectively. It can be seen that dependence of x-ray absorption on cluster size is small. With an increase in the cluster size, only a small amount of absorption fine structure appears on the high-energy

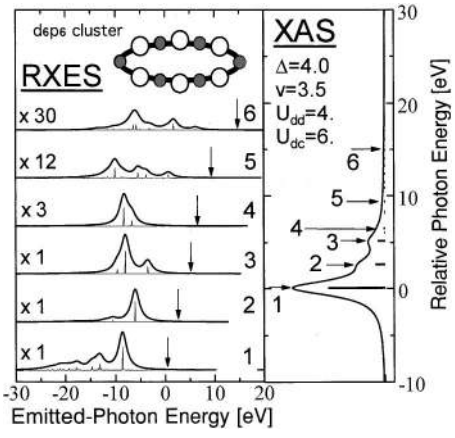

FIG. 48. Calculated spectra like those in the previous figure except using a d_6p_6 cluster, the geometry of which is shown in the inset. From Idé and Kotani, 1998.

tail of the main peak. This small modification of the absorption spectrum with cluster size, however, causes a very drastic change in RIXS, as shown in these figures. Here the calculated RIXS are shown with the incident-photon energy Ω tuned to the XAS energy positions 1, 2, 3, and so on. In this calculation, the main interest is confined to the study of inelastic scattering spectra, and for the elastic scattering component ($\omega=\Omega$) only the emitted-photon energy is shown with the arrow in the RIXS spectrum.

In the case of the d_1p_2 system, RIXS peaks are caused by the *local* charge-transfer excitation, and the emitted-photon energy ω moves in parallel with the incident-photon energy Ω. The first RIXS peak corresponds to a single-electron transfer excitation (to the antibonding state between d^0 and $d^1\underline{p}$ configurations), while the second one corresponds mainly to a two-electrons transfer excitation. For the d_6p_6 cluster, on the other hand, the energy ω of the strongest peak does not follow Ω but is rather constant; more precisely, it oscillates with the change of Ω. Thus the cluster size effect is very important for RIXS.

Similar calculations have been made for a CeO_2-like system (Idé and Kotani, 1998), although the result is not shown here. It was found that the cluster size dependence of XAS and RIXS for the CeO_2-like system was much smaller than that for the TiO_2-like system, and the small-cluster model worked well in describing both XAS and RIXS.

These results suggest that the Anderson impurity model well describes XAS for both TiO_2 and CeO_2 and justify previous theoretical analyses of Ti $2p$ absorption in TiO_2 and Ce $3d$ absorption in CeO_2. For RIXS, on the other hand, the cluster size dependence is very important for a TiO_2-like system, while the Anderson impurity model works fairly well for a CeO_2-like system. According to the Ti $2p\rightarrow 3d\rightarrow 2p$ RIXS spectra measured experimentally by Jiménez-Mier *et al.* (1999), strong NXES-like spectra whose energy ω did not follow the change of Ω were observed. These spectra were qualitatively consistent with the results of the d_6p_6 cluster. The theory by Idé and Kotani has also been extended to the system with orbital degeneracy (Idé and Kotani, 2000a).

Another example in which a model beyond the small-cluster model plays an important role is the Cu $1s\rightarrow 4p_\pi\rightarrow 1s$ RIXS in Nd_2CuO_4. As mentioned in Sec. V.A, Hill *et al.* (1998) observed the resonant enhancement of the 6-eV intensity at the absorption feature B, whereas the calculation with the Anderson impurity model shows the resonance both at A and B. A possible reason for this discrepancy is the effect of nonlocal screening in the intermediate state. As first pointed out by van Veenendaal *et al.* (1993), nonlocal, solid-state, effects play an important role in the final state of Cu $2p$ photoemission in systems with a linear chain of CuO_4 plaquettes. These authors showed that while a $3d^{10}\underline{L}$ state was required to screen the $2p$ core hole, the lowest-energy state was one in which the $\underline{L}$ hole, repelled by the $2p$ hole, moved onto another CuO_4 plaquette. This effect was stabilized by the formation of a Zhang-Rice singlet state (Zhang and Rice, 1988) on the second plaquette. Recent calculations have extended such conclusions to 2D clusters (Okada and Kotani, 1997). The Cu $2p$ photoemission final state is thought of as analogous to the Cu $2p$-$4p_\pi$ resonant intermediate state, and hence the lowest edge of the Cu $2p$-$4p_\pi$ absorption spectrum corresponds to a state with a Zhang-Rice singlet on the second plaquette. However, the 6-eV final state is a state without the Zhang-Rice singlet (even in large-cluster systems), so that the transition probability from the lowest XAS edge to the 6-eV feature should be suppressed. This idea is supported by a model calculation of RIXS in a Cu_5O_{16} cluster by Idé and Kotani (1999, 2000b).

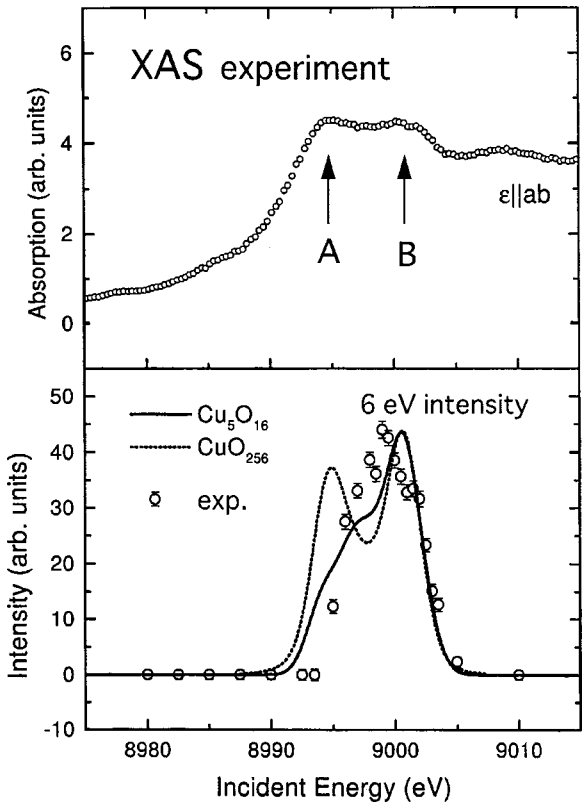

FIG. 49. Experimental spectra and theoretical interpretation for Cu $1s$ spectra in Nd_2CuO_4: top panel, x-ray absorption with the incident-photon polarization in the ab plane; lower panel, experimental result (open circles) for the 6-eV intensity of the Cu $1s\rightarrow 4p_\sigma\rightarrow 1s$ RIXS, and the calculated 6-eV intensity shown with the solid (Cu_5O_{16}) and dotted (CuO_{256}) curves. From Hämäläinen *et al.*, 2000.

More recently Hämäläinen *et al.* (2000) measured a similar 6-eV peak with an ab polarized (perpendicular to the c axis) incident photon. Now the Cu $1s$ electron is excited to the Cu $4p_\sigma$ band, whose energy is about 10 eV higher than the Cu $4p_\pi$ band. Figure 49 shows the experimental data for the Cu transition $1s$-$4p_\sigma$ (top panel) and the intensity of the 6-eV RIXS peak (lower panel) with the open circles. A theoretical calculation has also been made with a Cu_5O_{16} cluster, in which five CuO_4 plaquettes are arranged in the ab plain with D_{4h} symmetry. The calculated result of the 6-eV intensity is

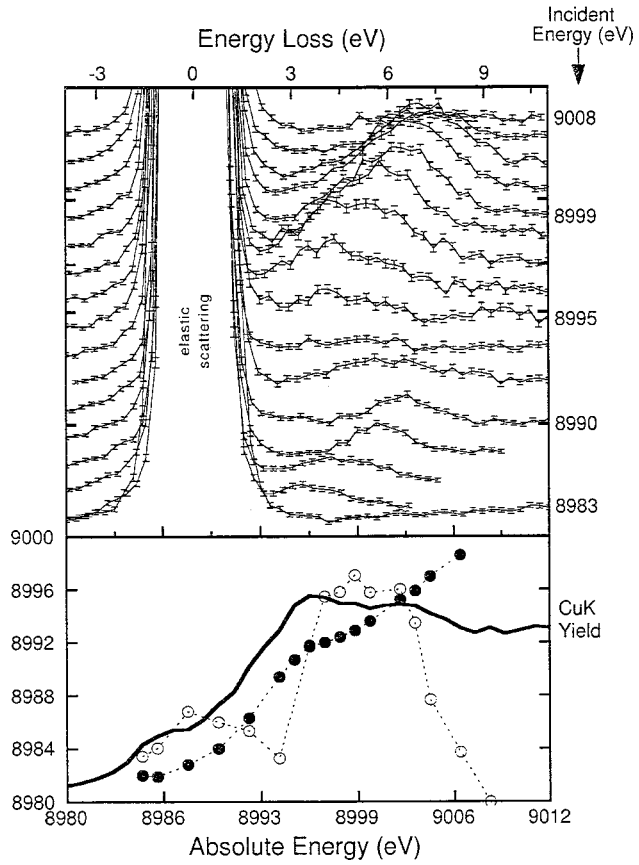

FIG. 50. Experimental RIXS for the Cu transition $1s \rightarrow 4p \rightarrow 1s$ in La_2CuO_4. The upper panel shows the raw spectra plotted as a function of the transferred energy. In the lower panel the open and filled circles are the inelastic peak height and position, respectively, plotted as a function of the incident-photon energy, and the solid curve is the fluorescent yield. From Abbamonte *et al.*, 1999.

shown with the solid curve (lower panel), and the agreement with experiments is good. For comparison the 6-eV intensity calculated with the Anderson impurity model (Cu_1O_{256} cluster) is also shown with the dashed curve, and it is found that the resonance enhancement at the lower XAS feature (denoted by A in the figure) is strongly suppressed with the Anderson impurity model in the case of the Cu_5O_{16} cluster. It is confirmed in this calculation that the reason for suppression of the resonance in the lower XAS feature is the formation of a Zhang-Rice singlet in the intermediate state.

It should be mentioned that Abbamonte *et al.* (1999) recently made similar RIXS measurements of the Cu $1s \rightarrow 4p \rightarrow 1s$ transition in La_2CuO_4 and $Sr_2CuO_2Cl_2$. A result for La_2CuO_4 is shown in Fig. 50, where the incident-photon polarization is in the ab plane and the momentum transfer $\mathbf{k}_1 - \mathbf{k}_2$ is 1.27 Å^{-1} parallel to the c axis. It is interesting to see that the RIXS peak energy depends strongly on the incident-photon energy, in contrast with the result in Nd_2CuO_4 of Hill *et al.* (1998) and Hämäläinen *et al.* (2000). Abbamonte *et al.* explained this behavior in terms of a shakeup picture in third-order perturbation theory which exhibits both incoming and outgoing resonances. In their calculation the Cu $1s$ core-hole potential acting on the $4p$ electron is treated as a lowest-order perturbation but the potential acting on the $3d$ electron is not taken into account, so that the role of the Zhang-Rice singlet state in the intermediate state is disregarded. The electronic excitation in the final state is suggested to be an a_{1g} excitonic state. This physical picture is different from that of Idé and Kotani (1999) and also from that of Hämäläinen *et al.* (2000). It would be interesting to compare the two pictures and check their validity. Abbamonte *et al.* (1999) also made an interesting measurement of the RIXS momentum-transfer dependence in $Sr_2CuO_2Cl_2$, and found that a feature at 2 eV (corresponding to a charge-transfer gap) changes its shape and shifts with changes in $\mathbf{k}_1 - \mathbf{k}_2$.

VI. OTHER TOPICS

There are many other interesting topics relating to RIXS, which we have not discussed so far in this article. Here we give only brief descriptions of some of them because of limited space.

A. Simple metals

The Fermi edge singularity in x-ray absorption and emission of simple metals originates from the many-body screening effect by conduction electrons around a core hole. Since Mahan (1967) and Noziéres and De Dominicis (1969) studied this effect theoretically about 30 years ago, extensive experimental investigations have been made. The measurements have been made mainly for normal x-ray emission with electron-beam excitation of a core electron, but the quality of NXES with synchrotron-radiation excitation is not very good because of the small fluorescence yield, and almost no RIXS data have been reported. One of the central issues of NXES study (Callcott *et al.*, 1978) is the comparison of a singularity exponent with an absorption exponent. The exponents observed in NXES of various materials are often different from those in XAS, though the theory (Noziéres and De Dominicis, 1969) predicts that they should be the same. However, the estimated value of the exponent depends on the quality of experimental data and the method of data analysis, so that it is desirable to measure NXES and RIXS systematically with high resolution, using high-brilliance synchrotron radiation, in future.

In this connection, it should be mentioned that a high-resolution inelastic x-ray scattering experiment has recently been carried out by Krisch *et al.* (1997) for Li $1s$ electron excitation using synchrotron radiation. This experiment is concerned not with RIXS but rather with Thomson scattering, the cross section of which is proportional to the dynamical structure factor $S(\mathbf{k}, \Omega - \omega)$, as shown in Eq. (3), where $\mathbf{k}(=\mathbf{k}_1 - \mathbf{k}_2)$ is the momentum transfer. As proposed by Doniach *et al.* (1971), it is very useful in the study of the Fermi edge singularity to measure the $\mathbf{k}$ dependence of inelastic x-ray scattering, because $S(\mathbf{k}, \Omega - \omega)$ is, in the limit of small $\mathbf{k}$, essentially the same as the x-ray absorption by the dipole transi-

tion, but with increasing **k** the contribution from that by the monopole, quadrupole, and higher-order transitions increases. Krisch *et al.* measured the inelastic x-ray scattering spectra of the Li $1s$ edge for two values of **k**, in each of which the dipole and monopole transitions were dominant, and determined the singularity exponents of the dipole transition ($\alpha_1=0.05$) and monopole transition ($\alpha_0=-0.18$). The values do not agree with those obtained so far from other experiments, but are in good agreement with the theoretical values of Girvin and Hopfield (1976), taking into account both Coulomb and exchange interactions between the core hole and conduction electrons.

B. Transition metals

For transition metals, the $2p\rightarrow 3d\rightarrow 2p$ inelastic scattering was measured for Ni metal (Weinelt *et al.*, 1996), the magnetic circular dichroism (MCD) of NXES for Fe (Hague *et al.*, 1993), and the MCD of RIXS for Fe, Co, and Ni (Duda *et al.*, 1994). Weinelt *et al.* focused their interest on the change in character of RIXS from "Raman scattering" to NXES near the Ni $2p_{3/2}$ threshold. They also measured the resonant x-ray photoemission near the same Ni $2p_{3/2}$ threshold (Weinelt *et al.*, 1997), and found a change in character from "photoemission" to "Auger" through a narrow transition region at the threshold. It should be noted that the resonant emission and photoemission correspond to two different decay channels from a common intermediate state. Although no detailed analysis of the experimental results has been made, the spectrum in the transition region is nothing but the NXES-like spectrum discussed in Secs. V.B and V.C., and the spectrum reflects the interplay between the local and itinerant characters of the $3d$ state of Ni.

The magnetic circular dichroism of x-ray emission was first measured by Hague *et al.* (1993) for the $2p$ core shell in ferromagnetic Fe metal using an effectively white beam of incident radiation. The $2p$ x-ray emission of ferromagnetic Fe metal with a threshold excitation was theoretically predicted from band-structure calculations by Strange *et al.* (1991, 1993), and the experimental result was compared with this theoretical calculation. Even in x-ray emission with white incident radiation, the memory of the circular polarization of the incident photon is left in the core-hole state with strong spin-orbit interaction, so that the Fe $3d\rightarrow 2p$ emission is expected to exhibit a characteristic MCD signal which reflects the spin polarization of the $3d$ band. In Fig. 51, the experimental MCD is shown by the data points, and compared with the theoretical prediction (upper curve). Since the experimental spectral resolution is not very good, the original emission spectrum (which is not shown here) has a broad peak with no structure, but the MCD of the emission clearly shows the dip structure predicted by the theoretical calculation. The good correspondence between experimental (white beam) and theoretical (threshold) excitation results suggests that even with the white incident beam the threshold excitation plays a dominant role in x-ray emission. The MCD of x-ray

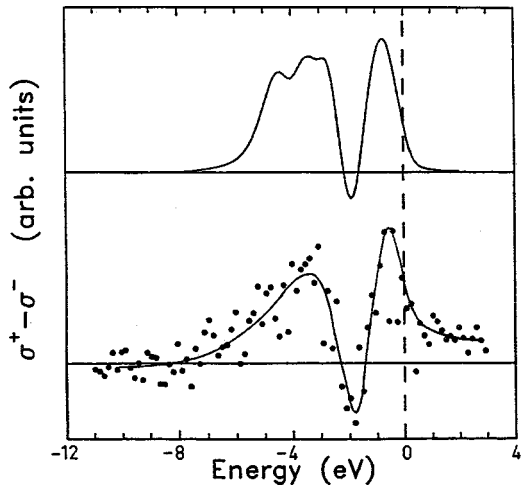

FIG. 51. Normalized magnetic circular dichroism of the emission spectrum with $2p_{3/2}$ core excitation in ferromagnetic Fe metal: upper curve, the theoretical result for the incident-photon energy at the threshold energy; lower panel, the experimental result (the continuous line serves as a guide for the eye). From Hague *et al.*, 1993.

emission in Co-Rh based alloys and Co-Fe multilayers, as well as a Coster-Kronig contribution to the emission MCD of in Fe metal, were also measured by Hague and co-workers (Hague *et al.*, 1995, 1997; Gallet *et al.* 1997, 1998).

Duda *et al.* (1994) measured the MCD of $2p\rightarrow 3d\rightarrow 2p$ RIXS of Fe, Co, and Ni. The observed features of the MCD spectra change in both intensity and sign with a change in the incident-photon energy from below the $2p_{3/2}$ to above the $2p_{1/2}$ excitation thresholds. There has been no energy-band calculation to compare with these experimental results, but Jo and Parlebas (1999) have shown that the most essential features (relative intensity and sign of MCD) can be understood from an atomic model in which the solid-state effect is taken into account only as the average $3d$ electron occupation in each atomic orbital. The present experimental resolution is not very good, so that no fine structure originating from the band density of states or from many-body effects is observed. More precise measurements with higher resolution and more detailed calculation with solid-state effects are desirable in the future.

C. Oxygen 1s x-ray emission in oxide systems

Oxygen $1s$ x-ray emission is very useful for studying the electronic structure of transition-metal oxides (Tsang, 1988; Zhang, 1989; Guo, 1994; Butorin, 1995; Duda, 1997; Kurmaev, 1998). Tunable excitation using synchrotron radiation is important for the site-selective excitation. There are some inequivalent oxygen sites in many oxide crystals. For example, there are in-plane and apical oxygen sites for layered perovskite oxides.

Figure 52 shows O $1s$ absorption spectra in $La_{2-x}Sr_xCuO_4$ for various values of x (Guo, 1994), and the O $1s\rightarrow 2p\rightarrow 1s$ emission spectra for $x=0.07$ are dis-

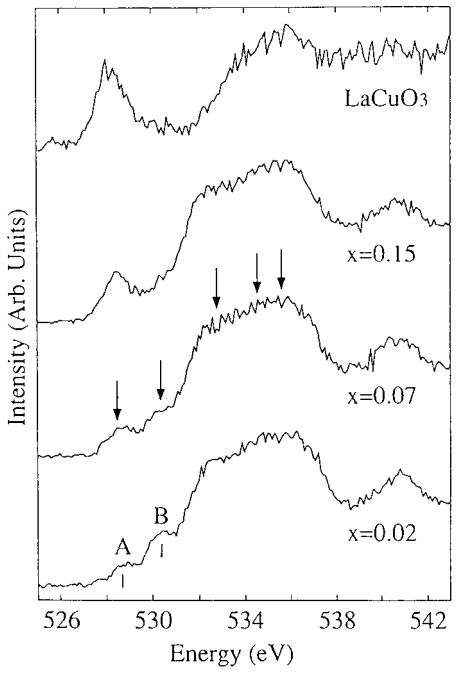

FIG. 52. Experimental data on the O 1*s* x-ray absorption in $La_{2-x}Sr_xCuO_4$ ($x=0$, 0.02, 0.07, and 0.15). From Guo *et al.*, 1994.

played in Fig. 53 for the incident-photon energies indicated by the arrows in Fig. 52. When Ω is tuned to the pre-edge peak at 528.5 eV, the emission spectrum exhibits a double-peak shape, while for $\Omega=532.8$ eV it shows a much narrower and nearly symmetric peak. With further increase in Ω the spectral width increases. According to the LDA band-structure calculation by Redinger

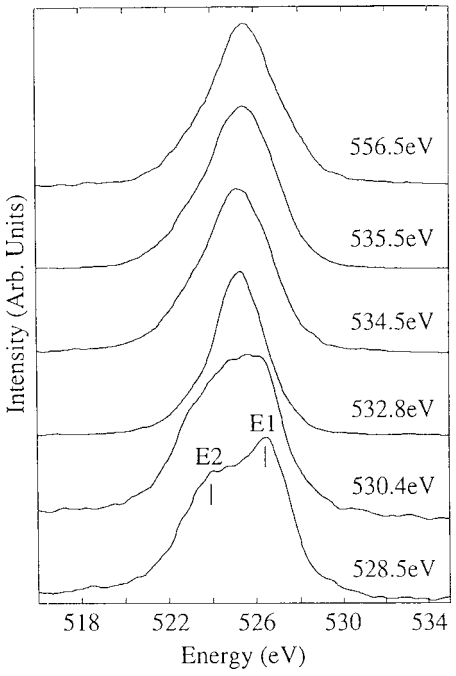

FIG. 53. Experimental data on the O $1s\rightarrow 2p\rightarrow 1s$ emission spectrum in $La_{2-x}Sr_xCuO_4$ ($x=0.07$) for various values of the incident-photon energy. From Guo *et al.*, 1994.

et al. (1987), the local O 2*p* density of states at the apical oxygen site has a double-peak structure, while that at the in-plane site exhibits a much narrower single peak. This is interpreted as evidence that the 528.5-eV excitation resonates with the O 2*p* state at the apical site, and the 532.8-eV excitation resonates with that at the in-plane site, while the 556.5-eV excitation detects both apical and in-plane O 2*p* states. It would be desirable to perform a theoretical analysis of these data using the coherent second-order optical formula and taking into account the electron correlation on the Cu site (note that the O 2*p* state is strongly hybridized with the Cu 3*d* state).

D. Molecules adsorbed on metal surfaces

The chemical bonding between an adsorbed molecule and a metal surface has been one of the main subjects of surface science. Recently, XES has been found to be a powerful experimental technique compared with photoemission spectroscopy, which has been the common experimental technique up to now, because new information on chemical bonding is obtained by XES. When we use the chemical shift of a core level in the excitation of x-ray emission, we can obtain information on the electronic states of a specific chemical bond, and furthermore their symmetries can be resolved by using the angle dependence and polarization dependence of the spectra. X-ray emission spectra have been applied to the study of various adsorbates on metal surfaces, such as molecular CO on Ni and Cu (Wassdahl *et al.*, 1992; Nilsson, Bennich, *et al.*, 1995), benzene and ethylene on Ni and Cu (Weinelt *et al.*, 1998; Triguero *et al.*, 1999), N_2 on Ni (Nilsson *et al.*, 1997; Bennich *et al.*, 1998), and atomic oxygen on Ni and Cu (Tillborg *et al.*, 1993).

Figures 54(a) and (b) show the N 1*s* absorption and emission spectra of an adsorbed N_2 molecule on Ni metal (Bennich *et al.*, 1998). It is known that the N_2 molecular axis is perpendicular to the surface plane. The N 1*s* absorption spectrum comes mainly from the transition from the N 1*s* to the $2p\pi^*$ states, and it is deconvoluted to two bands, which correspond to the contributions from the outer- and inner-N atoms, as shown with the solid curves in Fig. 54(a). By choosing the resonant excitation energy for each N atom, the RIXS spectra could be resolved into the outer- and inner-N atomic spectra. Furthermore, these spectra were measured by two experimental configurations using a rotating spectrometer. If we measure the emission spectrum in a configuration where the emitted x ray goes out normal to the surface, the spectra are related to the occupied molecular orbitals with the π symmetry of the N_2 molecule. On the other hand, if we measure the emission spectra in a configuration with grazing emission, they reflect both σ and π symmetries of N_2 molecular orbitals. Four deconvoluted emission spectra corresponding to the σ and π bands for the outer- and inner-N atoms were obtained by Bennich *et al.*, as shown in Fig. 54(b).

One can see that the intensity ratio of the two σ peaks is quite different for the outer- and inner-N atoms. This

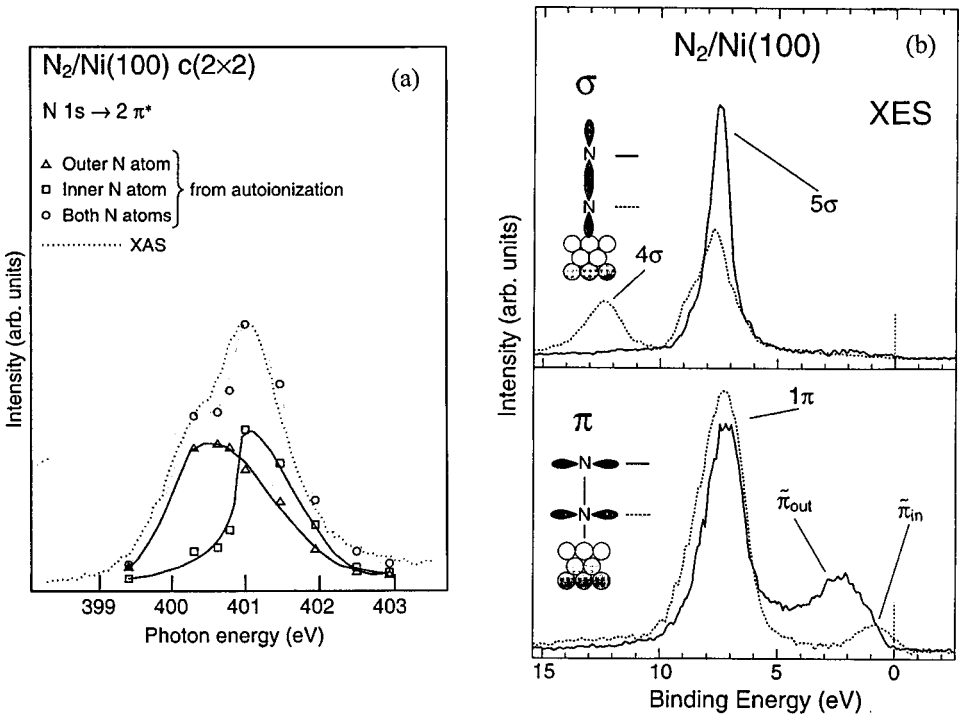

FIG. 54. Spectra involving N 1*s* states for N_2 molecules adsorbed on the Ni (100) surface: (a) x-ray absorption spectra showing the experimental results (dotted) and the deconvolution into contributions from the outer- and inner-N atoms (solid curves); (b) x-ray emission spectra of an N_2 molecule on the Ni (100) surface. The four curves correspond to the spectra of σ and π bands for the outer- and inner-N atoms. From Bennich *et al.*, 1998.

fact indicates that the σ bands of the N_2 molecule are strongly polarized in order to minimize Pauli repulsion with the Ni 4*sp* states in the substrate. In the case of π states, there is a band near the Fermi level. The π state near the Fermi level is found to be a nonbonding state with respect to the Nπ-Ni3*d* orbitals. These experimental results are in conflict with the traditional picture, which is based on a σ donation combined with a back-donation into the π^* level.

E. Interface and buried layers

The penetration depth of an x ray is much longer than that of an electron. Therefore XES is a useful method for probing the interfaces of the multilayers and the buried layers in bulk systems. Such experiments have been carried out for semiconductors (Perera, *et al.*, 1989; Carlisle, Terminello, *et al.*, 1995; Nilsson, Kanski, *et al.*, 1995; Ederer *et al.*, 1996; Agui *et al.*, 1999) and metals (Duda *et al.*, 1996; Nilsson *et al.*, 1996).

Figure 55 shows the Si 2*p* normal emission spectra of bulk Si, one monolayer (ML), and three ML's of Si embedded deep below a GaAs (001) surface (Nilsson, Kanski, *et al.*, 1995). For the 3-ML spectrum, a 0.26-eV shift of the high-energy edge is found, as compared with the bulk Si spectrum. Nilsson *et al.* interpreted the shift as originating from the Si chemical core-level shift due to the neighboring As atoms. For the 1-ML spectrum, a new peak appears around 86 eV, which is interpreted as a hybridization effect between the Si *s* states and the As *s* states. Interface states of BN (Perera, *et al.*, 1989) and AlAs layers (Agui *et al.*, 1999) have also been observed by NXES in addition to the bulk states. In the case of a superlattice of metals, (Duda *et al.*, 1996; Nilsson *et al.*), the 3*d* band becomes narrow and the spectra are consistent with the band calculation.

VII. CONCLUDING REMARKS

We have reviewed recent developments in the study of RIXS for semiconductors, insulators, and *f* and *d* electron systems. For semiconductors and insulators, such as Si, graphite, and diamond, the RIXS spectra reflect the energy-band dispersion through momentum conservation. For *f* and *d* electron systems, the effects of electron correlation are important, and the RIXS spectra reflect the multiplet excitation, the charge-transfer excitation, the crystal-field level excitation, and so on. The interplay between the intra-atomic Coulomb interaction and interatomic hybridization is taken into account theoretically by the Anderson impurity model or cluster models. The limitations of the band model and Anderson impurity model are also discussed in describing the RIXS of transition-metal compounds.

The effects of phonon relaxation have been discussed for semiconductors and insulators formed from light elements, but not for *f* and *d* electron systems. Usually, the phonon relaxation effect is not important in relatively heavy elements, because the core-hole lifetime is shorter than the phonon relaxation time. For instance, the lifetime broadening of the C 1*s* core level is of the order of 0.1 eV, which is comparable with the electron-phonon coupling energy, but the lifetime broadening of the 2*p* level of rare-earth elements is of the order of 1–10 eV, which is larger than the electron-phonon coupling energy. So, in most RIXS of *f* and *d* electron systems, the relaxation by the electron-electron interaction, which is comparable with the core-level lifetime width, is much more important than the electron-phonon interac-

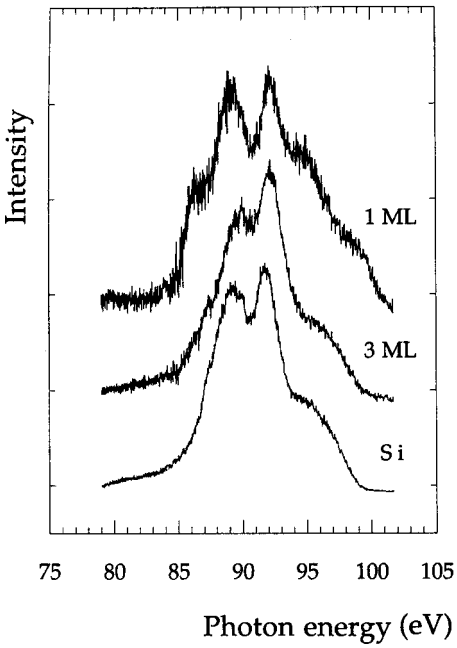

FIG. 55. Experimental normal emission spectra (NXES) of Si $2p$ in bulk Si, compared with 1- and 3-monolayer Si/GaAs heterostructure spectra. From Nilsson, Kanski, *et al.*, 1995.

tion. However, we expect that the phonon relaxation effect could also be observed in high-resolution RIXS measurements for some shallow core levels of f and d electron systems.

Let us note the important differences between RIXS in the soft-x-ray and hard-x-ray regions. In the soft-x-ray region, we can take the long-wavelength limit for the incident and emitted photons (i.e., $\mathbf{k}_1 \sim \mathbf{k}_2 \sim 0$), but in the hard-x-ray region we have to take into account that $\mathbf{k}_1$ and $\mathbf{k}_2$ are finite. One of the effects of the finite photon wave vector is the occurrence of electric quadrupole transitions in addition to electric dipole transitions. The contribution of quadrupole transitions in the optical excitation process has been discussed in Secs. IV.D and V.B for the $2p \rightarrow 4f$ transition in rare earths and the $1s \rightarrow 3d$ transition in transition-metal elements. It would also be interesting to study the contribution of the quadrupole transition in the deexcitation process, although no detailed research has been carried out so far.

Another effect of finite $\mathbf{k}_1$ and $\mathbf{k}_2$ is their contribution to momentum conservation. If we assume the independent-electron approximation, the momentum conservation rule Eq. (21) is now changed into

$$\mathbf{k}_c = \mathbf{k}_v + (\mathbf{k}_1 - \mathbf{k}_2) + \mathbf{G} \tag{46}$$

where $\mathbf{G}$ is a reciprocal-lattice vector. The importance of this effect has been reported in the RIXS literature with respect to the Si $1s$ core electron excitation (Ma *et al.*, 1995). More generally (beyond the independent-electron approximation), the RIXS spectrum (5) is expressed as a function of Ω, ω, and $\mathbf{k}_1 - \mathbf{k}_2$. The momentum-transfer dependence of the spectra gives important information on the dispersion of the electronic excitations, as discussed by Platzman and Isaacs (1998), who measured the momentum dependence of RIXS involving states in $NiS_{1.5}Se_{0.5}$ that originated from charge-transfer excitations. It is interesting to study the momentum dependence of the charge-transfer excitation of Cu oxide systems. If the resolution of RIXS is improved, it will also be interesting to measure the dispersion of the collective orbital excitation (orbital wave) by RIXS in the orbital ordered perovskite manganites, which are materials of current interest exhibiting colossal magnetoresistance. Theoretical predictions of the momentum-dependent RIXS are given for the charge-transfer excitation of cuprates by Tsutsui *et al.* (1999) and for the orbital wave of perovskite manganites by Ishihara and Maekawa (1999).

The study of RIXS will be advanced further with the development of the third and fourth generations of synchrotron radiation sources in the future.

ACKNOWLEDGMENTS

The authors would like to thank A. Agui, S. M. Butorin, T. A. Callcott, F. M. F. de Groot, L. C. Duda, D. L. Ederer, M. Fujisawa, K. Fukui, K. Hämäläinen, C. Hague, I. Harada, Y. Harada, J. P. Hill, T. Idé, Y. Kayanuma, C.-C. Kao, P. Lagarde, J.-M. Mariot, M. Matsubara, M. Nakazawa, J. Nordgren, H. Ogasawara, K. Okada, J. C. Parlebas, R. C. C. Perera, M. Pompa, M. Taguchi, S. Tanaka, T. Uozumi, and M. Watanabe, for collaborations and discussions. This work was partially supported by a Grant-in-Aid for Scientific Research from the Ministry of Education, Science, Culture and Sports in Japan.

REFERENCES

Abbamonte, P., C. A. Burns, E. D. Isaacs, P. M. Platzman, L. L. Miller, S. W. Cheong, and M. V. Klein, 1999, Phys. Rev. Lett. **83**, 860.

Agui, A., S. Shin, M. Fujisawa, Y. Tezuka, T. Ishii, Y. Muramatsu, O. Mishima, and K. Era, 1997, Phys. Rev. B **55**, 2073.

Agui, A., S. Shin, C. Wu, K. Shiba, and K. Inoue, 1999, Phys. Rev. B **59**, 10 792.

Allen, J. W., S. J. Oh, O. Gunnarsson, K. Schönhammer, M. B. Maple, M. S. Torikachvili, and I. Lindau, 1986, Adv. Phys. **35**, 275.

Anderson, P. W., 1961, Phys. Rev. **124**, 41.

Bartolomé, F., J. M. Tonnerre, L. Sève, D. Raoux, J. Chaboy, L. M. García, M. Krisch, and C. C. Kao, 1997, Phys. Rev. Lett. **79**, 3775.

Bearden, J. A., 1967, Rev. Mod. Phys. **39**, 78.

Bennich, P., T. Wiell, O. Karis, M. Weinelt, N. Wassdahl, A. Nilsson, M. Nyberg, L. G. M. Pettersson, J. Stöhr, and M. Samant, 1998, Phys. Rev. B **57**, 9274.

Bickers, N. E., D. L. Cox, and J. W. Wilkins, 1985, Phys. Rev. Lett. **54**, 230.

Braicovich, L., N. B. Brookes, C. Dallera, M. Salvietti, and G. L. Olcese, 1997, Phys. Rev. B **56**, 15 047.

Braicovich, L., C. Dallera, G. Ghiringhelli, N. B. Brookes, J. B. Goedkoop, and M. A. van Veenendaal, 1997, Phys. Rev. B **55**, R15 989.

Braicovich, L., G. van der Laan, G. Ghiringhelli, A. Tagliaferri, M. A. van Veenendaal, N. B. Brookes, M. M. Chervinskii, C. Dallera, B. De Michelis, and H. A. Dürr, 1999, Phys. Rev. Lett. **82**, 1566.

Butorin, S. M., L. C. Duda, J. H. Guo, N. Wassdahl, J. Nordgren, M. Nakazawa, and A. Kotani, 1997, J. Phys.: Condens. Matter **9**, 8155.

Butorin, S. M., J.-H. Guo, M. Magnuson, P. Kuiper, and J. Nordgren, 1996, Phys. Rev. B **54**, 4405.

Butorin, S. M., H. Guo, M. Magnuson, and J. Nordgren, 1997, Phys. Rev. B **55**, 4242.

Butorin, S. M., J.-H. Guo, D. K. Shuh, A. Kotani, and J. Nordgren, 1997, unpublished.

Butorin, S. M., J.-H. Guo, N. Wassdahl, P. Skytt, J. Nordgren, Y. Ma, C. Ström, L.-G. Johansson, and M. Qvarford, 1995, Phys. Rev. B **51**, 11 915.

Butorin, S. M., M. Magnuson, K. Ivanov, D. K. Shuh, T. Takahashi, S. Kunii, J.-H. Guo, and J. Nordgren, 1999, J. Electron Spectrosc. Relat. Phenom. **101–103**, 783.

Butorin, S. M., D. C. Mancini, J.-H. Guo, N. Wassdahl, J. Nordgren, M. Nakazawa, S. Tanaka, T. Uozumi, A. Kotani, Y. Ma, K. E. Myano, B. A. Karlin, and D. K. Shuh, 1996, Phys. Rev. Lett. **77**, 574.

Caliebe, W. A., C.-C. Kao, J. B. Hastings, M. Taguchi, A. Kotani, T. Uozumi, and F. M. F. de Groot, 1998, Phys. Rev. B **58**, 13 452.

Callcott, T. A., E. T. Arakawa, and D. L. Ederer, 1978, Phys. Rev. B **18**, 6622.

Callcott, T. A., W. L. O'Brien, J. J. Jia, Q. Y. Dong, D. L. Ederer, R. N. Watts, and D. R. Mueller, 1992, Nucl. Instrum. Methods Phys. Res. A **319**, 128.

Callcott, T. A., K. L. Tsang, C. H. Zhang, D. L. Ederer, and E. T. Arakawa, 1986, Rev. Sci. Instrum. **57**, 2680.

Carlisle, J. A., E. L. Shirley, E. A. Hudson, L. J. Terminello, T. A. Callcott, J. J. Jia, D. L. Ederer, R. C. C. Perera, and F. J. Himpsel, 1995, Phys. Rev. Lett. **74**, 1234.

Carlisle, J. A., E. L. Shirley, L. J. Terminello, J. J. Jia, T. A. Callcott, D. L. Ederer, R. C. C. Perera, and F. J. Himpsel, 1999, Phys. Rev. B **59**, 7433.

Carlisle, J. A., L. J. Terminello, E. A. Hudson, R. C. C. Perera, J. H. Underwood, T. A. Callcott, J. J. Jia, D. L. Ederer, F. J. Himpsel, and M. G. Samant, 1995, Appl. Phys. Lett. **67**, 34.

Carra, P., B. T. Thole, M. Altarelli, and X. Wang, 1993, Phys. Rev. Lett. **70**, 694.

Carra, P., M. Fabrizio, and B. T. Thole, 1995, Phys. Rev. Lett. **74**, 3700.

Chelikowsky, J. R., and M. L. Cohen, 1976, Phys. Rev. B **14**, 556.

Cowan, R. D., 1981, *The Theory of Atomic Structure and Spectra* (University of California, Berkeley).

de Groot, F. M. F., 1994, J. Electron Spectrosc. Relat. Phenom. **67**, 529.

de Groot, F. M. F., M. A. Arrio, Ph. Sainctavit, Ch. Cartier, and C. T. Chen, 1994, Solid State Commun. **92**, 991.

de Groot, F. M. F., A. Fontaine, C. C. Kao, and M. Krisch, 1994, J. Phys.: Condens. Matter **6**, 6875.

de Groot, F. M. F., P. Kuiper, and G. A. Sawatzky, 1998, Phys. Rev. B **57**, 14 584.

de Groot, F. M. F., M. Nakazawa, A. Kotani, M. H. Krisch, and F. Sette, 1997, Phys. Rev. B **56**, 7285.

Dong, Q.-Y., W. L. O'Brien, J. J. Jia, T. A. Callcott, D. R. Mueller, and D. L. Ederer, 1992, Phys. Rev. B **46**, 15 116.

Doniach, S., P. M. Platzman, and J. T. Yue, 1971, Phys. Rev. B **4**, 3345.

Duda, L.-C., 1996, Ph.D. thesis (Uppsala University).

Duda, L. C., G. Dräger, S. Tanaka, A. Kotani, J. Guo, D. Heumann, S. Bocharov, N. Wassdahl, and J. Nordgren, 1998, J. Phys. Soc. Jpn. **67**, 416.

Duda, L.-C., J.-H. Guo, J. Nordgren, C. B. Stagarescu, K. E. Smith, W. McCarroll, K. Ramanujachary, and M. Greenblatt, 1997, Phys. Rev. B **56**, 1284.

Duda, L.-C., P. Isberg, S. Mirbt, J.-H. Guo, B. Hjorvarsson, J. Nordgren, and P. Granberg, 1996, Phys. Rev. B **54**, 10 393.

Duda, L.-C., J. Stöhr, D. C. Mancini, A. Nilsson, N. Wassdahl, J. Nordgren, and M. G. Samant, 1994, Phys. Rev. B **50**, 16 758.

Duda, L.-C., C. B. Stagarescu, J. Downes, K. E. Smith, D. Korakakis, T. D. Moustakas, J. Guo, and J. Nordgren, 1998, Phys. Rev. B **58**, 1928.

Dufek, P., K. Schwarz, and P. Blaha, 1992, Phys. Rev. B **48**, 12 672.

Ederer, D. L., J. A. Carlisle, J. Jiménez, J. J. Jia, K. Osborn, T. A. Callcott, R. C. C. Perera, J. H. Underwood, L. J. Terminello, A. Asfaw, and F. J. Himpsel, 1996, J. Vac. Sci. Technol. A **14**, 859.

Ederer, D. L., and J. H. McGuire, 1996, Eds., *Raman Emission by X-Ray Scattering* (World Scientific, Singapore).

Ederer, D. L., K. E. Miyano, W. L. O'Brien, T. A. Callcott, Q.-Y. Dong, J. J. Jia, D. R. Mueller, J.-E. Rubensson, R. C. C. Perera, and R. Shuker, 1994, in *New Directions in Research with Third-Generation Soft X-ray Synchrotron Radiation Sources*, edited by A. S. Schlachter and F. J. Wuilleumier (Kluwer Academic, Dordrecht), p. 281.

Eisebitt, S., J. Lüning, J.-E. Rubensson, T. Van Buuren, S. N. Patitsas, T. Tiedje, M. Berger, R. Arens-Fischer, S. Frohnhoff, and W. Eberhard, 1996, Solid State Commun. **97**, 549.

Eisenberger, P., P. M. Platzman, and H. Winick, 1976a, Phys. Rev. Lett. **36**, 623.

Eisenberger, P., P. M. Platzman, and H. Winick, 1976b, Phys. Rev. B **13**, 2377.

Fano, U., 1961, Phys. Rev. **124**, 1866.

Finkelstein, L. D., E. Z. Kurmaev, M. A. Korotin, A. Moewes, B. Schneider, S. M. Butorin, J.-H. Guo, J. Nordgren, D. Hartmann, M. Neumann, and D. L. Ederer, 1999, Phys. Rev. B **60**, 2212.

Fujimori, A., and Y. Tokura, 1995, Eds., *Spectroscopy of Mott Insulators and Correlated Metals* (Springer, Heidelberg).

Fujishima, Y., Y. Tokura, T. Arima, and S. Uchida, 1993, Phys. Rev. B **48**, 511.

Gallet, J.-J., J. M. Mariot, C. F. Hague, J. P. Kappler, J. Goulon, A. Rogalev, G. Krill, M. Sacchi, and K. Hricovini, 1997, J. Phys. IV **7**, C2-365.

Gallet, J.-J., J.-M. Mariot, C. F. Hague, F. Sirotti, M. Nakazawa, H. Ogasawara, and A. Kotani, 1996, Phys. Rev. B **54**, 14 238.

Gallet, J.-J., J.-M. Mariot, L. Journel, C. F. Hague, J.-P. Kappler, G. Schmerber, D. J. Singh, G. Krill, J. Goulon, and A. Rogalev, 1998, Phys. Rev. B **57**, 7835.

Gallet, J.-J., J. M. Mariot, L. Journel, C. F. Hague, A. Rogalev, H. Ogasawara, A. Kotani, and M. Sacchi, 1999, Phys. Rev. B **60**, 14 128.

Girvin, S. M., and J. J. Hopfield, 1976, Phys. Rev. Lett. **37**, 1091.

Gunnarsson, O., and K. Schönhammer, 1983, Phys. Rev. B **28**, 4315.
Guo, J.-H., S. M. Butorin, N. Wassdahl, P. Skytt, J. Nordgren, and Y. Ma, 1994, Phys. Rev. B **49**, 1376.
Guo, J.-H., P. Glans, P. Skytt, N. Wassdahl, J. Nordgren, Y. Luo, H. Ågren, Y. Ma, T. Warwick, P. Heimann, E. Rotenberg, and J. D. Denlinger, 1995, Phys. Rev. B **52**, 10 681.
Guo, J.-H., N. Wassdahl, P. Skytt, S. M. Butorin, L.-C. Duda, C. J. Englund, and J. Nordgren, 1995, Rev. Sci. Instrum. **66**, 1561.
Hague, C. F., J.-M. Mariot, and J.-J. Gallet, 1997, Appl. Phys. A: Mater. Sci. Process. **65**, 141.
Hague, C. F., J.-M. Mariot, G. Y. Guo, K. Hricovini, and G. Krill, 1995, Phys. Rev. B **51**, 1370.
Hague, C. F., J.-M. Mariot, P. Strange, P. J. Durham, and B. L. Gyorffy, 1993, Phys. Rev. B **48**, 3560.
Hämäläinen, K., C.-C. Kao, B. Hastings, D. P. Siddons, L. E. Berman, V. Stojanoff, and S. P. Cramer, 1992, Phys. Rev. B **46**, 14 274.
Hämäläinen, K., J. P. Hill, S. Huotari, C.-C. Kao, L. E. Berman, A. Kotani, T. Idé, J. L. Peng, and R. L. Greene, 2000, Phys. Rev. B **61**, 1836.
K. Hämäläinen, D. P. Siddons, J. B. Hastings, and L. E. Berman, 1991, Phys. Rev. Lett. **67**, 2850.
Hanamura, E., H. Suzuura, A. Agui, and S. Shin, 1997, Phys. Rev. B **56**, 6384.
Harada, Y., H. Ishii, M. Fujisawa, Y. Tezuka, S. Shin, M. Watanabe, Y. Kitajima, and A. Yagishita, 1998, J. Synchrotron Radiat. **5**, 1013.
Harada, Y., T. Kinugasa, R. Eguchi, M. Matsubara, A. Kotani, S. Shin, M. Watanabe, and A. Yagishita, 2000, Phys. Rev. B **61**, 12 854.
Heitler, W., 1944, *The Quantum Theory of Radiation* (Oxford University, Oxford).
Higuchi, T., T. Tsukamoto, M. Watanabe, M. M. Grush, T. A. Callcott, R. C. Perera, Y. Harada, Y. Tezuka, D. L. Ederer, Y. Tokura, and S. Shin, 1999, Phys. Rev. B **60**, 7711.
Hill, J. P., C. C. Kao, W. A. C. Caliebe, M. Matsubara, A. Kotani, J. L. Peng, and R. L. Greene, 1998, Phys. Rev. Lett. **80**, 4967.
Hohenberg, P., and W. Kohn, 1964, Phys. Rev. **136**, B864.
Hüfner, S., 1995, *Photoelectron Spectroscopy* (Springer, Berlin).
Idé, T., and A. Kotani, 1998, J. Phys. Soc. Jpn. **67**, 3621.
Idé, T., and A. Kotani, 1999, J. Phys. Soc. Jpn. **68**, 3100.
Idé, T., and A. Kotani, 2000a, J. Phys. Soc. Jpn. **69**, 1895.
Idé, T., and A. Kotani, 2000b, J. Phys. Soc. Jpn. **69**, 3107.
Ishihara, S., and S. Maekawa, 1999, Jpn. J. Appl. Phys., Suppl. **38**, 1, 400.
Iwazumi, T., K. Kobayashi, S. Kishimoto, T. Nakamura, S. Nanao, D. Ohshima, R. Katano, and Y. Isozumi, 1997, Phys. Rev. B **56**, R14 267.
Jia, J. J., T. A. Callcott, A. Asfaw, J. A. Carlisle, L. J. Terminello, D. L. Ederer, F. J. Himpsel, and R. C. C. Perera, 1995, Phys. Rev. B **52**, 4904.
Jia, J. J., T. A. Callcott, D. L. Ederer, and R. C. C. Perera, 1998, J. Electron Spectrosc. Relat. Phenom. **92**, 181.
Jia, J. J., T. A. Callcott, W. L. O'Brien, Q. Y. Dong, D. R. Mueller, D. L. Ederer, Z. Tan, and J. I. Budnick, 1992, Phys. Rev. B **46**, 9446.
Jia, J. J., T. A. Callcott, W. L. O'Brien, Q. Y. Dong, J.-E. Rubensson, D. R. Mueller, D. L. Ederer, and J. E. Rowe, 1991, Phys. Rev. B **43**, 4863.
Jia, J. J., T. A. Callcott, E. L. Shirley, J. A. Carlisle, L. J. Terminello, A. Asfaw, D. L. Ederer, F. J. Himpsel, and R. C. C. Perera, 1996, Phys. Rev. Lett. **76**, 4054.
Jiménez-Mier, J., J. van Ek, D. L. Ederer, T. A. Callcott, J. Jia, J. Carlisle, L. Terminello, A. Asfaw, and R. C. Perera, 1999, Phys. Rev. B **59**, 2649.
Jo, T., and J. C. Parlebas, 1999, J. Phys. Soc. Jpn. **68**, 1392.
Jo, T., and A. Tanaka, 1998, J. Phys. Soc. Jpn. **67**, 1457.
Journel, L., M. Sacchi, J.-J. Gallet, C. F. Hague, J.-M. Mariot, N. B. Brookes, M. Finazzi, W. Felsch, and G. Krill, 1999, J. Electron Spectrosc. Relat. Phenom. **101-103**, 733.
Kanamori, J., and A. Kotani, 1988, Eds., *Core-Level Spectroscopy in Condensed Systems* (Springer, Heidelberg).
Kao, C.-C., W. A. L. Caliebe, J. B. Hastings, and J.-M. Gillet, 1996, Phys. Rev. B **54**, 16 361.
Kayanuma, Y., and A. Kotani, 1988, in *Core-Level Spectroscopy in Condensed Systems*, edited by J. Kanamori and A. Kotani (Springer, Heidelberg), p. 72.
Kohn, W., and L. J. Sham, 1965, Phys. Rev. **140**, A1133.
Kotani, A., 1993, Jpn. J. Appl. Phys., Part 1 **32**, 3.
Kotani, A., 1996, in *Correlations in Clusters and Related Systems*, edited by J.-P. Connerade (World Scientific, Singapore), p. 115.
Kotani, A., 1997, J. Phys. IV **7**, 1.
Kotani, A., 1998, J. Electron Spectrosc. Relat. Phenom. **92**, 171.
Kotani, A., 1999, Jpn. J. Appl. Phys., Suppl. **38**, 1, 354.
Kotani, A., T. Jo, and J. C. Parlebas, 1988, Adv. Phys. **37**, 37.
Kotani, A., H. Mizuta, T. Jo, and J. C. Parlebas, 1985, Solid State Commun. **53**, 805.
Kotani, A., and H. Ogasawara, 1992, J. Electron Spectrosc. Relat. Phenom. **60**, 257.
Kotani, A. and K. Okada, 1990, Prog. Theor. Phys. Suppl. **101**, 329.
Kotani, A., and Y. Toyozawa, 1973a, J. Phys. Soc. Jpn. **35**, 1073.
Kotani, A., and Y. Toyozawa, 1973b, J. Phys. Soc. Jpn. **35**, 1082.
Kotani, A., and Y. Toyozawa, 1974, J. Phys. Soc. Jpn. **37**, 912.
Kramers, H. H., and W. Heisenberg, 1925, Z. Phys. **31**, 681.
Krause, M. O., 1979, J. Phys. Chem. Ref. Data **8**, 307.
Krisch, M. H., C. C. Kao, F. Sette, W. A. Caliebe, K. Hämäläinen, and L. B. Hastings, 1995, Phys. Rev. Lett. **74**, 4931.
Krisch, M. H., F. Sette, U. Bergmann, C. Masciovecchio, R. Verbeni, J. Goulon, W. Caliebe, and C. C. Kao, 1996, Phys. Rev. B **54**, R12 673.
Krisch, M. H., F. Sette, C. Masciovecchio, and R. Verbeni, 1997, Phys. Rev. Lett. **78**, 2843.
Kuiper, P., H.-H. Guo, C. Såthe, L.-C. Duda, J. Nordgren, J. J. M. Pothuizen, F. M. F. de Groot, and G. A. Sawatzky, 1998, Phys. Rev. Lett. **80**, 5204.
Kurmaev, E. Z. M. A. Korotin, V. R. Galakhov, L. D. Finkelstein, E. I. Zabolotzky, N. N. Efremova, N. I. Lobachevskaya, S. Stadler, D. L. Ederer, T. A. Callcott, L. Zhou, A. Moewes, S. Bartkowski, M. Neumann, J. Matsuno, T. Mizokawa, A. Fujimori, and J. Mitchell, 1999, Phys. Rev. B **59**, 12 799.
Kurmaev, E. Z., S. Stadler, D. L. Ederer, Y. Harada, S. Shin, M. M. Grush, T. A. Callcott, R. C. C. Perera, D. A. Zatsepin, N. Ovechkina, M. Kasai, Y. Tokura, T. Takahashi, K. Chandrasekaran, R. Vijayaraghavan, and U. V. Varadaraju, 1998, Phys. Rev. B **57**, 1558.
Laubschat, C., E. Weschke, C. Holtz, M. Domke, O. Strebel, and G. Kindl, 1990, Phys. Rev. Lett. **65**, 1639.

Lawrence, J. M., J. D. Thompson, and Y. Y. Chen, 1985, Phys. Rev. Lett. **54**, 2537.
Loeffen, P. W., R. F. Pettifer, S. Müllender, M. A. van Veenendaal, J. Röhler, and D. S. Sivia, 1996, Phys. Rev. B **54**, 14 877.
Luo, Y., H. Ågren, F. Gel'mukhanov, J. Guo, P. Skytt, N. Wassdahl, and J. Nordgren, 1995, Phys. Rev. B **52**, 14 479.
Ma, Y., 1994, Phys. Rev. B **49**, 5799.
Ma, Y., P. Skytt, N. Wassdahl, P. Glans, D. C. Mancini, J. Guo, and J. Nordgren, 1993, Phys. Rev. Lett. **71**, 3725.
Ma, Y., N. Wassdahl, P. Skytt, J. Guo, J. Nordgren, P. D. Johnson, J.-E. Rubensson, T. Boske, W. Eberhardt, and S. D. Kevan, 1992, Phys. Rev. Lett. **69**, 2598.
Ma, Y., K. E. Miyano, P. L. Cowan, Y. Aglitzkiy, and B. A. Karlin, 1995, Phys. Rev. Lett. **74**, 478.
Magnuson, M., S. M. Butorin, J.-H. Guo, A. Agui, J. Nordgren, H. Ogasawara, A. Kotani, T. Takahashi, and S. Kunii, 2001, Phys. Rev. B **63**, 075101.
Mahan, G. D., 1967, Phys. Rev. **163**, 612.
Mariot, J.-M., J.-J. Gallet, L. Journel, C. F. Hague, W. Felsch, G. Krill, M. Sacchi, J.-P. Kappler, A. Rogalev, and J. Goulon, 1999, Physica B **256-261**, 1136.
Materlik, G., C. J. Sparks, and K. Fischer 1994, Eds., *Resonant Anomalous X-Ray Scattering: Theory and Applications* (North-Holland, Amsterdam).
Matsubara, M., T. Uozumi, A. Kotani, Y. Harada, and S. Shin, 2000, J. Phys. Soc. Jpn. **69**, 1558.
Minami, T., 1998, J. Phys. Soc. Jpn. **67**, 3958.
Minami, T., and K. Nasu, 1998, Phys. Rev. B **57**, 12 084.
Miyano, K. E., D. L. Ederer, T. A. Callcott, W. L. O'Brien, J. J. Jia, L. Zhou, Q.-Y. Dong, Y. Ma, J. C. Woicik, and D. R. Mueller, 1993, Phys. Rev. B **48**, 1918.
Moewes, A., D. L. Ederer, M. M. Grush, and T. A. Callcott, 1999, Phys. Rev. B **59**, 5452.
Moewes, A., T. Eskildson, D. L. Ederer, J. Wang, J. McGuire, and T. A. Callcott, 1998, Phys. Rev. B **57**, 8059.
Moewes, A., S. Stadler, R. P. Winarski, D. L. Ederer, M. M. Grush, and T. A. Callcott, 1998, Phys. Rev. B **58**, 15 951.
Mueller, D. R., D. L. Ederer, J. van Ek, W. L. O'Brien, Q. Y. Dong, J. Jia, and T. A. Callcott, 1996, Phys. Rev. B **54**, 15 034.
Muramatsu, Y., M. Oshima, and H. Kato, 1993, Phys. Rev. Lett. **71**, 448.
Nakano, T., A. Kotani, and J. C. Parlebas, 1987, J. Phys. Soc. Jpn. **56**, 2201.
Nakazawa, M., 1998, Ph.D. thesis (University of Tokyo).
Nakazawa, M., H. Ogasawara, A. Kotani, and P. Lagarde, 1998, J. Phys. Soc. Jpn. **67**, 323.
Nakazawa, M., S. Tanaka, T. Uozumi, and A. Kotani, 1996, J. Phys. Soc. Jpn. **65**, 2303.
Nakazawa, M., H. Ogasawara, and A. Kotani, 2000, J. Phys. Soc. Jpn. **69**, 4071.
Nilsson, A., P. Bennich, T. Wiell, N. Wassdahl, N. Mårtensson, J. Nordgren, O. Björneholm, and J. Stöhr, 1995, Phys. Rev. B **51**, 10 244.
Nilsson, P. O., J. Kanski, J. V. Thordson, T. G. Andersson, J. Nordgren, J. Guo, and M. Magnuson, 1995, Phys. Rev. B **52**, 8643.
Nilsson, P. O., J. Stöhr, T. Wiell, M. Aldén, P. Bennich, N. Wassdahl, M. G. Samant, S. S. P. Parkin, N. Mårtensson, J. Nordgren, B. Johansson, and H. L. Skriver, 1996, Phys. Rev. B **54**, 2917.
Nilsson, A., M. Weinelt, T. Wiell, P. Bennich, O. Karis, N. Wassdahl, J. Stöhr, and M. Samant, 1997, Phys. Rev. Lett. **78**, 2847.
Nordgren, J., 1994, in *New Directions in Research with Third-Generation Soft X-ray Synchrotron Radiation Sources*, edited by A. S. Schlachter and F. J. Wuilleumier (Kluwer Academic, Dordrecht), p. 189.
Nordgren, J., and E. Z. Kurmaev, Eds., 2000, *Soft X-Ray Emission Spectroscopy*, J. Electron Spectrosc. Relat. Phenom. **110-111**, pp. 1–363.
Nozières, P., and C. T. De Dominicis, 1969, Phys. Rev. **178**, 1097.
O'Brien, W. L., J. Jia, Q.-Y. Dong, T. A. Callcott, D. R. Mueller, and D. L. Ederer, 1992, Phys. Rev. B **45**, 3822.
O'Brien, W. L., J. Jia, Q.-Y. Dong, T. A. Callcott, D. R. Mueller, D. L. Ederer, and C.-C. Kao, 1993, Phys. Rev. B **47**, 15 482.
O'Brien, W. L., J. Jia, Q.-Y. Dong, T. A. Callcott, K. E. Miyano, D. L. Ederer, D. R. Mueller, and C.-C. Kao, 1993a, Phys. Rev. B **47**, 140.
O'Brien, W. L., J. Jia, Q.-Y. Dong, T. A. Callcott, K. E. Miyano, D. L. Ederer, D. R. Mueller, and C.-C. Kao, 1993b, Phys. Rev. Lett. **70**, 238.
O'Brien, W. L., J. Jia, Q.-Y. Dong, T. A. Callcott, D. L. Mueller, D. L. Ederer, N. D. Shinn, and S. C. Woronick, 1991, Phys. Rev. B **44**, 13 277.
O'Brien, W. L., J. Jia, Q.-Y. Dong, T. A. Callcott, J.-E. Rubensson, D. L. Mueller, and D. L. Ederer, 1991, Phys. Rev. B **44**, 1013.
Ogasawara, H., and A. Kotani, 1995, J. Phys. Soc. Jpn. **64**, 1394.
Okada, K., and A. Kotani, 1993, J. Electron Spectrosc. Relat. Phenom. **62**, 131.
Okada, K., and A. Kotani, 1997, J. Electron Spectrosc. Relat. Phenom. **86**, 119.
Okada, K., and A. Kotani, 2000, J. Phys. Soc. Jpn. **69**, 3100.
Peng, G., X. Wang, C. Randall, J. Moore, and S. P. Cramer, 1994, Appl. Phys. Lett. **65**, 2527.
Perera, R. C. C., C. H. Zhang, T. A. Callcott, and D. L. Ederer, 1989, J. Appl. Phys. **66**, 3676.
Phillipp, H. R., and H. Ehrenreich, 1959, Phys. Rev. **115**, 786.
Platzman, P. M., and E. D. Isaacs, 1998, Phys. Rev. B **57**, 11 107.
Pompa, M., A. M. Flank, P. Lagarde, J. Rife, I. Stekhin, M. Nakazawa, H. Ogasawara, and A. Kotani, 1997, Phys. Rev. B **56**, 2267.
Redinger, J., J. Yu, A. J. Freeman, and P. Weinberger, 1987, Phys. Lett. A **124**, 463.
Rehr, John, and Robert Albers, 2000, Rev. Mod. Phys. **72**, 621.
Rubensson, J.-E., S. Eisebitt, M. Nicodemus, T. Böske, and W. Eberhardt, 1994a, Phys. Rev. B **49**, 1507.
Rubensson, J.-E., S. Eisebitt, M. Nicodemus, T. Böske, and W. Eberhardt, 1994b, Phys. Rev. B **50**, 9035.
Rubensson, J.-E., J. Lüning, S. Eisebitt, and W. Eberhardt, 1995, Phys. Rev. B **51**, 13 856.
Rubensson, J.-E., D. Mueller, R. Shuker, D. L. Ederer, C. H. Zhang, J. Jia, and T. A. Callcott, 1990, Phys. Rev. Lett. **64**, 1047.
Sakurai, J. J., 1967, *Advanced Quantum Mechanics* (Addison-Wesley, Reading, MA), Chap. 2.
Shin, S., A. Agui, M. Fujisawa, Y. Tezuka, T. Ishii, and N. Hirai, 1995, Rev. Sci. Instrum. **66**, 1584.

Shin, S., A. Agui, and Y. Harada, 1997, J. Synchrotron Radiat. **4**, 256.
Shin, S., A. Agui, M. Watanabe, M. Fujisawa, Y. Tezuka, and T. Ishii, 1996, Phys. Rev. B **53**, 15 660.
Shin, S., M. Fujisawa, H. Ishii, Y. Harada, M. Watanabe, M. M. Grush, T. A. Callcott, R. C. C. Perera, E. Z. Kurmaev, A. Moewes, R. Winarski, S. Stadler, D. L. Ederer, 1998, J. Electron Spectrosc. Relat. Phenom. **92**, 197.
Shirley, E. L., 1998, Phys. Rev. Lett. **80**, 794.
Skytt, P., P. Glans, D. C. Mancini, J.-H. Guo, N. Wassdahl, J. Nordgren, and Y. Ma, 1994, Phys. Rev. B **50**, 10457.
Sparks, C. J., Jr., 1974, Phys. Rev. Lett. **33**, 262.
Stagarescu, C. B., L.-C. Duda, K. E. Smith, J. H. Guo, J. Nordgren, R. Singh, and T. D. Moustakas, 1996, Phys. Rev. B **54**, R17 335.
Strange, P., P. J. Durham, and B. L. Gyorffy, 1991, Phys. Rev. Lett. **67**, 3590.
Strange, C. F. Hague, J.-M. Mariot, P. J. Durham, and B. L. Gyorffy, 1993, Jpn. J. Appl. Phys., Part 1 **32**, 302.
Susaki, T., A. Sekiyama, K. Kobayashi, T. Mizokawa, A. Fujimori, M. Tsunekawa, T. Muro, T. Matsushita, S. Suga, H. Ishii, T. Hanyu, A. Kimura, H. Namatame, M. Taniguchi, T. Miyahara, F. Iga, M. Kasaya, and H. Harima, 1996, Phys. Rev. Lett. **77**, 4269.
Taguchi, M., 1998, Ph.D. thesis (University of Tokyo).
Taguchi, M., J. C. Parlebas, T. Uozumi, A. Kotani, and C.-C. Kao, 2000, Phys. Rev. B **61**, 2553.
Taguchi, M., T. Uozumi, and A. Kotani, 1997, J. Phys. Soc. Jpn. **66**, 247.
Takagawara, T., E. Hanamura, and R. Kubo, 1977, J. Phys. Soc. Jpn. **43**, 802.
Tanaka, S., and A. Kotani, 1993, J. Phys. Soc. Jpn. **62**, 464.
Tanaka, S., Y. Kayanuma, and A. Kotani, 1988, J. Phys. (France) **49**, C8-735.
Tanaka, S., K. Okada, and A. Kotani, 1991, J. Phys. Soc. Jpn. **60**, 3893.
Tanaka, S., Y. Kayanuma, and A. Kotani, 1990, J. Appl. Phys. **59**, 1488.
Tanaka, S., K. Okada, and A. Kotani, 1989, J. Phys. Soc. Jpn. **58**, 813.
Tanaka, S., H. Ogasawara, Y. Kayanuma, and A. Kotani, 1989, J. Phys. Soc. Jpn. **58**, 1087.
Tanaka, S., and A. Kotani, 1992, J. Appl. Phys. **61**, 4212.
Tanaka, S., K. Okada, and A. Kotani, 1994, J. Phys. Soc. Jpn. **63**, 2780.
Tanaka, S., and Y. Kayanuma, 1996, Solid State Commun. **100**, 77.
Tezuka, Y., S. Shin, A. Agui, M. Fujisawa, and T. Ishii, 1996, J. Phys. Soc. Jpn. **65**, 312.
Thole, B. T., P. Carra, F. Sette, and G. van der Laan, 1992, Phys. Rev. Lett. **68**, 1943.
Tillborg, H., A. Nilsson, T. Wiell, N. Wassdahl, N. Mårtensson, and J. Nordgren, 1993, Phys. Rev. B **47**, 16 464.
Toyozawa, Y., 1976, J. Phys. Soc. Jpn. **41**, 400.
Toyozawa, Y., A. Kotani, and A. Sumi, 1977, J. Phys. Soc. Jpn. **42**, 1495.
Triguero, L., Y. Luo, L. G. M. Pettersson, H. Ågren, P. Väterlein, M. Weinelt, A. Fröhlish, J. Hasselström, O. Karis, and A. Nilsson, 1999, Phys. Rev. B **59**, 5189.
Tsang, K. L., C. H. Zhang, T. A. Callcott, E. T. Arakawa, and D. L. Ederer, 1987, Phys. Rev. B **35**, 8374.
Tsang, K.-L., C. H. Zhang, T. A. Callcott, L. R. Canfield, D. L. Ederer, J. E. Blendell, C. W. Clark, N. Wassdahl, J. E. Rubensson, G. Bray, N. Mortensson, J. Nordgren, R. Nyholm, and S. Cramm, 1988, Phys. Rev. B **37**, 2293.
Tsutsui, K., T. Tohyama, and S. Maekawa, 1999, Phys. Rev. Lett. **83**, 3705.
Tulkki, J., and T. Åberg, 1980, J. Phys. B **13**, 3341.
van der Laan, G., 1990, Phys. Rev. B **41**, 12 366.
van Veenendaal, M., and R. Benoist, 1998, Phys. Rev. B **58**, 3741.
van Veenendaal, M., and P. Carra, 1997, Phys. Rev. Lett. **78**, 2839.
van Veenendaal, M. A., H. Eskes, and G. A. Sawatzky, 1993, Phys. Rev. B **47**, 11 462.
van Veenendaal, M., J. B. Goedkoop, and B. T. Thole, 1996, Phys. Rev. Lett. **77**, 1508.
Wang, X., F. M. F. de Groot, and S. P. Cramer, 1997, Phys. Rev. B **56**, 4553.
Wang, X., C. Randall, G. Peng, and S. P. Cramer, 1995, Chem. Phys. Lett. **243**, 469.
Wassdahl, N., A. Nilsson, T. Wiell, H. Tillborg, L. C. Duda, J. H. Guo, N. Mårtensson, J. Nordgren, J. N. Andersen, and R. Nyholm, 1992, Phys. Rev. Lett. **69**, 812.
Watanabe, M., Y. Harada, Y. Komiyama, T. Kinugasa, R. Eguchi, H. Ishii, S. Shin, and A. Yagishita, 2000, unpublished.
Weinelt, M., A. Nilsson, O. Karis, M. Magnusson, T. Wiell, N. Wassdahl, N. Mårtensson, J. Stöhr, and M. Samant, 1996, in *Raman Emission by X-Ray Scattering*, edited by D. L. Ederer and J. H. McGuire (World Scientific, Singapore), p. 118.
Weinelt, M., A. Nilsson, M. Magnuson, T. Wiell, N. Wassdahl, O. Karis, A. Föhlisch, N. Mårtensson, J. Stöhr, and M. Samant, 1997, Phys. Rev. Lett. **78**, 967.
Weinelt, M., N. Wassdahl, T. Wiel, O. Karis, J. Hasselström, P. Bennich, A. Nilsson, J. Stöhr, and M. Samant, 1998, Phys. Rev. B **58**, 7351.
Wuilloud, E., B. Delley, W.-D. Schneider, and Y. Baer, 1984, Phys. Rev. Lett. **53**, 202.
Yokohama, H., M. Okamoto, T. Hamada, T. Imura, Y. Osaka, A. Chayahara, and M. Fujisawa, 1989, Jpn. J. Appl. Phys., Part 1 **28**, 555.
Zaanen, J., C. Westra, and G. A. Sawatzky, 1986, Phys. Rev. B **33**, 8060.
Zhang, C. H., T. A. Callcott, K.-L. Tsang, D. L. Ederer, J. E. Blendell, C. W. Clark, T. Scimeca, and Y.-W. Liu, 1989, Phys. Rev. B **39**, 4796.
Zhang, F. C., and T. M. Rice, 1988, Phys. Rev. B **37**, 3759.
Zhou, L., T. A. Callcott, J. J. Jia, D. L. Ederer, and R. Perera, 1997, Phys. Rev. B **55**, 5051.